THE UNIVERSITY OF QUEENSLAND
AUSTRALIA

Photonic Quantum Information and Quantum Walks

Matthew A. Broome
M.Phys. (Hons I) The University of Warwick
December 20, 2012

A thesis submitted for the degree of Doctor of Philosophy at
The University of Queensland in 2012
School of Mathematics and Physics

Abstract

Controlling quantum states of light is of central importance to many fields of modern physics. The technology to do so underpins the only feasible means for long-distance quantum communication using quantum-key-distribution, and plays a pivotal role in the application of quantum computing, quantum metrology and investigations of fundamental physics. Motivated by these applications, in this thesis we present a number of experimental results that demonstrate an enhanced level of control over photonic states. First, we tackle one of the most important technological issues currently facing the field, namely the creation of pure multi-photon Fock states from pulsed parametric downconversion. Our technique shows a marked improvement over previous photon sources when employed for quantum information tasks. At a more foundational level, we experimentally examine the properties of quantum correlations in the temporal domain, where our results highlight surprising differences between its spatial-domain counterpart of multipartite entanglement. Finally, we experimentally implement single- and multi-photon quantum walks in the discrete- and continuous-time regimes respectively. Quantum walks have received much attention in recent years due to their vast applicability in quantum information science, especially for quantum simulation and emulation. On this front we use the quantum walk formalism to perform a full experimental simulation of topological phases in a 1-dimensional configuration. Aside from being the first demonstration of topological phases in this regime, our system exhibits unprecedented control over the topological properties in a quantum system. As such we are able to observe the exotic behaviour of trapped bound states, and discover the new phenomenon of paired bound states—a feature unique to periodically driven systems.

Declaration by author

This thesis is composed of my original work, and contains no material previously published or written by another person except where due reference has been made in the text. I have clearly stated the contribution by others to jointly-authored works that I have included in my thesis.

I have clearly stated the contribution of others to my thesis as a whole, including statistical assistance, survey design, data analysis, significant technical procedures, professional editorial advice, and any other original research work used or reported in my thesis. The content of my thesis is the result of work I have carried out since the commencement of my research higher degree candidature and does not include a substantial part of work that has been submitted to qualify for the award of any other degree or diploma in any university or other tertiary institution. I have clearly stated which parts of my thesis, if any, have been submitted to qualify for another award.

I acknowledge that an electronic copy of my thesis must be lodged with the University Library and, subject to the General Award Rules of The University of Queensland, immediately made available for research and study in accordance with the Copyright Act 1968.

I acknowledge that copyright of all material contained in my thesis resides with the copyright holder(s) of that material. Where appropriate I have obtained copyright permission from the copyright holder to reproduce material in this thesis.

Publications during candidature

Peer-reviewed publications

1. *Discrete single-photon quantum walks with tunable decoherence,*
   Broome, M. A., Fedrizzi, A., Lanyon, B. P., Kassal, I., Aspuru-Guzik, A., White, A. G. *Physical Review Letters* **104**, 153602 (2010). (*arXiv:1002.4923v2*)

2. *Hardy's Paradox and violation of a state-independent Bell inequality in time*,
   Fedrizzi, A., Almeida, M. P., Broome, M. A., White, A. G., Barbieri, M.
   Physical Review Letters **106**, 200402 (2011). (*arXiv:1011.1304v2*)

3. *Two-photon quantum walks in an elliptical direct-write waveguide array*,
   Owens, J. O., Broome, M. A., Biggerstaff, D. N., Goggin, M. E., Fedrizzi, A., Linjordet, T., Ams, M., Marshall, G. D., Twamley, J., Withford, M. J., White, A. G.
   New Journal of Physics **13**, 075003 (2011). (*arXiv:1103.0604v2*)

4. *Reducing multi-photon rates in pulsed down-conversion by temporal multiplexing*,
   Broome, M. A., Almeida, M. P., Fedrizzi, A., White, A. G.
   Optics Express **19**, 22698-22708 (2011). (*arXiv:1110.4718v2*)

5. *Observation of topologically protected bound states in photonic quantum walks*,
   Kitagawa, T., Broome, M. A., Fedrizzi, A., Rudner M. S., Berg, E., Kassal, I., Aspuru-Guzik, A., Demler, E., White, A. G.
   Nature Communications **3**, 882 (2012). (*arXiv:1105.5334v1*)

6. *Efficient measurement of quantum dynamics via compressive sensing*,
   Shabani, A., Kosut, R. L., Mohseni, M., Rabitz, H.,
   Broome, M. A., Almeida, M. P., Fedrizzi, A., White, A. G.
   Physical Review Letters **106**, 100401 (2011). (*arXiv:0910.5498v2*)

7. *Multi-photon quantum interference in a multi-port integrated photonic device*,
   Metcalf, B. J., Thomas-Peter, N., Spring, J. B., Kundys, D., Broome, M. A., Humphreys, P., Jin, X. M., Barbieri, M., Kolthammer, W. S., Gates, J. C., Smith, B. J., Langford, N. K., Smith, P. G. R., Walmsley I. A.
   Accepted to *Nature Communications* (2012). (*arXiv:1208.4575v2*)

8. *Experimental* BOSONSAMPLING *in tunable tunable circuit*,
   Broome, M. A., Fedrizzi, A., Rahimi-Keshari, S., Dove, J., Scott, A., Ralph, T., White, A. G.
   Accepted to *Science* (2012). (*arXiv:1212.2234*)

Online e-print publications

9. *Direct characterisation of any linear photonic device*, e-print *arXiv:1210.6463v2*, (2012).
   Rahimi-Keshari, S., Broome, M. A., Fickler, R., Fedrizzi, A., Ralph, T., White, A. G.

Publications included in this thesis

Discrete single-photon quantum walks with tunable decoherence,

Broome, M. A., Fedrizzi, A., Lanyon, B. P., Kassal, I., Aspuru-Guzik, A., White, A. G.

Physical Review Letters **104**, 153602 (2010).

Incorporated as Chapter 6.

Contributor	Statement of contribution
Broome, M. A. (Candidate)	Initial development of concept (25%) Design and construction of experiment (80%) Preliminary and final data acquisition (75%) Data analysis and interpretation (75%) Theoretical model (25%) Complete first draft of manuscript (40%) Final draft of manuscript (20%) Referee replies and final manuscript revision (16%)
Fedrizzi, A.	Initial development of concept (25%) Design and construction of experiment (10%) Preliminary and final data acquisition (25%) Data analysis and interpretation (25%) Theoretical model (25%) Complete first draft of manuscript (30%) Final draft of manuscript (20%) Referee replies and final manuscript revision (16%)
Lanyon, B. P.	Initial development of concept (25%) Design and construction of experiment (10%) Theoretical model (25%) Complete first draft of manuscript (30%) Final draft of manuscript (20%) Referee replies and final manuscript revision (16%)
Kassal, I.	Theoretical model (25%) Complete first draft of manuscript (30%) Final draft of manuscript (20%) Referee replies and final manuscript revision (16%)
Aspuru-Guzik, A.	Referee replies and final manuscript revision (16%)
White, A. G.	Initial development of concept (25%) Final draft of manuscript (20%) Referee replies and final manuscript revision (16%)

Hardy's Paradox and violation of a state-independent Bell inequality in time, Fedrizzi, A., Almeida, M. P., Broome, M. A., White, A. G., Barbieri, M.
Physical Review Letters **106**, 200402 (2011).
Incorporated as Chapter 4.

Contributor	Statement of contribution
Broome, M. A. (Candidate)	Design and construction of experiment (50%) Preliminary and final data acquisition (33%) Data analysis and interpretation (33%) Complete first draft of manuscript (25%) Final draft of manuscript (20%) Referee replies and final manuscript revision (20%)
Fedrizzi, A.	Design and construction of experiment (25%) Preliminary and final data acquisition (33%) Data analysis and interpretation (33%) Complete first draft of manuscript (25%) Final draft of manuscript (20%) Referee replies and final manuscript revision (20%) Initial development of theory (50%)
Almeida, M. P.	Design and construction of experiment (25%) Preliminary and final data acquisition (33%) Data analysis and interpretation (33%) Complete first draft of manuscript (25%) Final draft of manuscript (20%) Referee replies and final manuscript revision (20%)
White, A. G.	Final draft of manuscript (20%) Referee replies and final manuscript revision (20%)
Barbieri, M.	Complete first draft of manuscript (25%) Final draft of manuscript (20%) Referee replies and final manuscript revision (20%)

Two-photon quantum walks in an elliptical direct-write waveguide array, Owens, J. O., Broome, M. A., Biggerstaff, D. N., Goggin, M. E., Fedrizzi, A., Linjordet, T., Ams, M., Marshall, G. D., Twamley, J., Withford, M. J., White, A. G.
New Journal of Physics **13**, 075003 (2011).
Incorporated as Chapter 8.

Contributor	Statement of contribution
Broome, M. A. (Candidate)	Design and construction of experiment (40%)
	Preliminary and final data acquisition (50%)
	Theoretical model of optical circuit (33%)
	Data analysis and interpretation (50%)
	Complete first draft of manuscript (30%)
	Final draft of manuscript (10%)
	Referee replies and final manuscript revision (100%)
Owens, J. O.	Design and construction of experiment (40%)
	Preliminary and final data acquisition (50%)
	Theoretical model of optical circuit (33%)
	Data analysis and interpretation (50%)
	Complete first draft of manuscript (30%)
	Final draft of manuscript (10%)
Biggerstaff, D. N.	Theoretical model of optical circuit (33%)
	Complete first draft of manuscript (10%)
	Final draft of manuscript (10%)
Goggin, M. E.	Design and construction of experiment (20%)
	Final draft of manuscript (10%)
Fedrizzi, A.	Complete first draft of manuscript (30%)
	Final draft of manuscript (10%)
Linjordet, T.	Design and fabrication of optical circuit (40%)
Ams, M.	Design and fabrication of optical circuit (15%)
Marshall, G. D.	Design and fabrication of optical circuit (15%)
Twamley, J.	Design and fabrication of optical circuit (15%)
Withford, M. J.	Design and fabrication of optical circuit (15%)
White, A. G.	Final draft of manuscript (10%)

Observation of topologically protected bound states in photonic quantum walks,
Kitagawa, T., Broome, M. A., Fedrizzi, A., Rudner M. S., Berg, E., Kassal, I., Aspuru-Guzik, A., Demler, E., White, A. G.
Nature Communications **3**, 882 (2012).
Incorporated as Chapter 7.

Contributor	Statement of contribution
Broome, M. A. (Candidate)	Design and construction of experiment (70%) Preliminary and final data acquisition (100%) Theoretical model (33%) Data analysis and interpretation (75%) Complete first draft of manuscript (25%) Final draft of manuscript (20%) Referee replies and final manuscript revision (35%)
Kitagawa, T.	Initial development of concept (70%) Theoretical model (33%) Complete first draft of manuscript (25%) Final draft of manuscript (20%) Referee replies and final manuscript revision (25%)
Fedrizzi, A.	Design and construction of experiment (30%) Theoretical model (33%) Data analysis and interpretation (25%) Complete first draft of manuscript (20%) Final draft of manuscript (10%) Referee replies and final manuscript revision (10%)
Rudner, M. S.	Initial development of concept (10%) Complete first draft of manuscript (10%) Final draft of manuscript (10%) Referee replies and final manuscript revision (10%)
Berg, E.	Initial development of concept (10%) Complete first draft of manuscript (10%) Final draft of manuscript (10%) Referee replies and final manuscript revision (10%)
Kassal, K.	Complete first draft of manuscript (10%) Final draft of manuscript (10%) Referee replies and final manuscript revision (10%)
Aspuru-Guzik, A.	Final draft of manuscript (5%)
Demler, E.	Initial development of concept (10%) Final draft of manuscript (5%)
White, A. G.	Final draft of manuscript (10%)

Reducing multi-photon rates in pulsed down-conversion by temporal multiplexing,
Broome, M. A., Almeida, M. P., Fedrizzi, A., White, A. G.
Optics Express **19**, 22698-22708 (2011).
Incorporated as Chapter 3.

Contributor	Statement of contribution
Broome, M. A. (Candidate)	Initial development of concept (33%) Design and construction of experiment (75%) Preliminary and final data acquisition (75%) Data analysis and interpretation (50%) Theoretical model of photon source and circuit (100%) Complete first draft of manuscript (80%) Final draft of manuscript (40%) Referee replies and final manuscript revision (100%)
Almeida, M. P.	Initial development of concept (33%) Design and construction of experiment (25%) Preliminary and final data acquisition (25%) Data analysis and interpretation (25%) Complete first draft of manuscript (10%) Final draft of manuscript (20%)
Fedrizzi, A.	Data analysis and interpretation (25%) Complete first draft of manuscript (10%) Final draft of manuscript (20%)
White, A. G.	Initial development of concept (33%) Final draft of manuscript (20%)

Contributions by others to the thesis

No contributions by others.

Statement of parts of the thesis submitted to qualify for the award of another degree

None.

Keywords

Keywords: photonics, quantum walks, quantum optics, single photons, downconversion, quantum information

Australian and New Zealand Standard Research Classifications (ANZSRC)

ANZSRC code: 020603 Quantum Information, Computation and Communication 50%
ANZSRC code: 020604 Quantum Optics, 30%
ANZSRC code: 020503 Nonlinear Optics and Spectroscopy, 20%

Fields of Research (FoR) Classification

FoR code: 0206 Quantum Physics, 80%
FoR code: 0205 Optical Physics, 20%

Acknowledgements

I sincerely hope that those who I have worked with during the course of my Ph.D. already realise how much they have aided my learning and development as a researcher. However, as it is traditional to do so, I will acknowledge them all here.

First and foremost I want to thank my advisory team. For his unprecedented enthusiasm about everything, especially our research, I want to thank Andrew White. Thank you for giving me independence to do what I wanted and guidance when I needed it. For teaching me everything I needed to know of experimental quantum optics I have Marcelo Almeida, Alessandro Fedrizzi and Till Weinhold to thank. All of you are my good friends now whether you like it or not.

I would also like to acknowledge the support from all my fellow Ph.D. students, especially Geoff Gillett for his LabVIEW brilliance and clear quantum insights; Devin Smith and Devon Biggerstaff for their help with experiments and theoretical concepts; Nathan Walk and Jacques Pienaar for stimulating break-time conversations; Glen Harris, Terry McRae and Jon Swaim for finding time to show me some other cool physics; Sven Ramelow: ‘if you can learn just one thing each day’, thanks for that; Yarema Reshitnyk for being a great office buddy; and James Owens for putting up with me during late nights in the lab. Finally I want to thank Ben Lanyon for his ideas that contribute to this work, his learned advice, and for getting me here in the first place!

I strongly believe in the importance of a work-life balance, and for helping me achieve that over the past few years, I thank Mike Garrett and Leif Humbert for waking me up for 6:00am surf sessions.

As is often the case with science, an outside perspective can go a long way. For keeping your doors open and finding the time to discuss physics I am grateful to Gerard Milburn, Tim Ralph, Ben Powell, Warwick Bowen and Tom Stace.

For the invaluable time I spent away from UQ learning new physics, I have my hosts and team of theorists to thank at Harvard University, Ivan Kassal, Alán-Aspuru Guzik, Takuya Kitawaga, Erez Berg, Mark Rudner and Eugene Demler; and all the ultrafasters at Oxford University, especially, Nathan Langford, Ian Walmsley, Nick Thomas-Peter, Benjamin Metcalf and Justin Spring (‘Stand by... I’m going in’).

Alongside my studies I have been fortunate enough to engage with many young potential scientists around Australia—an experience that has shaped my time in this country. For giving me the opportunity to ‘Outreach in the Outback’ I thank Sebastian Schnelle and Andrew Stephenson for their vision and dedication to science outreach; the OSA, ATSE and EQuS for financial support; and Halina Rubinsztein-Dunlop and Andrew White for *always* supporting our outreach endeavours.

This thesis represents a culmination of many years of learning physics on my behalf, but also many years of encouragement and support from others. For inspiring me to do all this, and for doing more than just your job, I thank Mr Davis, Dr Stokes, Mr Deal, Mr Ellis and Steve Dixon. I am also grateful to Peter Ogden, Tim Simmons, Anne Hoole and Jane Fidler of the Ogden Trust, for their unwavering support and dedication to excellence in physics education.

To all my friends in the Northern Hemisphere, especially James Bennett and Alex Wood, thanks for being reliable, and to all the friends I’ve made in Australia, you’ve made my time here.

A special thanks goes to Kimberley, for all her support throughout my studies. We’ve managed to have some great adventures over here haven’t we?

Finally, to my family, thanks for understanding the time I’ve spent away, and to my twin brother James: ‘I’ll be back soon. Over and out Roger Red...’

Contents

List of Figures

For my grandfathers.

Introduction

As humans we have always strived to understand the rules that govern the way things around us operate. These rules will often emerge as a consequence of studying the patterns of our world, from the way the sun rises each day to the predictability of the ocean tides. Both of these effects can in part be attributed to the Earth's rotation on its axis, although studying them is not enough to explain *why* the Earth rotates with the frequency it does, or even how the Earth came to be where it is in the first place. Answering these questions required a deeper study of our universe, in fact both mysteries can be solved by observing the formation of solar systems *outside* of our own [1].

In a similar way we have found ourselves looking deeper into the microscopic world to explain many macroscopic phenomena. One of the more famous examples is the explanation of the energy distribution from a black-body emitter, of which a correct description was first formulated in 1900 by Max Planck. His discovery, that one should consider the energy field emitted from a black-body as a collection of discrete packets of energy, or 'quanta', is heralded as the birth of *quantum* theory. More than a hundred years after this discovery we have transformed our view of the world. We now have a concrete picture of how the universe behaves at the atomic and subatomic scales and are able to observe things governed by the laws of quantum mechanics.

Quantum mechanics is undoubtedly the most successful theory in modern physics owing to its precise predictions of many experimentally observable phenomena. Consequently there is now a vast portfolio of experiments that demonstrate its success. Soon after the theory's inception, concepts such as quantisation were beautifully exemplified by the photo-electric effect [2] (quantisation of the electromagnetic field) and the Stern-Gerlach experiment [3] (quantisation of electron spin). Other more ambitious experiments, such as Bose-Einstein condensation [4, 5] which was not realised until over 70 years after its prediction [6, 7], demonstrated that quantum theory applied equally well to larger systems, not just to single particles.

Central to the above experiments is the discovery of *wave-particle* duality, the idea that sometimes particles act as waves and sometimes waves act as particles. It is this concept that underpins much of quantum theory's success in describing the naturally occurring phenomenon that, before it, had no physical explanation. The wave-like behaviour of electrons for example explains atomic orbitals and therefore the structure of elements in the periodic table and how they chemically bond [8]. The history of quantum physics is littered with many successes of this kind which, until recently, simply proved quantum mechanics as a tool for describing interesting physical behaviour.

This journey of exploring the quantum world inside the laboratory has left us with a plethora of experimental techniques to isolate, manipulate and probe quantum systems. As such we are now entering a new phase in the story of quantum physics in which quantum systems can be coherently engineered and used to our advantage for quantum communication, quantum computation and quantum simulation [8]. **This thesis is a contribution to this effort, focused specifically in the field of quantum optics**.

Overview of this thesis

This work is predominantly a thesis by publication. Chapters 3, 4, 6, 7 and 8 are all peer reviewed research papers, four of which I am either the lead or second author. Each paper is self contained, meaning that a reader with a strong background in quantum physics could follow the ideas and arguments throughout them. For this reason, those readers who are mainly interested in the experimental results of this work may wish to move directly to these chapters. However, for the purpose of completeness additional introductory Chapters 1, 2 and 5 serve to provide the less technically familiar reader with the necessary tools to understand the thesis as a whole.

Although the common theme running throughout this thesis is the use of single photon states for quantum information and quantum simulation, as an entirety, this is the only aspect that ties *all* of the projects together. Apart from Chapters 6 and 7, each research project does not necessarily follow as a result of any other project. However, as the title of this thesis suggests there are two main parts to this work: photonic quantum information processing and photonic quantum walks given in Parts I and II respectively. Their constituent chapters are set out as follows.

Part I: Photonic Quantum Information Processing

In Chapters 1 and 2 we lay down the key physical concepts and mathematical tools forming the groundwork of quantum information with photons. The first of these chapters focuses specifically on the framework of quantum information and quantum computation, but in an architecture independent way. That is, the concepts of storing, manipulating and measuring quantum information are dealt with on an abstract level rather than pertaining specifically to photonics. In Chapter 2 we introduce quantum information from a photonic perspective and discuss some of the finer details of experimental photonic quantum information processing.

The first new results of this work are given in Chapter 3 where we demonstrate a technique to reduce the level of noise from the most widely used source of single photon states: spontaneous parametric downconversion (SPDC). Since SPDC relies on spontaneous emission it is inherently non-deterministic and can produce more than one pair of photons simultaneously which introduces noise into the measurement statistics. With our technique we demonstrate a significant improvement in the visibility of two-photon interference as well as the fidelity of quantum computation protocols.

In Chapter 4 we investigate the properties of quantum correlations in time. Traditionally, quantum correlations refer to the joint properties of multiple quantum particles that are spatially separated. Here instead we look at how the measurements on a single particle at time t_1 are correlated with a non-destructive measurement performed on the same particle at time t_0, where $t_0 < t_1$. Additionally, in the same study, we present the temporal form of Hardy's paradox performed on the same particle, as opposed to the previously studied space-like separated measurements performed on two particles.

Part II: Photonic Quantum Walks

In the second part of this thesis we study single- and multi-photon quantum walks in one and two dimensions. As the experimental techniques, for example those of single photon generation from SPDC and non-classical interference, are identical to those discussed in Chapter 2 we omit them here. Instead we begin with Chapter 5 with a mathematical overview of the two types of walks studied in this thesis, the discrete- and continuous-time quantum walks.

In Chapter 6 we experimentally demonstrate a discrete-time single-photon quantum walk on a line in space. With the same experimental setup we investigate the effects of absorbing boundaries on the survival probability of the quantum walker, as well as the effect of controlled amounts of decoherence where we are able to observe the quantum-to-classical transition.

In Chapter 7 we use the same system as above to investigate the topological properties of photonic quantum walks. Taking the idea of a quantum simulator we encode specific quantum walk Hamiltonians at different points across the walk lattice. Importantly, by implementing topologically distinct Hamiltonians we are able to observe the exotic topological behaviour of bound states at the interface between topologically distinct regions.

Finally, in keeping with the theme of quantum walks, in Chapter 8 we demonstration a two-photon quantum walk in a three-dimensional waveguide structure. As well as highlighting the feasibility of these waveguide structures for emulation of coherent quantum phenomena, we identify some of their properties that are are still poorly understood, for example the polarisation dependent coupling between waveguides.

In the remaining pages we draw together the work in this thesis and make some concluding remarks on future research directions in these areas.

References

[1] Montmerle, T. *et al.* Solar system formation and early evolution: the first 100 million years. *Earth, Moon, and Planets* **98**, 39–95 (2006).

[2] Einstein, A. Concerning an heuristic point of view toward the emission and transformation of light. *Ann. Phys (Translated into English by American Journal of Physics, 33, 1965)* **17**, 132 (1905).

[3] Gerlach, W. & Stern, O. Das magnetische Moment des Silberatoms. *Zeitschrift für Physik* **9**, 353–355 (1922).

[4] Anderson, M. H., Ensher, J. R., Matthews, M. R., Wieman, C. E. & Cornell, E. A. Observation of Bose-Einstein condensation in a dilute atomic vapor. *Science* **269**, 198–201 (1995).

[5] Davis, K. B. *et al.* Bose-Einstein condensation in a gas of sodium atoms. *Phys. Rev. Lett.* **75**, 3969–3973 (1995).

[6] Bose, S. N. Plancks Gesetz und Lichtquantenhypothese. *Zeitschrift fuer Physik A Hadrons and Nuclei* **26**, 178–181 (1924).

[7] Einstein, A. Zur Quantentheorie des idealen Gases. *Sitzungsber. Preuss. Akad. Wiss.* **3**, 18–25 (1925).

[8] Dowling, J. P. & Milburn, G. J. Quantum technology: the second quantum revolution. *Phil. Trans. R. Soc. Lond. A* **361** (2003).

Part I

Photonic Quantum Information Processing

CHAPTER 1

Introduction to quantum computation

Computation refers to the act of calculation or information processing on a computing machine. The idea is to use a computer to run an algorithm—a well defined set of rules—to calculate a function's outcome or process information. With this method we can use computers to solve a variety of different problems in physics. In classical physics for example, the rules that govern the motion of classical particles in a potential are those of Newtonian mechanics. For quantum particles we use quantum mechanics to define the equations of motion. From a computational perspective, the key difference between classical and quantum systems is that the computational resources needed to compute the outcome of classical and quantum systems scale differently with the size of the problem.

Take for example a system of N classical coins each of which are equally likely to have the outcome values $c = \{0, 1\}$. We toss all the coins and upon them landing record their values. Although there is a total of 2^N possible outcomes, we only require N bits of information to record the state of the system. In the quantum case each coin can be in a superposition of both coin values $q = \{0, 1\}$, meaning for N quantum coins we require 2^N bits of information to fully describe the system. It is this exponential increase in parameter space that ultimately renders classical computers inefficient for solving problems in the quantum regime. An algorithm's efficiency is related to how the number of individual steps, or computer operations, required to run the algorithm scales as the problem size increases. Inefficient algorithms are those where the size of computer needed to run the algorithm scales exponentially with the problem size, conversely, efficient algorithms are those where the computer size scales at most polynomially with the problem size.

As an alternative to using classical computers for solving the dynamics of quantum systems, why not use a quantum system itself? The concept of a quantum computer was first proposed by Feynman in *"Simulating Physics with Computers"* [1] and takes advantage of the inherent quantum nature of such a device. In essence a quantum computer would work in the following way. We encode an initial state into the state of a quantum system and evolve it under some interactions that also obey the laws of quantum mechanics. In some cases both the initial state and the interactions could form the algorithm of the quantum computer. Importantly, as the quantum system naturally keeps track of the entire state of the system, simply measuring its state when the algorithm is complete is enough to determine the answer.

Both classical and quantum computers are restricted in the type of functions they can evaluate—namely computable functions—but in some cases, a quantum computer is more efficient at solving problems than a classical one. For example, the factoring of large integers into prime numbers, for which there is no known efficient classical algorithm, was shown to be efficiently computable on a quantum computer by Shor [2]. The prospect of such computational speed-ups over classical algorithms is one reason behind the excitement for quantum computing, though quantum computers also have the potential to make *quantum* systems easier to simulate. This idea takes advantage of the fact that some physical quantum systems can be made to 'look' like other quantum systems. That is, the equations that describe the physics of a quantum system—given by the system's Hamiltonian—is simply a mathematical object and therefore in principle could be encoded using many different physical systems. The task then is to find an easily controllable quantum system whose interactions can be tailored such that it simulates a Hamiltonian of interest: this would be a quantum simulator.

With the prospect of outperforming classical computers and simulating new physics, realising a scalable quantum computer or simulator has become the goal of many experimental groups around the world. The crux of this task is the development of a highly controllable quantum system that can be prepared in a known state, measured with great certainty and sufficiently isolated from its environment such that it is not disturbed by it. In addition there must be a set of quantum interactions that the experimenter can perform which is capable of performing *any* quantum computation, in the circuit model of quantum computation this set of interactions is called a *universal set.* These criteria are the essence of the DiVincenzo criteria for a scalable quantum computer [3].

1.1 Basic quantum information

Quantum computation is a sub-field of the more broader field of quantum information—the study of how information can be stored, manipulated and computed in the quantum world. As such I will continue this discussion with an overview of basic quantum information theory. In particular I will focus on the mathematical framework that is important to understand this thesis.

1.1.1 Qubits

What makes quantum information totally different from its more familiar counterpart, classical information, is quantum *superposition.* Quantum superposition is the notion that a system's property can assume two distinct values at the same time, a concept that is perfectly acceptable in the quantum world but utterly absurd in a classical one. As an example consider the most fundamental unit of classical information a binary digit or bit for short. On classical computing machines that operate via electrical signals[1] a bit of information can be represented as a voltage. For example in transistor-transistor logic (TTL) circuits if a signal $S < V_0$ the bit is assigned

---

[1] One of the first computers, designed by Charles Babbage, was capable of simple arithmetic and was proposed to be entirely mechanical.

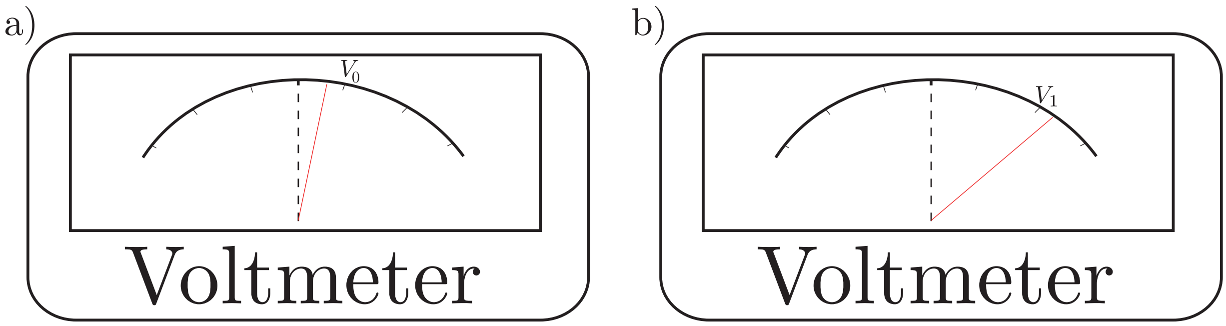

Figure 1.1: Measuring a classical voltage signal. a) A voltage representing the classical bit value ‘0’ and b) a voltage representing a bit value of ‘1’. The classical world does not allow a system to be in the state ‘0’ and ‘1’ simultaneously.

the value ‘0’ and if $S > V_1$ the bit is assigned the value ‘1’, see Fig. 1.1. Clearly in this classical scenario the signal cannot be both ‘0’ and ‘1’ simultaneously.

In the quantum case the most basic unit of information is the quantum bit or *qubit*. Qubits, like classical bits, are two level systems with the distinct states zero and one, denoted in the Dirac notation as $|\mathbf{0}\rangle$ and $|\mathbf{1}\rangle$ respectively [4] . However, unlike bits they can exist in any superposition of these states and the general form of a qubit $|\psi\rangle$, is given by

$$|\psi\rangle = e^{i\gamma}(\cos(\theta/2)\,|\mathbf{0}\rangle + e^{i\phi}\sin(\theta/2)\,|\mathbf{1}\rangle), \tag{1.1}$$

where γ, θ and ϕ are real numbers. The factor $e^{i\gamma}$ is called the *global* phase and has no measurable effects, it can therefore be ignored, meaning that the state of a qubit is reduced to

$$|\psi\rangle = \cos(\theta/2)\,|\mathbf{0}\rangle + e^{i\phi}\sin(\theta/2)\,|\mathbf{1}\rangle\,. \tag{1.2}$$

The qubit state can be visualised using the two dimensional surface of a sphere which we will call the qubit sphere[2], where θ and ϕ are polar coordinates for a position on the surface, see Fig. 1.2.

Importantly, the states $|\mathbf{0}\rangle$ and $|\mathbf{1}\rangle$ are vectors which form a complete basis set, or spanning set, in a two-dimensional inner product space $\mathcal{H}_2$, this particular set is called the *computational* basis. That is, $|\mathbf{0}\rangle$ and $|\mathbf{1}\rangle$ span a vector space V, where the inner product maps $V \times V$ to the complex number space $\mathbf{C}$. The inner product, or dot product as it is sometimes called, is a means of determining the orthogonality of two vectors in V. For two vectors of equal length

---

[2] Historically this was called the Poincaré sphere which was originally used to describe the polarisation states of light. More recently a rotated version of the Poincaré sphere, called the Bloch sphere, has become the common way to describe a two-level quantum system. These two pictures are equivalent up to a $\pi/2$ rotation.

Symbol	State
$\lvert + \rangle$	$\frac{1}{\sqrt{2}}(\lvert 0\rangle + \lvert 1\rangle)$
$\lvert - \rangle$	$\frac{1}{\sqrt{2}}(\lvert 0\rangle - \lvert 1\rangle)$
$\lvert +i \rangle$	$\frac{1}{\sqrt{2}}(\lvert 0\rangle + i\lvert 1\rangle)$
$\lvert -i \rangle$	$\frac{1}{\sqrt{2}}(\lvert 0\rangle - i\lvert 1\rangle)$

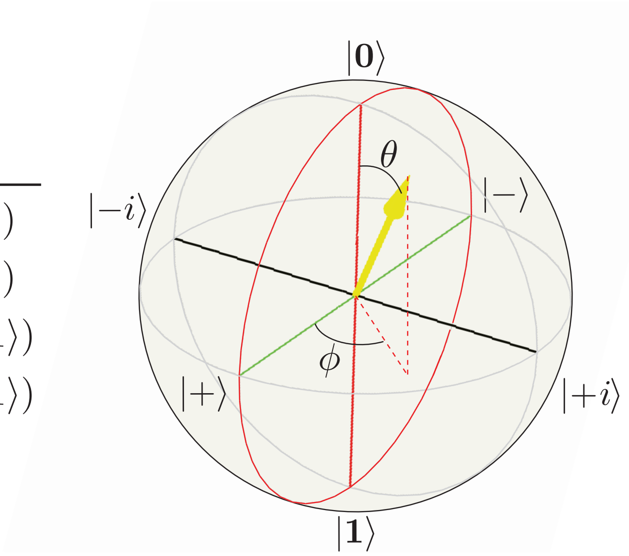

Figure 1.2: Qubit states represented by points on a sphere. All pure states live on the surface of the qubit sphere and are coherent superpositions of the computational basis states $\lvert \mathbf{0} \rangle$ and $\lvert \mathbf{1} \rangle$. θ and ϕ are the polar coordinates of the pure states. The red circle depicts the real plane, that is, all the pure states $\alpha \lvert \mathbf{0} \rangle + \beta \lvert \mathbf{1} \rangle$, where α and β real numbers. The green (connected by $\lvert + \rangle$ and $\lvert - \rangle$), black (connected by $\lvert +i \rangle$ and $\lvert -i \rangle$) and red (connected by $\lvert \mathbf{0} \rangle$ and $\lvert \mathbf{1} \rangle$) lines are the x, y and z axes respectively.

$\lvert x \rangle$ and $\lvert y \rangle$ the inner product is given by

$$\langle x \,|y \rangle \equiv \begin{bmatrix} x_1^* \dots x_i^* \dots x_n^* \end{bmatrix} \begin{bmatrix} y_1 \\ \vdots \\ y_i \\ \vdots \\ y_n \end{bmatrix} = \sum_i x_i^* y_i, \tag{1.3}$$

where * denotes the complex conjugate [5]. Any qubit state can be expressed in terms of the states $\lvert \mathbf{0} \rangle$ and $\lvert \mathbf{1} \rangle$ which are orthogonal, therefore satisfying the following inner products, $\langle \mathbf{0} \,| \mathbf{1} \rangle = \langle \mathbf{1} \,| \mathbf{0} \rangle = 0$ as well as $\langle \mathbf{0} \,| \mathbf{0} \rangle = \langle \mathbf{1} \,| \mathbf{1} \rangle = 1$. For finite dimensional spaces, such as that for qubits, the inner product space $\mathcal{H}_2$ is called a *Hilbert* space.

Finally, it is oftentimes useful to express the state of a qubit explicitly as a vector, so that it looks like

$$\lvert \psi \rangle = \alpha \begin{bmatrix} 1 \\ 0 \end{bmatrix} + \beta \begin{bmatrix} 0 \\ 1 \end{bmatrix} = \alpha \lvert \mathbf{0} \rangle + \beta \lvert \mathbf{1} \rangle, \tag{1.4}$$

where α and β are complex numbers that satisfy the relation $|\alpha|^2 + |\beta|^2 = 1$.

1.1.2 The density operator

Equations 1.1-1.4 can only describe *pure* states, that is, an entirely coherent superposition of the basis states. However, given an ensemble of qubits one might find that in addition to pure states the ensemble also encompasses a statistical *mixture* of $|\mathbf{0}\rangle$ and $|\mathbf{1}\rangle$. These states require a more complete description known as the *density operator* or *density matrix* formalism,

$$\rho = \sum_i p_i \, |\psi_i\rangle\langle\psi_i| \, , \tag{1.5}$$

where p_i is the probability of being in the state $|\psi_i\rangle$. In reality one will always encounter mixedness since no quantum system is able to maintain perfect coherence. The density operator is therefore a more useful tool for real world quantum physics than the pure state formalism. As a measure of this coherence the *purity* of ρ is given by $\mathrm{Tr}(\rho^2)$ which is < 1 for mixed states and unity for pure states. More generally, the lower bound for purity is $\mathrm{Tr}(\rho^2)=1/d$ for a d-dimensional system.

1.1.3 Mixed states and decoherence

Like many aspects of quantum mechanics the exact meaning of a mixed state is open to interpretation. A mixed state can be thought of as a statistical mixture of many particles each in a pure state where performing a measurement reveals a particle's state (Copenhagen interpretation), or that each particle is in *reality* a mixed state containing less than unity information (many-worlds interpretation) [6]. Despite these differences we do have a good understanding of how mixture occurs in practice.

Mixture results from the interaction of a quantum state with an (internal or external) environment [6]. The environment in this context can be pictured either as another quantum system or in some cases a large thermal bath, where the interaction between it and the quantum system lead to quantum correlations between them. Such interactions can either be intentional, in the case of interacting two qubits for example, or an unwanted coupling of a quantum system to the experimental apparatus. More formally, as a result of the quantum system's interaction with another environment it is said to become 'entangled' with it (see Section 1.1.5). Recovering and accounting for these correlations would require knowing the corresponding effects that occurred to the environment as a result of *its* interaction with the quantum system. In cases where the environment is an unwanted coupling with the surrounding experimental apparatus, recovering these correlations is an impossible task, hence such information is lost, leading to mixture in the quantum state—this process is called decoherence. Throughout this thesis I will detail the mechanisms that lead to mixture in each experiment and in some cases suggest remedies to reduce their effects.

1.1.4 Multiple qubits

The usefulness of any computing device comes from the ability to manipulate many pieces of information. Thankfully in quantum information keeping track of multiple qubits is a simple extension of the single qubit case with the addition of the tensor product. The tensor product is a mathematical tool used to combine multiple vector spaces into one [5]. A single pure qubit lives in a vector space (see eq. 1.1), or Hilbert space, with dimension 2, since we require exactly 2 numbers to completely describe it. To describe a pure two-qubit system with individual states $|\psi_A\rangle$ and $|\psi_B\rangle$, we take the tensor product of their individual state vectors in the following way

$$|\Psi\rangle = |\psi_A\rangle \otimes |\psi_B\rangle = \begin{bmatrix} \alpha_A \\ \beta_A \end{bmatrix} \otimes \begin{bmatrix} \alpha_B \\ \beta_B \end{bmatrix} = \begin{bmatrix} \alpha_A\alpha_B \\ \alpha_A\beta_B \\ \alpha_B\alpha_B \\ \alpha_B\beta_B \end{bmatrix}. \tag{1.6}$$

The result is a state vector which lives in a Hilbert space of dimension 4. In general the dimension of the Hilbert space increases exponentially as 2^N, where N is the number of qubits. It is this exponential increase in the Hilbert space—and therefore the number of parameters needed to describe the quantum system—which renders classical computers inefficient for simulating quantum systems. Mixed states are dealt with in the same way by replacing the state vectors in Eq. 1.6 with the corresponding density operators.

The state $|\Psi\rangle$ in Eq. 1.6 is called a *product* or *separable* state because it can be described either as a state in the combined Hilbert space $\mathcal{H_{AB}}=\mathcal{H_A}\otimes\mathcal{H_B}$, or two separate states $|\psi_A\rangle$ and $|\psi_B\rangle$ in $\mathcal{H_A}$ and $\mathcal{H_B}$, respectively. However, this is not the case for all multiple qubit states, as some qubits share correlations, meaning that a description of the entire state cannot be given as a product of two separate states in their respective individual Hilbert spaces. In some cases these states share a type of correlation known as entanglement, which we will discuss now.

1.1.5 Two-qubit entanglement

The ability to entangle multiple qubits is believed to be a crucial element in quantum computation [7]. When multiple particles are entangled a full description of the system can only be given by their joint properties. Individual measurements on the particles reveal that they have no full identity of their own—they are in mixed states. An important class of entangled states are the two-qubit Bell states,

$$\begin{aligned} \left|\Phi^{\pm}\right\rangle &= \frac{1}{\sqrt{2}}(|\mathbf{0}\rangle_A \otimes |\mathbf{0}\rangle_B \pm |\mathbf{1}\rangle_A \otimes |\mathbf{1}\rangle_B) \\ \left|\Psi^{\pm}\right\rangle &= \frac{1}{\sqrt{2}}(|\mathbf{0}\rangle_A \otimes |\mathbf{1}\rangle_B \pm |\mathbf{1}\rangle_A \otimes |\mathbf{0}\rangle_B), \end{aligned} \tag{1.7}$$

where 'A' and 'B' denote the two parties who have access to the qubits: Alice and Bob respectively. We can prove that individually each qubit on its own is mixed by inspecting the state of one qubit regardless of the other. Mathematically this is equivalent to performing a *partial trace* on the system. If we have a joint system given by the density operator ρ_{AB} then we can 'trace out' Bob's half of the system to reveal only Alice's half by performing the partial trace given by,

$$\rho_A = \mathrm{Tr}_B(\rho_{AB}). \tag{1.8}$$

The notation Tr_B is referred to as 'tracing out' the system B so that we are only left with ρ_A. For any two state vectors in A $|a_1\rangle$ and $|a_2\rangle$, and likewise for B $|b_1\rangle$ and $|b_2\rangle$, the partial trace is defined as,

$$\mathrm{Tr}_B(|a_1\rangle\langle a_2| \otimes |b_1\rangle\langle b_2|) \equiv |a_1\rangle\langle a_2| \,\mathrm{Tr}(|b_1\rangle\langle b_2|), \tag{1.9}$$

noting that $\mathrm{Tr}(|b_1\rangle\langle b_2|)= \langle b_1 |b_2 \rangle$. Finally, combining Eqs. 1.8 and 1.9 we have,

$$\begin{aligned} \rho_A &= \mathrm{Tr}_B(\rho_{AB}) \\ &= \mathrm{Tr}_B\left(\sum_{i,j} p_{i,j}\, |a_i\rangle\langle a_j| \otimes |b_i\rangle\langle b_j|\right) \\ &= \sum_{i,j} p_{i,j}\, |a_i\rangle\langle a_j| \,\mathrm{Tr}(|b_i\rangle\langle b_j|). \end{aligned} \tag{1.10}$$

As an interesting example of the partial trace, let us we choose $|\Psi^+\rangle$ from Eq. 1.7 and trace out Bob's qubit so that the state of Alice's qubit is given by,

$$\begin{aligned} \rho_A &= \mathrm{Tr}_B\left(|\Psi^+\rangle\langle\Psi^+|\right) \\ &= \frac{|\mathbf{0}\rangle\langle\mathbf{0}|\,\langle \mathbf{1}\,|\mathbf{1}\rangle + |\mathbf{0}\rangle\langle\mathbf{1}|\,\langle \mathbf{1}\,|\mathbf{0}\rangle + |\mathbf{1}\rangle\langle\mathbf{0}|\,\langle \mathbf{0}\,|\mathbf{1}\rangle + |\mathbf{1}\rangle\langle\mathbf{1}|\,\langle \mathbf{0}\,|\mathbf{0}\rangle}{2} \\ &= \frac{|\mathbf{0}\rangle\langle\mathbf{0}| + |\mathbf{1}\rangle\langle\mathbf{1}|}{2} \\ &= \frac{I}{2}, \end{aligned} \tag{1.11}$$

which is a completely mixed state since the purity, $\mathrm{Tr}(\rho_A^2)$=1/2.

1.1.6 Unitary evolution and quantum gates

In an idealised theoretical framework the evolution of a quantum state $|\psi\rangle$, can be described by the operator U, such that the adjoint of this operator, $U^\dagger$ (the reverse of U), returns the initial state,

$$UU^\dagger |\psi\rangle = U^\dagger |\psi'\rangle = I |\psi\rangle, \tag{1.12}$$

where I is the identity operator, which is the same dimension as U with matrix elements given by I_{ij}=δ_{ij}, where δ_{ij} is the Kronecker delta function. This, property of an operator known as *unitarity*, is just as attainable in reality as pure states are (see above), i.e., not at all. It describes the evolution of a quantum system which is completely isolated from the environment and therefore entirely free from decoherence. This issue aside, it is a useful starting point in describing quantum state evolution.

We visualise quantum state evolution using the circuit model of quantum computation, shown in Fig. 1.3. A line depicts a quantum state and operators on that line either manipulate the quantum state or measure it. Double lines represent a classical information channel and the flow of information runs from left to right [5].

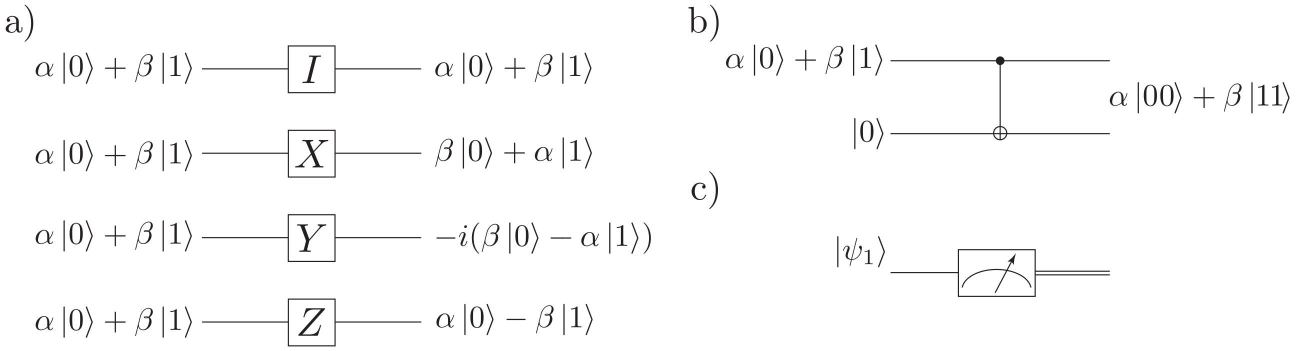

Figure 1.3: a) Single qubit Pauli operators depicted in the circuit model of quantum computation. b) Multiple qubit gates span multiple quantum states, and in some special cases are simply depicted as lines connecting two states as for the controlled-NOT gate, shown here. c) Measurement is depicted by this meter symbol with a classical information channel shown as two parallel lines.

Single qubit gates

Figure 1.3a shows the quantum circuit model depicting a class of single qubit unitaries called the Pauli operators. Of all the single qubit unitaries the Pauli operators are the most important since they form a complete set that span the 2×2 vector space of Hermitian unitaries, i.e. $U_m^{\dagger}{=}U_m$ and $U_m^2{=}U_m$. Consequently a combination of the Pauli operators can be used to perform arbitrary single qubit gates. The Pauli operators X, Y, Z and I are given by

$$\begin{aligned}\sigma_1 \equiv X \equiv \begin{bmatrix} 0 & 1 \\ 1 & 0 \end{bmatrix} \qquad \sigma_2 \equiv Y \equiv \begin{bmatrix} 0 & -i \\ i & 0 \end{bmatrix} \\ \sigma_3 \equiv Z \equiv \begin{bmatrix} 1 & 0 \\ 0 & -1 \end{bmatrix} \qquad \sigma_0 \equiv I \equiv \begin{bmatrix} 1 & 0 \\ 0 & 1 \end{bmatrix}.\end{aligned} \tag{1.13}$$

Single qubit quantum gates are also commonly called rotations as they can be depicted as rotations about axes on the qubit sphere. The rotation of a state by an angle θ about the axes $\vec{n} = (n_x, n_y, n_z)$ on the qubit sphere is given by

$$R_{\vec{n}}(\theta) \equiv e^{-i\theta\vec{n}\cdot\vec{\sigma}/2} = \cos\left(\frac{\theta}{2}\right) I - i\sin\left(\frac{\theta}{2}\right)(n_x X + n_y Y + n_z Z). \tag{1.14}$$

And an arbitrary single qubit unitary is given by

$$U = e^{(i\delta)} R_{\vec{n}}(\theta), \tag{1.15}$$

where $e^{(i\delta)}$ is a physically insignificant global phase shift. Figure 1.4 shows the the action of one of the most widely used single qubit rotations, the Hadamard.

The Hadamard's most important property in relation to this thesis is that it can be used to

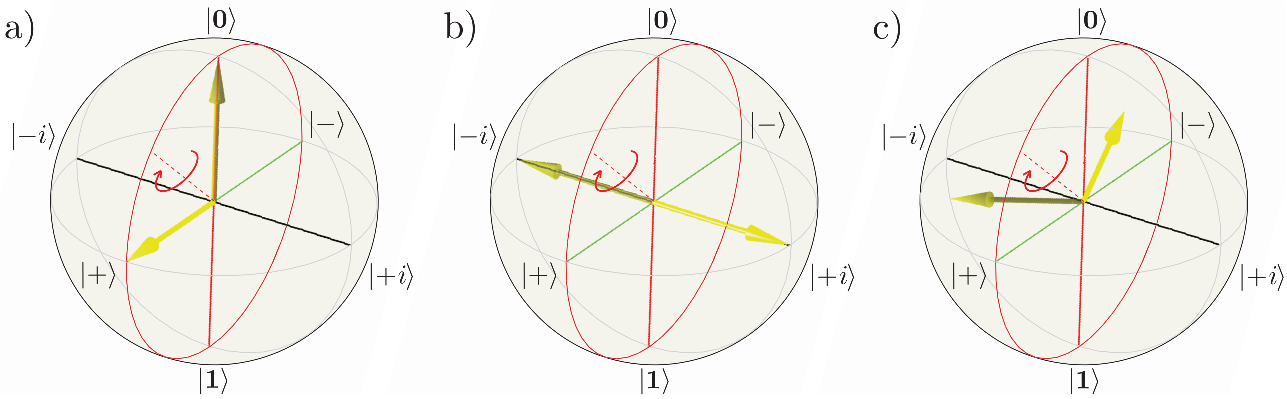

Figure 1.4: The action of the Hadamard operator on single qubit states. The Hadamard does a $\theta{=}\pi$ rotation about the axis $\vec{n}{=}(1/\sqrt{2},0,1/\sqrt{2})$, shown by the dashed red line. The qubit states are shown by the yellow arrows. a) $|\mathbf{0}\rangle \rightarrow (|\mathbf{0}\rangle + |\mathbf{1}\rangle)/\sqrt{2}$, b) $(|\mathbf{0}\rangle - i\,|\mathbf{1}\rangle)/\sqrt{2} \rightarrow (|\mathbf{0}\rangle + i\,|\mathbf{1}\rangle)/\sqrt{2}$ and c) $\alpha\,|\mathbf{0}\rangle + \beta\,|\mathbf{1}\rangle \rightarrow (\alpha+\beta)\,|\mathbf{0}\rangle + (\alpha-\beta)\,|\mathbf{1}\rangle$.

create a balanced state in the computational basis. That is, it performs the following unitary,

$$H\begin{bmatrix}\alpha\\ \beta\end{bmatrix} = \frac{1}{\sqrt{2}}\begin{bmatrix}1 & 1\\ 1 & -1\end{bmatrix}\begin{bmatrix}\alpha\\ \beta\end{bmatrix} = \frac{1}{\sqrt{2}}\begin{bmatrix}\alpha+\beta\\ \alpha-\beta\end{bmatrix}. \tag{1.16}$$

This operator becomes important in Part II on quantum walks. Here, the direction a quantum particle moves on a one-dimensional lattice is governed by its qubit state (often called the *coin* state in this context) and in the quantum case this can be both left and right!

Multiple qubit gates

Multi-qubit gates lie at the heart of any quantum computation protocol. In particular, they allow the state of one or some of the qubits entering the gate to have a significant effect on the state of another. An important class of multi-qubit gates are those that perform *control* operations. One of the major breakthroughs in quantum computing theory was the realisation that any n-qubit transformation can be achieved using many instances of the two-qubit controlled-NOT (CNOT) gate and single-qubit gates [8, 9, 10]; such a set of gates is known as a *universal* set. Since then, much attention has been paid to both the efficient use of CNOT gates for quantum computing as well as its physical realisation inside the laboratory. During the early stages of experimental quantum computation, realising a CNOT gate was a highly coveted goal due not only to its universality proof but also for its ability to produce maximally *entangled* states, see Section 1.1.5. Although, it has also been shown that any two-qubit gate which generates even a small amount of entanglement, is universal for quantum computation [11].

The CNOT circuit shown in Fig. 1.3b performs the Pauli-X operation on a *target* qubit $|y\rangle_t$ (bottom qubit in the picture), conditioned on the state of the *control* qubit $|x\rangle_c$ (top qubit in the picture) and in the computational basis performs the following unitary

$$U_{CNOT}\,|x\rangle_c\,|y\rangle_t = |x\rangle_c\,|y\oplus x\rangle_t \tag{1.17}$$

where $\oplus$ is addition modulo two [5]. To generate a maximally entangled state using a CNOT operation consider preparing the control qubit in the state $|+\rangle = (|\mathbf{0}\rangle + |\mathbf{1}\rangle)/\sqrt{2}$ and interacting it with a target qubit prepared in $|\mathbf{0}\rangle$ such that we get

$$U_{CNOT}\,|+\rangle_c\,|\mathbf{0}\rangle_t = \frac{|\mathbf{0}\rangle_c\,|\mathbf{0}\rangle_t + |\mathbf{1}\rangle_c\,|\mathbf{1}\rangle_t}{\sqrt{2}}. \tag{1.18}$$

This is the $|\Phi^+\rangle$ state given in Section 1.1.5.

An important gate for this thesis is the controlled-SIGN gate or CZ gate which performs a controlled Pauli-Z operation on the target qubit. It is equivalent to the CNOT with the addition of the single qubit Hadamard gate on either side of the target qubit.

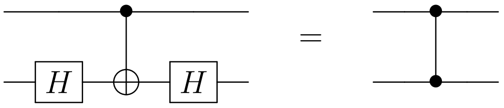

The CZ gate is therefore equally powerful with regard to universal quantum computing and the generation of maximally entangled states. In Chapter 2 we describe this gate in greater detail, and cover the real world implementation of it in Chapters 3 and 4.

1.1.7 Quantum measurement theory

After the initial preparation of the qubit states, and evolution under quantum logic gates, measurement is the final step of a quantum information task. Broadly speaking the experimenter is interested in the following question: given the state $|\psi\rangle$ and a set of measurement operators $\{M_m\}$ which act on the state space of $|\psi\rangle$ and whose measurement outcomes are m, what is the probability that m will occur? This probability is given by

$$p(m) = \langle\psi|\, M_m^\dagger M_m\, |\psi\rangle\,. \tag{1.19}$$

Since the probability of obtaining all measurement outcomes must sum to unity,

$$1 = \sum_m p(m) = \sum_m \langle\psi|\, M_m^\dagger M_m\, |\psi\rangle\,, \tag{1.20}$$

it follows that $\sum_m M_m^\dagger M_m = I$, this is called the *completeness* equation [5]. As a result of implementing the measurement operator, the state of the system immediately after the measurement is changed to

$$|\psi'\rangle = \frac{M_m\,|\psi\rangle}{\sqrt{\langle\psi|\, M_m^\dagger M_m\, |\psi\rangle}} = \frac{M_m\,|\psi\rangle}{\sqrt{p(m)}}. \tag{1.21}$$

Projective measurements

The most important type of measurement needed to understand this thesis is the *projective* measurement. The projector of rank-n,

$$\mathbf{P}_W = \sum_{m \in W^n} P_m = \sum_{m \in W^n} |\gamma_m\rangle\langle\gamma_m| , \tag{1.22}$$

acting on the state $|\psi\rangle$ gives the components of this state parallel to $|\gamma_m\rangle \in W^n$, where W^n is a subspace of the total Hilbert space of $|\psi\rangle$, $\mathcal{H}_d$. Projectors by definition are orthogonal, i.e. $\mathbf{P}_{W'}\mathbf{P}_W = \delta_{W',W}\mathbf{P}_W$, meaning that in the space $\mathcal{H}_d$ there can be at most d projectors each of rank-one. When $\mathbf{P}_W$ in Eq. 1.22 is the sum of this set of rank-one projectors, $\{P_m\}$, the measurement is said to be 'made in the $|\gamma_m\rangle$ basis'. In the simplest case of a pure qubit which has a total Hilbert space of size 2, there are at most 2 projectors, for example measuring in the $|\pm i\rangle = (|\mathbf{0}\rangle \pm i\,|\mathbf{0}\rangle)/\sqrt{2}$ basis requires the projection operators $P_{|+i\rangle} = |+i\rangle\langle+i|$ and $P_{|-i\rangle} = |-i\rangle\langle-i|$. These projection operators are also the eigenvectors of the Pauli-Y operator, so this measurement will often be referred to as a measurement of the spin[3] along the y-axis.

Importantly, projectors are Hermitian with the consequence that the eigenvalues or measurement outcomes of a projection are always real and therefore correspond to physical attributes of the measurement device. With this we can define the measurement *observable* O, given by its spectral decomposition

$$O = \sum_m \lambda_m P_m, \tag{1.23}$$

where λ_m are the corresponding eigenvalues of the projectors P_m. The average value of the observable $\langle O\rangle$, or *expectation* value, on the state $|\psi\rangle$, is given by

$$\begin{aligned} \langle O\rangle &= \sum_m \lambda_m p(m) \\ &= \langle\psi|\, O\, |\psi\rangle . \end{aligned} \tag{1.24}$$

This is the value of the observable after performing many instances of the same measurement operator O, on a large ensemble of identically prepared quantum states $|\psi\rangle$.

Nondestructive measurements

As well as performing two-qubit operations for computation and producing entanglement, the control gates discussed in Section 1.1.6 can also be utilised to make non-destructive measurements (also called nondemolition measurements) on a single qubit [12]. To perform a nondestructive measurement on the signal qubit $|\psi\rangle_s$, we entangle it with an ancillary qubit, or meter $|\psi\rangle_m$, which will be destructively measured. As an example take the signal qubit (acting as the control) in the unknown state $\alpha\,|\mathbf{0}\rangle + \beta\,|\mathbf{1}\rangle$ and interact it with the meter qubit (the target) prepared in the state $|\mathbf{0}\rangle$, in a CNOT gate. The action of the CNOT gate produces the

---

[3] For historical reasons 'spin' can be used to denote the value of any two-level quantum system, since the electron spin was the first physical system to exhibit the same symmetries associated with a qubit state.

following output,

$$U_{CNOT}(\alpha\,|\mathbf{0}\rangle_s + \beta\,|\mathbf{1}\rangle_s) \otimes |\mathbf{0}\rangle_m = \alpha\,|\mathbf{0}\rangle_s\,|\mathbf{0}\rangle_m + \beta\,|\mathbf{1}\rangle_s\,|\mathbf{1}\rangle_m\,, \tag{1.25}$$

which is a maximally entangled state. The fully destructive measurement of the meter will give '0' with probability $|\alpha|^2$ and therefore project the signal into the state $|\mathbf{0}\rangle$, or '1' with probability $|\beta|^2$, projecting the signal into the state $|\mathbf{1}\rangle$. A non-destructive measurement done in this way can be thought of as a perfect projection measurement of the signal qubit without destroying it. In the photonic architecture of quantum information processing this type of measurement is particularly important, since in the usual scenario one is forced to destroy the quantum information carrier (the photon), as a result of detection, in order to obtain information about the observable.

It should be noted that this type of measurement is entirely reliant upon the amount of entanglement between the signal and meter qubits after interaction in the two-qubit gate. To demonstrate this we consider preparing the meter in the state $(|\mathbf{0}\rangle + |\mathbf{1}\rangle)/\sqrt{2}$ which upon interaction in the CNOT gate with the unknown signal qubit gives

$$\frac{\alpha}{\sqrt{2}}\,|\mathbf{0}\rangle_s\,|\mathbf{0}\rangle_m + \frac{\alpha}{\sqrt{2}}\,|\mathbf{0}\rangle_s\,|\mathbf{1}\rangle_m + \frac{\beta}{\sqrt{2}}\,|\mathbf{1}\rangle_s\,|\mathbf{0}\rangle_s + \frac{\beta}{\sqrt{2}}\,|\mathbf{1}\rangle_s\,|\mathbf{1}\rangle_m\,. \tag{1.26}$$

This state exhibits no entanglement between signal and meter qubits, and a measurement of the meter simply renders the signal in its original input state [12, 13]. In general, the strength of the measurement can be continuously changed by altering the meter qubit state $|\psi\rangle_m = \gamma\,|\mathbf{0}\rangle + \bar{\gamma}\,|\mathbf{1}\rangle$, where $\gamma^2 + \bar{\gamma}^2 = 1$. In this case the strength of the measurement is governed by a knowledge parameter, $K = 2\gamma^2 - 1$ [13]. To gain maximum knowledge about the signal qubit we set $K=1$, (or equivalently $\gamma=1$), and minimum knowledge when $K=0$ $(\gamma = 1/\sqrt{2})$. When $0 < K < 1$ we refer to the measurement as a *weak* measurement, and in this framework they are generalisations of the non-destructive measurement [14].

Non-destructive measurements become particularly important in Chapter 4 where we are required to make two sequential measurements on a single qubit. The first measurement must necessarily be non-destructive in order to preserve the quantum system for the second measurement.

1.1.8 Quantum state tomography

The measurement of a single observable of an unknown quantum state is not enough to gain a full description of it. For instance, if we make a projective Pauli-Z measurement on the single qubit state $|\psi\rangle = (|\mathbf{0}\rangle + e^{i\phi}\,|\mathbf{1}\rangle)/\sqrt{2}$ we gain the outcomes '0' and '1' each with a probability 1/2 telling us that indeed the state is an equal superposition of $|\mathbf{0}\rangle$ and $|\mathbf{1}\rangle$, but this information tells us nothing about the the phase ϕ which could be anything between 0 and 2π. To gain full knowledge of an unknown quantum state we must perform multiple measurements in different bases in a protocol known as *state tomography* [5]. Intuitively quantum state tomography for a

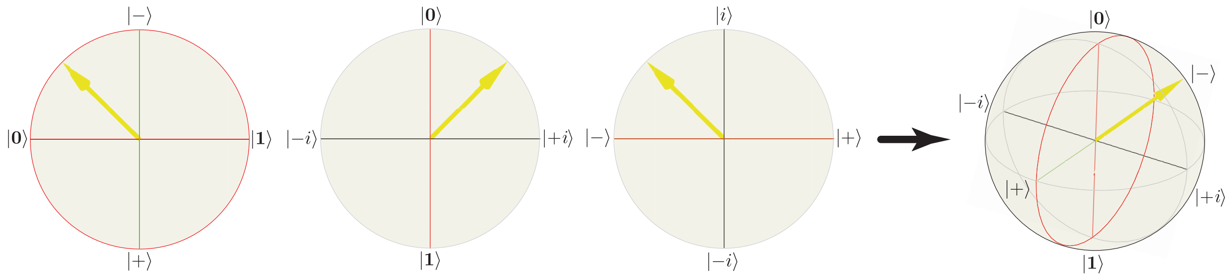

Figure 1.5: An intuitive picture of quantum state tomography of a qubit. Reconstructing a quantum state is done using multiple projective measurements onto different bases, or axes of the qubit sphere. This is equivalent to looking at the qubit sphere from different angles.

single qubit is like taking the qubit sphere and viewing it from different angles, a toy example is shown in Fig. 1.5.

Another requirement is that we have access to a large number of identically prepared copies of the unknown state $|\psi\rangle$ such that we can build up enough measurement statistics to estimate its state. If we had just a single copy of the unknown state it would be impossible to determine its exact state due to the restrictions placed upon us by Heisenberg's uncertainty principle.

Qubit state tomography

In the general case, for a d-dimensional system, we choose d^2 density operators,

$$|\psi_1\rangle\langle\psi_1|, \ldots, |\psi_{d^2}\rangle\langle\psi_{d^2}|, \tag{1.27}$$

which form a complete set over the space of d-dimensional matrices. For a single qubit which lives in a space with dimension d=2 the normalised Pauli operators, $X/\sqrt{2}$, $Y/\sqrt{2}$, $Z/\sqrt{2}$ and $I/\sqrt{2}$, form a complete set that span the Hilbert space of qubit states, such that an arbitrary qubit state (pure or mixed) can be written as

$$\rho = \frac{1}{2}(\sigma_0 + \vec{r}\cdot\vec{\sigma}), \tag{1.28}$$

where σ_0 and $\vec{\sigma}$=$(\sigma_1, \sigma_2, \sigma_3)$ are the Pauli operators (see Section 1.1.6) and $\vec{r}$=(r_x, r_y, r_z) is a vector in the qubit sphere given by r_i=$\mathrm{Tr}(\sigma_i\rho)$. Given n copies of the state ρ we can obtain the expectation values of the Pauli operators, $\mathrm{Tr}(\sigma_i\rho)$, by summing the measurement outcomes and dividing by n,

$$\langle\sigma_i\rangle = \mathrm{Tr}(\sigma_i\rho) = \sum_i^n \lambda_i/n, \tag{1.29}$$

where λ_i are the outcomes of each projective measurement (equal to the eigenvalue of the measurement operator, either $+1$ or -1). We then have an estimate of the state ρ given by,

$$\rho_{est} = \frac{1}{2}\sum_i \langle\sigma_i\rangle\sigma_i. \tag{1.30}$$

This is only an estimate because in reality the number of measurements we perform n, is finite and hence there is a finite error[4] associated with each expectation value $\langle\sigma_i\rangle$. As a consequence the estimated density operator ρ_{est} can sometimes lie outside the space of physically possible quantum states. Mathematically a non-physical density operator is one whose eigenvalues do not lie in the range $0 \leq \lambda \leq 1$ [15], it is said to be non-positive.

In these cases in order to attribute a physical quantum state to the measured system we use a *maximum likelihood* technique. This involves searching the entire space of physically possible quantum states to find the one that is *most likely* to produce the measured observables given in Eq.1.29. A more thorough discussion of maximum likelihood tomography can be found in references [15, 16].

---

[4] Since each measurement is independent, by the central limit theorem this error scales as $1/\sqrt{n}$.

References

[1] Feynman, R. P. Simulating physics with computers. *Int. J. Theor. Phys.* **21**, 467–488 (1982).

[2] Shor, P. Proc. 35th ann. symp. found. comp. sci. *IEEE Comp. Soc. Press* (1994).

[3] DiVincenzo, D. P. The physical implementation of quantum computation. *arXiv:quant-ph/0002077v3* (2000).

[4] Sakurai, J. J. *Modern Quantum Mechanics* (Addison Wesley, 1993).

[5] Nielsen, M. A. & Chuang, I. L. *Quantum Computation and Quantum Information* (Cambridge University Press, 2000).

[6] Zurek, W. H. Decoherence, Einselection and the existential interpretation (the rough guide). *Philosophical Transactions of the Royal Society of London. Series A: Mathematical, Physical and Engineering Sciences* **356**, 1793–1821 (1998).

[7] Steane, A. Quantum computing. *Reports on Progress in Physics* **61**, 117 (1998).

[8] Barenco, A. *et al.* Elementary gates for quantum computation. *Phys. Rev. A* **52**, 3457–3467 (1995).

[9] Lloyd, S. Almost any quantum logic gate is universal. *Phys. Rev. Lett.* **75**, 346–349 (1995).

[10] Deutsch, D., Barenco, A. & Ekert, A. Universality in quantum computation. *Proceedings of the Royal Society of London. Series A: Mathematical and Physical Sciences* **449**, 669–677 (1995).

[11] Dodd, J. L., Nielsen, M. A., Bremner, M. J. & Thew, R. T. Universal quantum computation and simulation using any entangling hamiltonian and local unitaries. *Phys. Rev. A* **65**, 040301 (2002).

[12] Ralph, T. C., Bartlett, S. D., O'Brien, J. L., Pryde, G. J. & Wiseman, H. M. Quantum nondemolition measurements for quantum information. *Phys. Rev. A* **73**, 012113 (2006).

[13] Pryde, G. J., O'Brien, J. L., White, A. G., Bartlett, S. D. & Ralph, T. C. Measuring a photonic qubit without destroying it. *Phys. Rev. Lett.* **92**, 190402 (2004).

[14] Aharonov, Y. & Vaidman, L. Properties of a quantum system during the time interval between two measurements. *Phys. Rev. A* **41**, 11–20 (1990).

[15] Langford, N. *Encoding, manipulating and measuring quantum information in optics*. Ph.D. thesis, University of Queensland (2007).

[16] James, D. F. V., Kwiat, P. G., Munro, W. J. & White, A. G. Measurement of qubits. *Phys. Rev. A* **64**, 052312 (2001).

CHAPTER 2

Quantum computing with photons

The mathematical constructs described in the last chapter can apply equally well to any discrete two-level quantum system: two well isolated energy levels of an atom [1], spin states of a single electron [2], or the flux quanta of a superconducting loop with a Josephson junction [3]. The commonality of all of these systems is the concept of quantisation—that some physical attributes of a system exist only in discrete units rather than continuously—an idea started with the discovery of photons.

2.1 Quantum physics with single photons

Photons are discrete packets of energy that make up the electromagnetic field [4, 5]. Their existence was originally proposed by Max Planck in a bid to solve the so called 'ultraviolet catastrophe' of the late 1800s. This puzzle was borne out of the original description of black body radiation given by the Rayleigh-Jeans law. It implied that the power per unit frequency increased beyond physicality as the frequency of light emitted from a black body increased. In 1900 Max Planck solved this issue by considering the energy radiating from the black body as made up of discrete packets of energy or quanta [4]. The concept of photons of light was later ironed out in 1905 by Einstein who used it to describe the photoelectric effect [5]. This leap from the Maxwellian description of light as a continuous field in space and time to discrete packets of energy localised in space and time is heralded as one of the founding discoveries leading to the birth of quantum mechanics.

After this time the world view of physics began to shift quite rapidly from classical to quantum. Old experiments such as Young's double slit were revived using single electrons [6], C_{60} molecules, so-called "buckyballs" [7] and more recently even larger molecules [8] to demonstrate the quantum phenomena of superposition and wave-particle duality. Surprisingly, it wasn't until 1986 that the quantisation of the light field was demonstrated conclusively via photon anti-correlation effects at a beam splitter [9]. Meanwhile, in 1981 Alain Aspect *et al.* [10] produced highly non-classical two-photon states to experimentally confirm what is considered the defining feature of quantum mechanics—entanglement (see Section 1.1.5).

The Aspect experiment made use of polarisation entangled two-photon states from an atomic cascade source. However, such sources are difficult to set up and give very low count rates, rendering experiments with 3 or more simultaneous photons near impossible. In comparison, what is now the most ubiquitous source of paired photons—spontaneous parametric downconversion (SPDC)—can be set up with ease and gives much higher count rates (see Section 2.2.5) of unentangled [11] and entangled photon states [12].

With a reliable, high-yielding and easy to use source of single photons the prospect of building useful devices to exploit the quantum nature of light became a real prospect for many scientists. Quantum computation is one such goal and we will now continue our discussion with the specifics of a photonic quantum computer.

2.2 Photonic quantum computing

The task of building a quantum computer is by no means an easy one. Most importantly there must be a quantum system that is simultaneously isolated from its environment and precisely controllable by its user. Herein lies the appeal of using light to store and manipulate quantum information. Photons are almost entirely free from decoherence: information can be stored in a photon for long times and therefore over long distances. This property makes them ideal for use in quantum communication protocols and such schemes are already commercially available [13]. However, the goal of quantum computation is different, here we want to interact carriers of quantum information, in an analogous way to classical logic gates, by using quantum logic gates (see Section 1.1.6). Encoding information into photonic qubits, and taking advantage of photon-photon interactions to perform quantum logic operations is one way of doing this and is the basis for the discrete variable approach to quantum computing with photons.

2.2.1 Photonic qubits

In Chapter 1 we discussed the properties of qubits without alluding to a specific physical architecture in which they can be realised. We will now discuss how a qubit state can be encoded using the quantised optical field. Although there are a variety of degrees of freedom which can be utilised to realise qubit states with photons we will only focus on the two that are important to understand this work, namely polarisation and dual-rail qubits. For a more comprehensive overview see references [14, 15, 16]. To start with we will review some of the basic nomenclature of quantum optics that will aid our discussion on photonic qubits.

Fock space

When dealing with discrete particles such as photons we work in a Hilbert space (defined in Section 1.1.1) known as Fock space. In Fock space we represent n particles in the mode k using the notation $|n_k\rangle$. The states in this space obey all the rules normally associated with a Hilbert space (see Section 1.1.1), that is,

$$\langle n_k | m_k \rangle = \delta_{nm} \qquad \text{and} \qquad \sum_{n_k=0}^{\infty} |n_k\rangle\langle n_k| = 1. \tag{2.1}$$

We operate on this space using the annihilation and creation operators (field operators) a_k and $a_k^\dagger$ respectively, which have the following effects on the number states $|n_k\rangle$,

$$\mathbf{a}_k\,|n_k\rangle=\sqrt{n_k}\,|n_k{-}1\rangle\,,\quad a_k^\dagger\,|n_k\rangle=\sqrt{n_k{+}1}\,|n_k{+}1\rangle\,,\quad a_k^\dagger a_k\,|n_k\rangle=n_k\,|n_k\rangle\,. \tag{2.2}$$

The number operator is given its own symbol $N_k{=}(a_k^\dagger a_k)$ [17]. Finally, when dealing specifically with photons we must employ Bosonic commutation relations between the creation and annihilation operators given by,

$$[a_k, a_{k'}] = [a_k^\dagger, a_{k'}^\dagger] = 0 \qquad [a_k, a_{k'}^\dagger] = \delta_{kk'}, \tag{2.3}$$

where the k's represent distinguishable modes. The most general form of a single particle state is that given by the coherent superposition in many distinguishable modes

$$|\psi_{single}\rangle = \left(\sum_k c_k a_k^\dagger\right)|0\rangle\,, \tag{2.4}$$

where $|0\rangle$ represents the vacuum state and $|c_k|^2$ is the normalised probability of finding the particle in the k^{th} mode, therefore $\sum_k |c_k|^2=1$ [14].

Single photons

The Hamiltonian that describes the quantised electromagnetic field in free space is given by

$$H = \sum_k \hbar\omega_k \left(a_k^\dagger a_k + \frac{1}{2}\right), \tag{2.5}$$

where ω_k is the angular frequency of the optical field in mode k [17]. To create a single photon we act on the vacuum mode $|0\rangle$ with the creation operator, such that at time t=0, the single photon state is $|\psi(0)\rangle=|1\rangle$. Solving the time-dependent Schrödinger equation we get,

$$|\psi(t)\rangle = e^{-i\omega_k t}\,|\psi(0)\rangle\,. \tag{2.6}$$

This is exactly what we expect for a single photon, that is, an excitation with a phase that changes at a rate given by the frequency of the excitation. Given this framework we will continue our discussion with the description of two important optical elements, the phase shifter and the beam splitter.

Phase shifters and beam splitters

The two crucial building blocks of a photonic quantum computer are the phase shifter which imparts a phase on a particular optical mode and the beam splitter that mixes multiple optical modes. Physically a phase shifter is a material, with length L, which has a different index of refraction n', to that of its surroundings n. When the optical field passes through such a material it picks up a phase shift ϕ, proportional to the refractive index contrast given by,

$$\phi = \frac{(n' - n)\omega_k L}{c}, \tag{2.7}$$

where c is the speed of light. The phase shifter acting on a single optical mode is described by the interaction Hamiltonian $H_{PS}{=}-\hbar\phi a_k^\dagger a_k$. Importantly, this Hamiltonian commutes with the photon number operator N_k, that is, $[H_{PS}, N_k]{=}0$, meaning it conserves photon number therefore giving the unitary transformation,

$$U_{PS} = e^{i\phi a_k^\dagger a_k}. \tag{2.8}$$

The operators $a_k^\dagger$ and a_k are effected under the transform $a_{out}{=}U_{PS}a_{in}U_{PS}^\dagger$, such that [16],

$$a_{out}^\dagger = e^{i\phi a_{in}^\dagger a_{in}} a_{in}^\dagger e^{-i\phi a_{in}^\dagger a_{in}} = e^{i\phi} a_{in}^\dagger. \tag{2.9}$$

To describe the beam splitters we introduce two distinct optical modes 1 and 2 with creation (annihilation) operators $a_1^\dagger(a_1)$ and $a_2^\dagger(a_2)$ respectively. The beam splitter Hamiltonian is $H{=}\theta e^{i\phi}a_1 a_2^\dagger - \theta e^{-i\phi}a_1^\dagger a_2$, which mixes the two modes with a weighting θ. It follows that,

$$\begin{aligned} a_{1,out}^\dagger &= \cos\theta a_{1,in}^\dagger + ie^{-i\phi}\sin\theta a_{2,in}^\dagger \\ a_{2,out}^\dagger &= ie^{i\phi}\sin\theta a_{1,in}^\dagger + \cos\theta a_{2,in}^\dagger. \end{aligned} \tag{2.10}$$

Physically a beam splitter is a dielectric medium which is partly reflective and partly transmissive. In practice we talk of beam splitter reflectivities and transmissivities, given by $\eta{=}\sin^2\theta$ and $1{-}\eta{=}\cos^2\theta$, respectively. The phase factors $ie^{\pm i\phi}$ ensure that the transformation conserves photon number and therefore unitarity [16].

2.2.2 Encoding and manipulating photonic qubits

We can encode qubits onto a single photon by choosing two distinguishable (orthogonal) optical modes represented by the creation and annihilation operators $a_1^\dagger, a_2^\dagger$ and a_1, a_2 respectively. Importantly, the modes 1 and 2 represent two entirely distinguishable states of a two-level photonic degree of freedom e.g. the polarisation. In equivalent notations, an arbitrary qubit state is given by,

$$\left(\alpha a_1^\dagger + \beta a_2^\dagger\right)|0\rangle = \alpha \begin{bmatrix} 1 \\ 0 \end{bmatrix} + \beta \begin{bmatrix} 0 \\ 1 \end{bmatrix}. \tag{2.11}$$

Using the matrix notation we can define both phase shifters and beam splitters as rotations of a qubit state on the qubit sphere (see discussion in Section 1.1.6). The phase shifter is equivalent to a rotation about the z-axis on the qubit sphere, given in matrix form as,

$$R_z(\phi) = e^{-i\phi\sigma_3/2} = \begin{bmatrix} e^{-i\phi/2} & 0 \\ 0 & e^{i\phi/2} \end{bmatrix}, \tag{2.12}$$

where σ_3 is the Pauli-Z operator. And the beam splitter operation is given by a rotation about the y-axis of the qubit sphere,

$$R_y(\theta) = e^{-i\theta\sigma_2} = \begin{bmatrix} \cos\theta & \sin\theta \\ -\sin\theta & \cos\theta \end{bmatrix}, \tag{2.13}$$

where σ_2 is the Pauli-Y operator, and we have chosen the phase of the beam splitter, $\phi{=}\pi/2$. The two operators, $R_z(\phi)$ and $R_y(\theta)$ are sufficient for performing an arbitrary single-qubit unitary, given by the Z-Y decomposition [15],

$$U = e^{i\alpha}R_z(\beta)R_y(\gamma)R_z(\delta), \tag{2.14}$$

where α, β, γ and δ are real numbers. Suffice to say that all single qubit unitaries can be decomposed as a series of phase shifters and beam splitters [15].

Polarisation qubits

Polarisation refers to the direction of oscillation of the electric field component of the optical field, see see Fig 2.1. It is a two-level quantum system that possesses identical symmetry properties to those of qubits. Therefore the polarisation states can be mapped directly onto the qubit sphere[1]. Traditionally, we take the horizontally and vertically polarised states to represent the computational basis, that is $|H\rangle = |\mathbf{0}\rangle$ and $|V\rangle = |\mathbf{1}\rangle$ respectively. In the Fock state picture, an arbitrary polarisation qubit is written as,

$$|\psi\rangle = \left(\alpha a_H^\dagger + \beta a_V^\dagger\right)|0\rangle = \alpha\,|H\rangle + \beta\,|V\rangle\,, \tag{2.15}$$

where $a_H^\dagger$ and $a_V^\dagger$ are the creation operators for horizontally and vertically polarised modes respectively and $|0\rangle$ is the vacuum state.

Manipulating polarisation in the lab is done using birefringent materials: materials whose property of refraction is anisotropic and therefore dependent on the polarisation direction of the input field. In particular, birefringent materials display two different indices of refraction n_o and n_e, for *ordinary*- and *extraordinary*-waves, polarised along and perpendicular to the optic axis respectively [18] . From these materials a wide variety of polarising optics can be made including wave plates that rotate the direction of polarisation and polarisers that reflect and transmit specific polarisations. For a full description of these optics refer to reference [18].

In polarisation encoding, single qubit unitaries are performed with half- and quarter-wave plates (HWP and QWP respectively). Wave plates are made from thin pieces of birefringent material, usually calcite ($CaCO_3$). When light passes through a wave plate the two orthogonal components of the electric field, e and o, travel through at varying speeds leading to a phase shift between them and a resulting change to the polarisation. When the extraordinary wave is aligned with the optic axis of the birefringent material, half- and quarter-wave plates introduce

---

[1] For historical reasons the equivalent of the qubit sphere for polarisation is called the Poincaré sphere. The two names will be used interchangeably throughout this thesis.

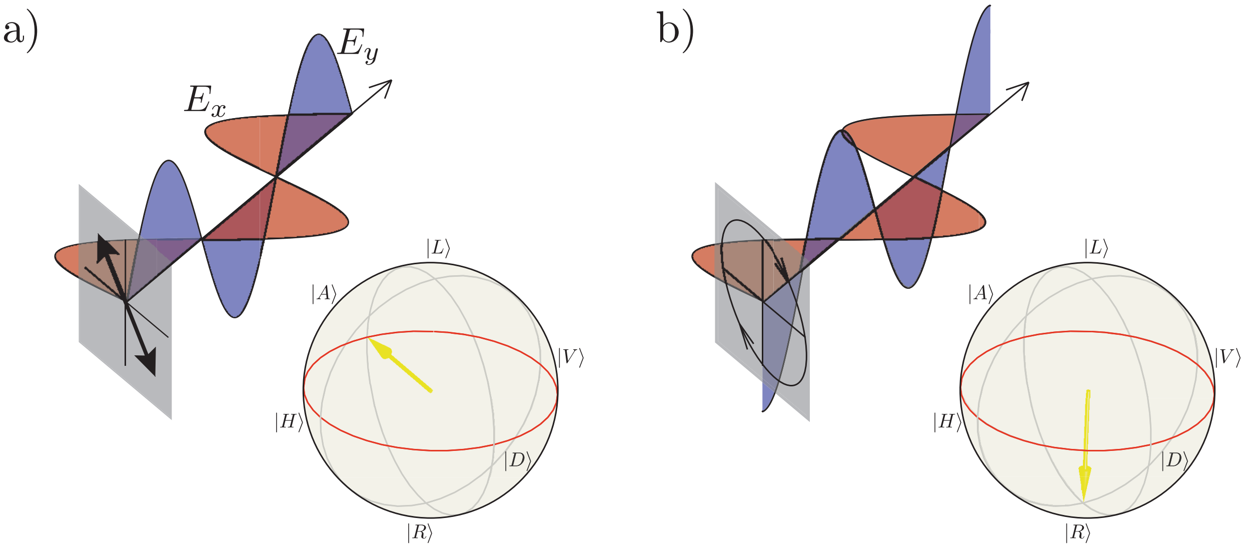

Figure 2.1: Polarisation of the light field. The two orthogonal components of the electric field, E_x and E_y shown in red and blue respectively, specify the resulting direction of the electric field oscillation. In a) the E_x and E_y components of the electric field are out of phase by $-\pi$ to give the anti-diagonal state $|A\rangle = \frac{1}{\sqrt{2}}(|H\rangle - |V\rangle)$, in b) E_x and E_y have a phase difference of $-\pi/2$ to give the right-circularly polarised state, $|R\rangle = \frac{1}{\sqrt{2}}(|H\rangle - i|V\rangle)$.

π and $\pi/2$ phase shifts respectively, between the incoming extraordinary (e) and ordinary (o) waves. That is, in the frame of reference of the wave plate, HWPs and QWPs perform the following unitaries,

$$\begin{aligned} U_{HWP} &= R_z(\pi) = \begin{bmatrix} -i & 0 \\ 0 & i \end{bmatrix} \\ U_{QWP} &= R_z(\pi/2) = \frac{1}{\sqrt{2}} \begin{bmatrix} 1-i & 0 \\ 0 & 1+i \end{bmatrix}. \end{aligned} \tag{2.16}$$

If both of the optical elements are made of the same material, and therefore have the same n_o and n_e, the only difference between them is their thickness, which from Eq. 2.7 gives the variation in phase shift.

We describe the phase shift imparted between the e- and o-waves in the reference frame of the wave plate itself, however when describing the system in the laboratory reference frame we use the horizontally and vertically polarised states which are related by a physical rotation in space $R(\theta)$ given by,

$$R(\theta) = \begin{bmatrix} \cos\theta & \sin\theta \\ -\sin\theta & \cos\theta \end{bmatrix}, \tag{2.17}$$

where θ is the physical angle of the optic-axis with respect to the horizontal axis in the laboratory frame of reference [14]. Notice that although this rotation is a physical one it is similar to the beam splitter rotation $R_y(\theta)$ given in Eq. 2.13. We therefore interpret this rotation as

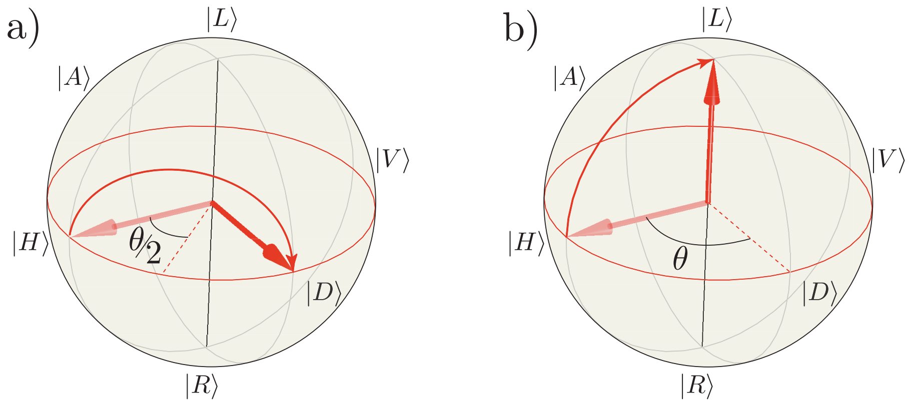

Figure 2.2: The action of wave plates represented on the qubit sphere. a) A half-wave plate implements a $\pi/2$ rotation about an axis defined in the real plane indicated by the red dashed line. b) A quarter wave plate does a $\pi/4$ rotation. In both cases θ is the physical rotation angle of the wave plate with respect to the optic axis in the laboratory frame of reference.

a change of reference frame. The operation of a wave plate in the laboratory frame can be built up as follows i) rotate into the wave plate frame of reference, ii) implement the desired wave plate unitary and finally iii) rotate back to the laboratory frame of references. For a wave plate rotated at an angle θ with respect to laboratory frame the HWP and QWP perform the following unitaries [14],

$$\begin{aligned} U_{HWP}(\theta) &= -i\begin{bmatrix} \cos 2\theta & \sin 2\theta \\ \sin 2\theta & -\cos 2\theta \end{bmatrix} \\ U_{QWP}(\theta) &= \frac{1}{\sqrt{2}}\begin{bmatrix} 1+i\cos 2\theta & i\sin 2\theta \\ i\sin 2\theta & 1-i\cos 2\theta \end{bmatrix}. \end{aligned} \tag{2.18}$$

Examples of their actions on states on the qubit sphere are shown in Fig 2.2. Using a combination of half-wave and quarter-wave plates allows one to change any state on the qubit sphere to any other state: they can form a universal single qubit unitary. In fact is has been shown that a combination of one half-wave plate and two quarter-wave plates in *any* order, is sufficient to realise a universal single qubit unitary up to a phase factor [19]. Of course, in practice a wave plate will not implement the exact rotations shown in Eqs. 2.18. For further discussion on real wave plates see reference [14].

Dual-rail encoded qubits

In dual rail the qubit state is represented by the photon number occupation in two orthogonal optical modes. If a photon is in optical mode x we assign it the state $|10\rangle = |1\rangle_x \otimes |0\rangle_y$ and likewise when the photon is in optical mode y, $|01\rangle = |0\rangle_x \otimes |1\rangle_y$. Importantly, x and y can be *any* two orthogonal states of the light field, for example polarisation. Polarising beam splitters spatially separate the incoming optical field into its orthogonal polarisation states to give an equivalent representation of the qubit in the longitudinal dual-rail representation, that is orthogonal qubit states in separate longitudinal-spatial modes. This mapping from the polarisation states to two orthogonal longitudinal-spatial modes x and y, is given by

$$\begin{aligned} |10\rangle_{HV} &\rightarrow |10\rangle_{xy} \\ |01\rangle_{HV} &\rightarrow |01\rangle_{xy} . \end{aligned} \tag{2.19}$$

Conventionally these dual-rail states are equivalent to the computational basis states, that is, $|\mathbf{0}\rangle = |10\rangle$ and $|\mathbf{1}\rangle = |01\rangle$. The joint state of two qubits in the dual-rail representation lives in a Hilbert space spanned by the four (unnormalised) basis states $|1010\rangle$, $|1001\rangle$, $|0110\rangle$ and $|0101\rangle$, in the basis $|x_1 y_1 x_2 y_2\rangle$, where x_1 is photon 1 in mode x.

2.2.3 Nonlinear optical quantum gates

As discussed in Section 1.1.6 one of the fundamental building blocks of a universal quantum computer is an entangling two-qubit quantum gate. The controlled-SIGN (CZ) gate, which given the correct input states can produce a maximally entangled two-qubit state, is defined as having the following operation in the computational basis,

$$U_{CZ} |x\rangle |y\rangle = (-1)^{x \cdot y} |x\rangle |y\rangle . \tag{2.20}$$

In other words, when both $x, y {=} \mathbf{1}$, meaning that both photons are in the optical mode ‘1’, the joint state is subject to a π phase shift (since $e^{i\pi} {=} -1$).

One way to implement such an interaction is via an optical Kerr nonlinearity in a nonlinear dielectric material. These materials exhibit a refractive index n_r, which is proportional to the input optical field intensity, such that

$$n_r = n_0 + \chi' E^2, \tag{2.21}$$

where n_0 is the ordinary refractive index and the proportionality constant χ', is related to the third-order susceptibility of the material. This change in refractive index induces an intensity-dependent phase shift by two distinct mechanisms. The first is referred to as a *self-phase modulation* in which the intensity of a single beam induces a phase shift upon itself, and the second is called the *cross*-Kerr effect and refers to a signal (probe) optical mode inducing a phase shift upon a separate probe (signal) mode [16]. The cross-Kerr effect produces an intensity dependent phase shift, between optical modes 1 and 2 by mediating the following interaction Hamiltonian

$$H_{Kerr} = \hbar \chi a_1^\dagger a_1 a_2^\dagger a_2, \tag{2.22}$$

where χ is proportional to the third-order susceptibility and $(a_1^\dagger a_1)$ and $(a_2^\dagger a_2)$ are the number operators for optical modes 1 and 2 respectively [17].

Figure 2.3 shows how this nonlinear optical effect could be used in principle for an entangling quantum gate between two single photon qubits. The cross-Kerr effect for two single photon

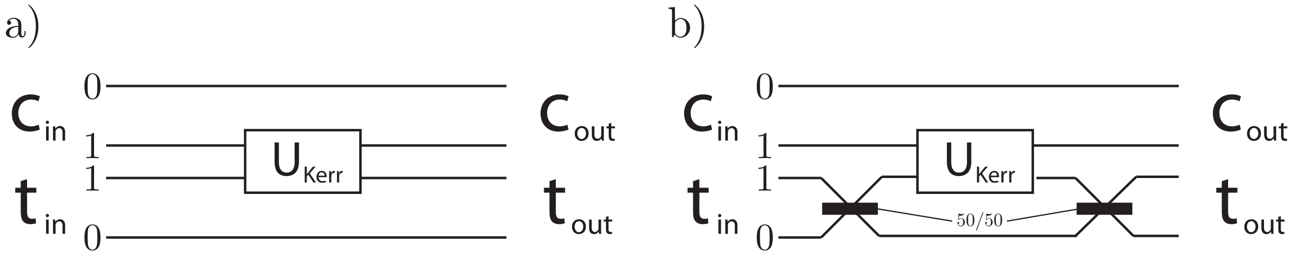

Figure 2.3: Using Kerr nonlinearities for entangling quantum gates. a) Two single photons, prepared as dual rail qubits, are subject to the cross-Kerr effect when they are both present in mode '1'. When the phase shift induced by the cross-Kerr effect is equal to π, or equivalently $e^{i\chi t}=-1$ this gate is equivalent to a CZ operation between the two qubits. b) Two 50/50 beam splitters placed either side of the target qubit transforms the CZ into a CNOT gate.

qubits is described by the following unitary evolution

$$U_{Kerr}\left|x\right\rangle\left|y\right\rangle = e^{-ix\cdot y\chi t}\left|x\right\rangle\left|y\right\rangle . \tag{2.23}$$

Hence, the size of the induced phase shift is directly proportional to both χ and the interaction time t.

The gate in Fig. 2.3a shows two single photons, one acting as the control qubit and the other as the target qubit, that are subject to the phase shift induced by the cross-Kerr effect only if they are both in optical mode '1'. This is similar to the phase shift operation required for the CZ gate given in Eq. 2.20. An entangled state can be produced by preparing both the control and target qubits in an equal superposition of their respective '0' and '1' modes giving the following output,

$$\frac{\left|\mathbf{0}\right\rangle_c\left|\mathbf{0}\right\rangle_t + \left|\mathbf{0}\right\rangle_c\left|\mathbf{1}\right\rangle_t + \left|\mathbf{1}\right\rangle_c\left|\mathbf{0}\right\rangle_t + e^{-i\chi t}\left|\mathbf{1}\right\rangle_c\left|\mathbf{1}\right\rangle_t}{2}. \tag{2.24}$$

In the case where $e^{i\chi t}=-1$ this state is a maximally entangled state. Quantum gates based on Kerr-nonlinearities were first proposed by Yamamoto [20] and Milburn [21]. More recent studies by Hutchinson and Milburn [22] detail how Kerr-nonlinearities can be exploited for building up large multipartite entangled states called *cluster states*, which have been shown to be a powerful resource in the measurement based scheme of quantum computing [23].

One of the major advantages that this system has over other optical quantum computing schemes is that it is deterministic. As we will see in the next section the linear optics scheme for quantum computing relies on quantum logic gates that are inherently non-deterministic. That is, in order to know whether the logic gate has worked or not one is forced to measure and therefore destroy the output photons which carry the crucial quantum information. This problem can be circumvented with the addition of ancilla photons, but more on this later.

Inducing a phase shift of the order of π using a cross-Kerr nonlinearity is difficult due to the lack of materials that exhibit strong enough third order susceptibilities. Currently the best reported phase shift induced by a single photon in a nonlinear optical material was measured to be of the order of $\sim 10^{-7}$ rads [24]. In this work they measure the single photon induced phase shift in a photonic crystal optical fibre and claim that a fibre length of a few kilometres with losses of $\sim$ 1dBkm^{-1} would still only result in phase shifts of $\sim 10^{-4}$ rads. In addition to the small nonlinearities of known materials the task of producing well defined single Fock photon states is itself a difficult problem. We will discuss this issue more in Section 2.2.5 and in much greater detail in Chapter 3.

2.2.4 Linear optics quantum computing

We have discussed how single qubit gates can be implemented using basic linear optics elements equivalent to phase shifters and beam splitters, but what about multiple qubit gates? In Section 1.1.6 we discussed how quantum logic gates can in theory be used to create maximally entangled bipartite states, and in the previous section we showed that creating such states is currently infeasible using nonlinear optics techniques. We will now discuss the alternative: linear optics quantum computing.

In 2001 Knill, Laflamme and Milburn (KLM) proposed a scheme for deterministic quantum computation using only single photon sources and detectors, and linear optical networks [25]. The scheme relies heavily on off-line resources such as ancilla photons and entanglement to combat the inherent non-deterministic nature of a single linear optics quantum logic gate. These extra required resources make the task of building a scalable quantum computer with linear optics a hard one. Despite this the first proof of principle two-qubit quantum logic gate, the controlled-NOT, was experimentally demonstrated with linear optics in 2003 by O'Brien *et al.* [26]. Since then more two-photon gates [27, 28, 29, 30, 31] and the three-photon Toffoli [32] gate have been realised inside the lab. In a next step towards quantum computation with single photons, demonstrations of Shor's algorithm first in free space [33, 34] and more recently with silica-on-silicon waveguides circuits [35], show promise for this system as a tool in quantum computation.

As we saw in the previous section, implementing a CZ gate with single photons requires that the presence of one photon affects the state of another in a nonlinear fashion. In nonlinear optics this interaction could be mediated deterministically through the use of the cross-Kerr effect. The breakthrough in the linear optics KLM scheme is that a nonlinearity can arise by means of measurement [25]. Central to the understanding of the KLM scheme is the way in which photons themselves interact via linear optics, which is the subject of the next section.

Photon-photon interaction

On a qualitative level single photons interact with the universe in much the same way that classical fields do, they are subject to absorption and scattering with matter and interference with themselves. Where they differ significantly from classical fields is their interaction with other single photons, exemplified by the interference of two single photons at a beam splitter, see Fig. 2.4.

Consider two single photon qubits $|\psi_1\rangle$ and $|\psi_2\rangle$, represented in dual-rail as,

$$\begin{aligned} |\psi_1\rangle &= a_1^\dagger |00\rangle = |10\rangle \\ |\psi_2\rangle &= a_2^\dagger |00\rangle = |01\rangle . \end{aligned} \tag{2.25}$$

From Eq. 1.6 the total state of this system is given by the tensor product of the two qubits $|\psi_T\rangle = |\psi_1\rangle \otimes |\psi_2\rangle$. The action of a beam splitter on the two qubits is given by the tensor product of the individual beam splitter operations for each mode given in Eq. 2.13, that is

$$\begin{aligned} U_{BS}^{(2)} &= U_{BS} \otimes U_{BS} \\ &= \begin{bmatrix} tt & tr & rt & rr \\ -tr & tt & -rr & rt \\ -rt & -rr & tt & tr \\ rr & -rt & -tr & tt \end{bmatrix}, \end{aligned} \tag{2.26}$$

where $r{=}\sqrt{\eta}$ and $t{=}\sqrt{1-\eta}$ are the reflectivity and transmissivity of the beam splitter respectively. Acting on the two-qubit state $|\psi_T\rangle$ we have,

$$\begin{aligned} U_{BS}^{(2)} |\psi_T\rangle &= \begin{bmatrix} tt & tr & rt & rr \\ -tr & tt & -rr & rt \\ -rt & -rr & tt & tr \\ rr & -rt & -tr & tt \end{bmatrix} \begin{bmatrix} 0 \\ 1 \\ 0 \\ 0 \end{bmatrix} \\ &= \begin{bmatrix} tr \\ tt \\ -rr \\ -rt \end{bmatrix} . \end{aligned} \tag{2.27}$$

Substituting $r{=}\sqrt{\eta}$ and $t{=}\sqrt{1-\eta}$ we have the final output state,

$$\sqrt{\eta(1-\eta)}\,(|1010\rangle - |0101\rangle) + (1-\eta)\,|1001\rangle - \eta\,|0110\rangle . \tag{2.28}$$

If the photons are entirely indistinguishable, the Bosonic commutation relations ensure that the states $|1001\rangle$ and $|0110\rangle$ are symmetric under the exchange of photons 1 and 2. Therefore, in general we have,

$$\sqrt{2\eta(1-\eta)}\,(|20\rangle - |02\rangle) + (1-2\eta)\,|11\rangle , \tag{2.29}$$

where $|1010\rangle = a_1^\dagger a_1^\dagger |00\rangle$, $|0101\rangle = a_2^\dagger a_2^\dagger |00\rangle$ and $|1001\rangle = a_1^\dagger a_2^\dagger |00\rangle$. However, in the special case of a 50/50 beam splitter, where $r = t = 1/\sqrt{2}$, we have the state

$$\frac{a_1^\dagger a_1^\dagger |00\rangle - a_2^\dagger a_2^\dagger |00\rangle}{2} = \frac{|20\rangle - |02\rangle}{\sqrt{2}}, \tag{2.30}$$

The right hand side is the equivalent state represented in the number basis. Therefore, when

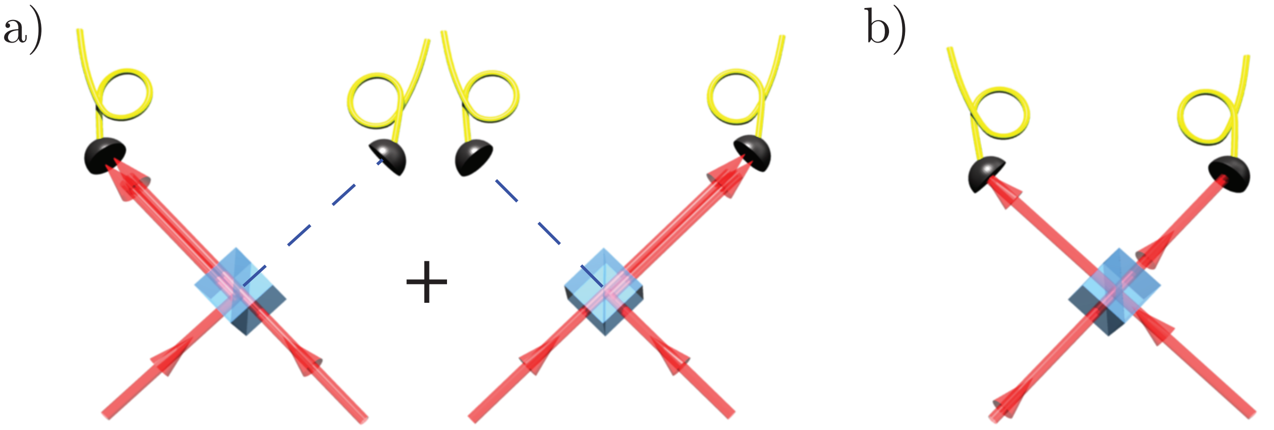

Figure 2.4: Schematic representation of a Hong-Ou-Mandel experiment. a) Two photons arrive at the beam splitter simultaneously and bunch at the output ports. b) Two photons injected into the 50/50 beam splitter are temporally delayed and therefore distinguishable: no photon bunching is observed at the output detectors.

two perfectly indistinguishable photons arrive at a 50/50 beam splitter at the same time they ‘bunch’ together and leave via the same optical port. Using single photon detectors at each output of the beam splitter one can observe how the number of coincident events changes as the overlap between incoming photons is altered. Due to the bunching effect, when the photons are maximally overlapped the coincidence rate drops to a minimum. A setup of such an experiment is illustrated in Fig. 2.4a and an example of real experimental data is shown in Fig. 2.5. The effect known as non-classical, or Hong-Ou-Mandel (HOM) interference, named after those who first observed it [36], is a direct consequence of the Bosonic commutation relationship (see Eq. 2.2), and is one of the key differences between classical and quantum light fields.

Mastering HOM interference is a challenge for experimental physicists and requires careful optical alignment and photon source engineering [37]. Temporal and spatial mode mismatch, frequency or polarisation non-degeneracy, and photon number purity all contribute to the distinguishability of the input photons which will ultimately be seen as a drop in the contrast or visibility of interference, defined as

$$\mathcal{V} = \frac{P_{out} - P_{in}}{P_{out}} \tag{2.31}$$

where P_{out} and P_{in} are the probabilities of detecting a coincident photon pair at the outputs of the beam splitter inside (maximum overlap, Fig 2.4a) and outside (far from maximum overlap, Fig 2.4b) the HOM interference dip, respectively.

Hong-Ou-Mandel interference is one key ingredient in performing multi-qubit quantum gates with linear optics. The other ingredient is measurement. Measurement introduces the non-linearity required to affect the controlled operations between multiple qubits detailed in Section 1.1.6. As it is used multiple times throughout this thesis, we will now detail the operation of a linear optics CZ gate based on the KLM scheme of linear optics quantum logic gates.

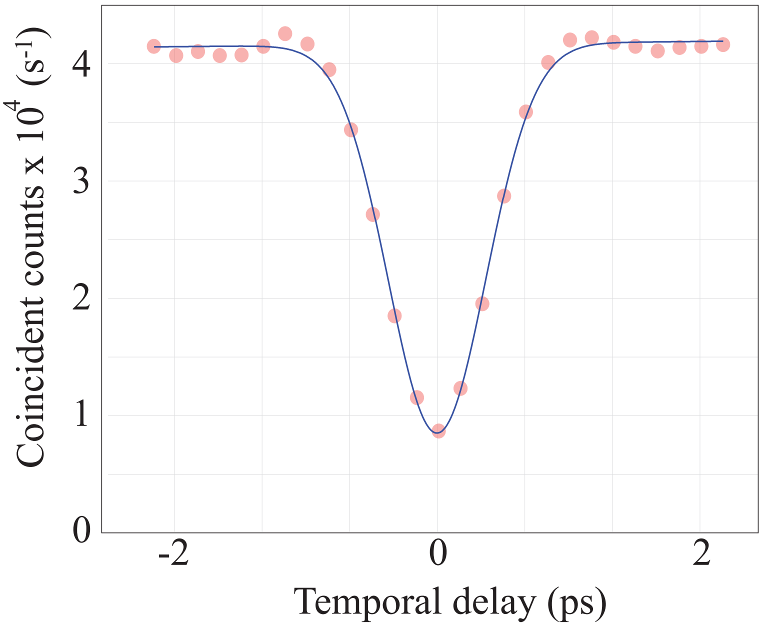

Figure 2.5: Experimental data showing coincidence counts vs temporal delay between two photons at a 50/50 beam splitter, the corresponding experimental schematic is shown in Fig. 2.4. This data was taken using two triggered photons from two independent photon sources (see Section 2.2.5). The red markers show experimental data with Poissonian errors smaller than the marker size. The calculated visibility in this case is 81 ± 2%, demonstrating that the photons are not entirely indistinguishable.

The linear optics CZ gate

In 2002 a linear optics version of the CNOT and CZ gate was proposed by Ralph *et al.* [38] and Hofmann *et al.* [39] respectively. The mechanism by which they operate are identical, relying on the non-classical interference of two vertically polarised photon modes at a beam splitter with a reflectivity of η=1/3. The operation of the gate is best understood in the dual-rail picture, which is shown schematically in Fig 2.6a.

Importantly, the gate only operates in *post-selection*, that is, only if one photon is output in each mode $\mathrm{c}_{\mathrm{out}}$ and $\mathrm{t}_{\mathrm{out}}$ does the circuit operate as a CZ gate. Its operation can be understood as follows. If the control is prepared in the horizontally polarised state occupying mode c_{H}, no interaction between the control and target can occur such that a coincidence is detected at both the output ports. However, when the control photon is in the mode c_{V} it can interact with the vertically polarised mode of the target qubit t_{V} at the central 1/3 beam splitter. This non-classical interference causes a π phase shift between the control and target qubits when they leave the gate via *different* output ports.

As the gate is operated in post-selection, for vertically polarised input photons we disregard all instances when both photons leave via the same optical port, these account for exactly 8/9 of all events. To balance this loss for the horizontally polarised inputs, two extra 1/3 beam splitters attenuate the c_{H} and t_{H} modes. The gate therefore has a success probability of 1/9.

In practice this type of gate is difficult to realise using dual-rail encoding. Not only are the

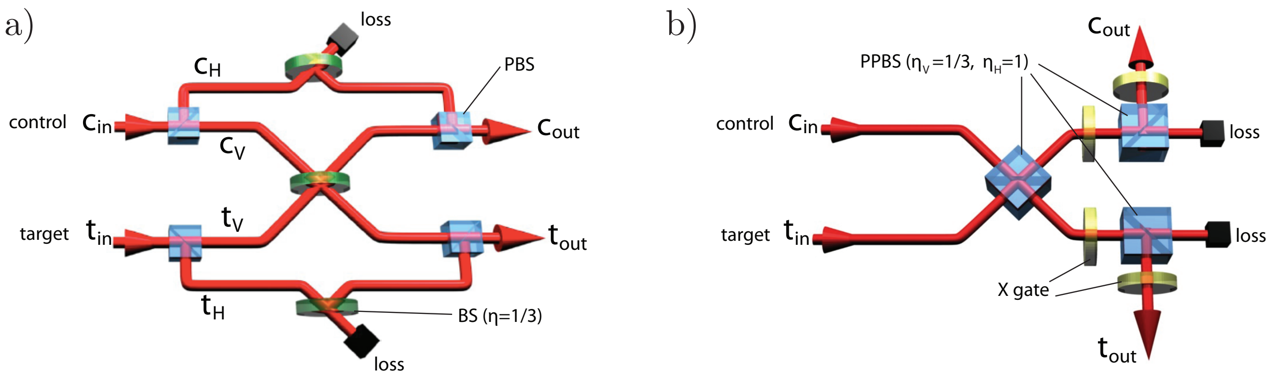

Figure 2.6: The CZ gate in detail a) dual rail representation using three η=1/3 non-polarising beam splitters (BS) and b) using an entirely polarisation encoded setup with a single partially polarising beam splitter (PPBS) with reflectivities $\eta_V = 1/3$ and $\eta_H = 1$ for horizontal and vertical polarised light respectively [27, 30, 31]. An additional wave plates doing a Pauli-X operation, and identical PPBSs at the output balance the loss for the horizontally polarised modes. In both setups, quantum interference results in a relative π phase shift of the vertical polarisation components, $c_V t_V$. The correct functioning is heralded by a coincidence count between the two outputs, $\mathrm{c_{out}}$ and $\mathrm{t_{out}}$, which occurs with probability 1/9.

optical paths difficult to align, but due to the classical interferometers required between the control and target modes, physical drift can hamper the overall characterisation of the gate operation. Despite these issues the first demonstration of this gate using this configuration was implemented in 2003 by O'Brien *et al.* [26].

Subsequently a new design of this gate based entirely on polarisation encoding was developed by Langford [27], Kiesel [30] and Okamoto [31], see Fig. 2.6b. The gate operates in an identical fashion as its predecessor, except here the entire gate setup is realised using polarisation encoded photons, not longitudinal spatial-mode, therefore circumventing the need for highly stabilised classical interferometers. The trick is to use a partially polarising beam splitter (PPBS), one that has different reflectivities for orthogonal polarisation modes H and V.

Although in linear optics schemes two-photon quantum gates cannot be performed deterministically without the addition of extra ancillary photon resources [25], non-deterministic gates are useful for demonstrating proof-of-principle photonic quantum logic, generating entangled states and performing non-destructive measurements. All such experiments can employ the use of the linear optics CZ gate, which we use experimentally in Chapters 3 and 4.

All of the theoretical proposals for scalable photonic quantum computing assume the availability of single photon Fock states, whereas state-of-the-art demonstrations in this field use spontaneous parametric downconversion (SPDC) as the photon source which only approximates a true single photon states [40]. Finally, for the remainder of this chapter we will discuss this method for the creation of single photon states.

2.2.5 An approximate single photon source: Spontaneous parametric downconversion

Every experiment in this thesis makes use of pairs of single photons produced via spontaneous parametric downconversion (SPDC). First observed in the 1970s [11], SPDC has proved an invaluable tool in fundamental science, from Bell tests [41] to quantum computing [26, 27, 28, 29, 32, 33], as well as in more practical applications such as quantum key distribution [42] and quantum metrology [43]. The advantages of SPDC sources are numerous: they are easy to set up, can be operated at room temperature and with sturdy optical alignment can provide a steady flow of single photons for days.

SPDC is a process whereby one high energy pump photon decays into two lower energy daughter photons—traditionally called *signal* and *idler*—obeying both energy and momentum conservation. The process occurs in a nonlinear optical medium, one whose polarisation P has a nonlinear dependence on the input electric field amplitude,

$$P = \chi^{(1)}E + \chi^{(2)}E^2 + \chi^{(3)}E^3..., \tag{2.32}$$

where $\chi^{(i)}$ us the i^{th}-order susceptibility of the optical medium and we have only considered the electric field contribution of the polarisability [44]. When the electric field in the above equation is sinusoidal in time a polarisation wave is established in the medium which has a non-zero coupling between the fundamental frequency of the input field with its subharmonics (and visa-versa in the case of second harmonic generation) [45]. In the case of SPDC there is a $\chi^{(2)}$ nonlinearity that gives rise to a three-wave mixing process between the pump field, ω_p and the two down-converted fields, ω_s and ω_i, called the *signal* and *idler* respectively, where $\omega_p = \omega_s + \omega_i$.

Phase matching and the geometry of SPDC

In addition to conservation of energy expressed as, $\omega_p = \omega_s + \omega_i$, the three fields involved in SPDC should conserve momentum, that is, their wave vectors should satisfy

$$\vec{k}_p = \vec{k}_s + \vec{k}_i. \tag{2.33}$$

Importantly, for a maximum energy transfer between the pump field and the down-converted fields, the polarisation wave that is set up by the pump beam in the nonlinear medium must be phase coherent with the resulting down converted fields [44]. Since the wave vectors involved are determined by the refractive indices of the material the following relation must hold for efficient energy transfer [46]

$$n_p\omega_p = n_s\omega_s + n_i\omega_i. \tag{2.34}$$

With these conditions the system is said to be *phase matched* [44]. Neglecting factors such as anomalous dispersion and birefringence for now, in the case of normally dispersive materials, that is $\frac{dn}{d\omega} > 0$, the conditions in Eq. 2.34 are impossible to meet. To show this we examine the

	Positive uniaxial ($n_e > n_o$)	Negative uniaxial ($n_e < n_o$)
Type-I	$n_p^o\omega_p = n_i^e\omega_i + n_s^e\omega_s$	$n_p^e\omega_p = n_i^o\omega_i + n_s^o\omega_s$
Type-II	$n_p^o\omega_p = n_i^o\omega_i + n_s^e\omega_s$	$n_p^o\omega_p = n_i^e\omega_i + n_s^o\omega_s$

Table 2.1: Phase matching conditions for type-I and type-II $\chi^{(2)}$ processes in a nonlinear medium with uniaxial birefringence.

refractive index differences $n_p - n_s$ and $n_p - n_i$, which are given by,

$$n_p - n_s = \frac{(n_i - n_s)\omega_i}{\omega_p} \tag{2.35}$$

$$n_p - n_i = \frac{(n_s - n_i)\omega_s}{\omega_p}. \tag{2.36}$$

Since for normally dispersive materials the left-hand-sides of these equations are always positive, both of them cannot be simultaneously satisfied for any choice of ω_s and ω_i [44]. The phase matching condition in Eq. 2.34 can be satisfied however, by making use of the birefringence of a nonlinear material, that is, the difference in refractive index dependent upon the polarisation of the various optical fields.

There are many different phase matching conditions that can be achieved in birefringent materials, depending upon the pump polarisation and the type of birefringence in the nonlinear medium. An in-depth discussion of all of them is beyond the scope of this thesis, for a more comprehensive overview see references [44, 47, 46]. The simplest case of phase matching in a $\chi^{(2)}$ media is understood in uniaxial birefringent materials. Table 2.1 lists the types of phase matching that are possible in these systems [44, 47]. Most of the experiments in this thesis employ Type-I phase matching in β-barium borate (BBO) which has a strong negative uniaxial birefringence, $n_e < n_o$. Here, the phase matching conditions are met when the pump photon is extraordinarily (ordinarily) polarised and converts into two ordinarily (extraordinarily) polarised daughter photons.

Having the correct material is only the first step in achieving optimal conditions for down-conversion. To accomplish phase matching one must control the refractive indices for the individual fields either by angular or temperature tuning the nonlinear medium.

Angular tuning is the process of precisely controlling the alignment of the crystal optic axis with respect to the propagation direction of the pump field. Due to birefringence this will often result in an angular emission of the down-converted fields, and given the symmetry about the pump axis, the pair ω_s and ω_i is emitted as a cone out of the crystal. Figure 2.7 shows a typical experimental setup to couple down-converted light into optical fibers. Additionally, since some materials' refractive indices exhibit strong temperature dependences, for example lithium niobate, temperature can also be used to establish perfect phase matching.

Since the pump beam will inevitably contain a spectrum of wavelengths so will the down-converted photons and therefore they will share frequency correlations. Usually strong spectral filtering is applied to increase indistinguishability in this degree of freedom, although this has

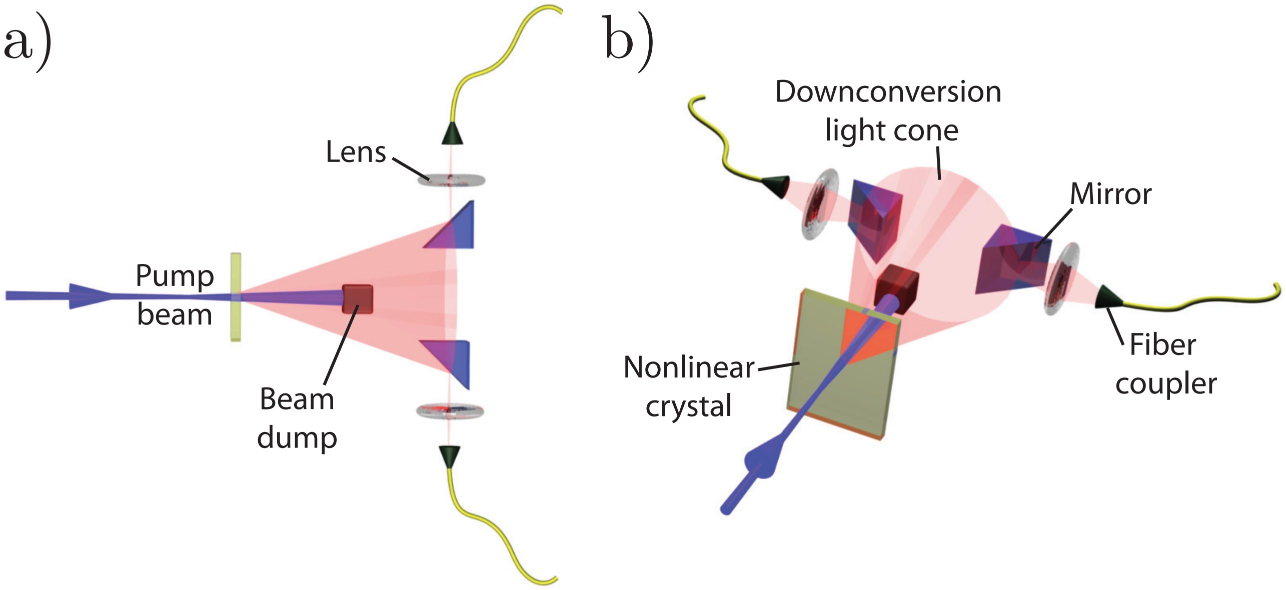

Figure 2.7: Experimental setup to couple light from a spontaneous parametric downconversion source into optical fibers. In most cases light is emitted out of the nonlinear crystal as a cone of light made up of degenerate single photon pairs at opposite sides of the cone. Prism mirrors direct light from the cone through lenses and into the fiber core. a) Top view. b) Oblique view.

the adverse effect introducing extra loss and decreasing overall photon collection efficiency. One way around this is to tailor the phase matching conditions appropriately such that the down-converted fields are spectrally separable, allowing the triggering of one photon in the pair without collapsing the other it into a spectrally mixed state. Such a system was developed and implemented in a Type-II bulk crystal source by Mosley *et al.* [48].

Group velocity mismatch in SPDC

In any birefringent material ordinary and extraordinary fields will experience different group-velocities if propagating neither exactly parallel nor perpendicular to the optic axis of the crystal [37]. For Type-I processes the signal and idler are identically polarised so they do not experience differing transverse walk-off. However, since the pump is orthogonally polarised to the signal/idler, it travels through the crystal with a different group-velocity compared to the down-converted light, introducing longitudinal walk-off. In the worst case two down-converted photons from *independent* sources, one produced at the beginning and one at the end of the crystal, will suffer a temporal delay that introduces distinguishability between the two down converted fields, see Fig. 2.8. Group-velocity mismatch, as it is known, is one source of distinguishability between photons from independent sources. In the context of this work it reduces the visibility of Hong-Ou-Mandel interference and therefore the quality of a quantum logic gate [37].

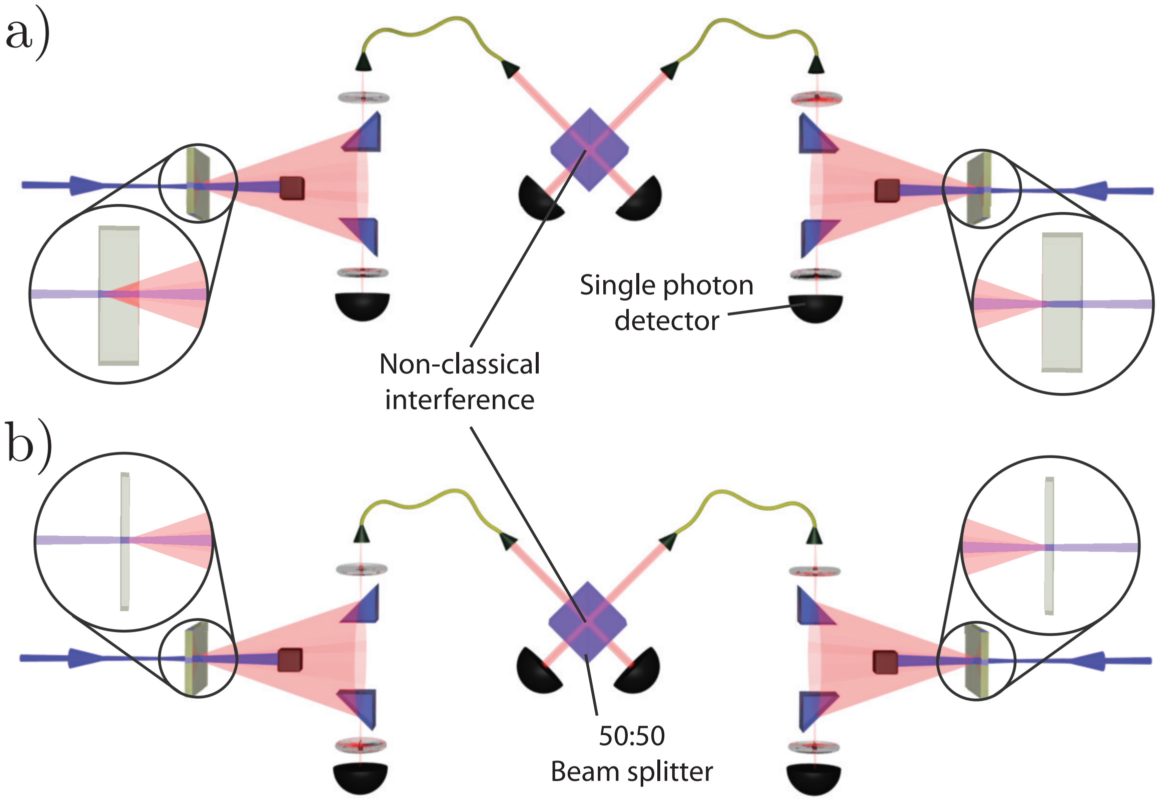

Figure 2.8: Group-velocity mismatch is one factor that effects the quality of non-classical interference between independent photons from separate downconversion sources. a) In the left-hand source, a pair of photons is produced at the beginning of the nonlinear crystal whereas in the right-hand source the pair is produced at the end of the nonlinear crystal. Because the pump and downconversion fields travel through the crystal with different group velocities a temporal mode mismatch is introduced between the interfering photons at the beam-splitter. As a result the visibility of Hong-Ou-Mandel interference is reduced, see Eq. 2.31 b) Using a shorter crystal reduces the effect of group velocity mismatch at the expense of source brightness.

Pulsed SPDC and higher order terms

Pulsed SPDC uses ultrashort (fs) pulses of light energy at high repetition rates (MHz) as the pump beam, ω_p, which offers two advantages over continuous wave SPDC:

1. Short pulses that are temporally separated provide a natural time bin for degenerate downconversion events[2].
2. High peak power increases the probability of simultaneous photon creation greater than two.

Although point 2 is desirable for multi-photon experiments from independent processes it also acts to introduce noise into the photon source. In the pulsed regime, used to perform experiments with photon numbers > 2, the likelihood of higher order photon events is increased due to the high peak power of each pulse. Without the ability to resolve the number of photons in a linear optics network[3], higher order photon events lead to spurious counting statistics. In the next chapter we describe a temporal multiplexing scheme that reduces the rate of higher order photon events without compromising the single-photon brightness.

---

[2] Provided the detectors are fast enough to resolve each pulse in one time window

[3] Standard single photon detectors simply click for an incident number of photons ≥ 1.

References

[1] Brennen, G. K., Deutsch, I. H. & Jessen, P. S. Entangling dipole-dipole interactions for quantum logic with neutral atoms. *Phys. Rev. A* **61**, 062309 (2000).

[2] Koppens, F. H. L. *et al.* Driven coherent oscillations of a single electron spin in a quantum dot. *Nature* **442**, 766–771 (2006).

[3] Chiorescu, I., Nakamura, Y., Harmans, C. J. P. M. & Mooij, J. E. Coherent quantum dynamics of a superconducting flux qubit. *Science* **299**, 1869–1871 (2003).

[4] Planck, M. On the law of distribution of energy in the normal spectrum. *Annalen der Physik* **4**, 553 (1901).

[5] Einstein, A. Concerning an heuristic point of view toward the emission and transformation of light. *Annalen der Physik (Translated into English by American Journal of Physics, 33, 1965)* **17**, 132 (1905).

[6] Jönsson, C. Elektroneninterferenzen an mehreren künstlich hergestellten Feinspalten. *Zeitschrift für Physik A Hadrons and Nuclei* **161**, 454–474 (1961).

[7] Arndt, M. *et al.* Wave-particle duality of C60 molecules. *Nature* **401**, 680–682 (1999).

[8] Juffmann, T. *et al.* Real-time single-molecule imaging of quantum interference. *Nature Nanotechnology* **7**, 297–300 (2012).

[9] Grangier, P., Roger, G. & Aspect, A. Experimental evidence for a photon anticorrelation effect on a beam splitter: A new light on single-photon interferences. *EPL (Europhysics Letters)* **1**, 173 (1986).

[10] Aspect, A., Grangier, P. & Roger, G. Experimental tests of realistic local theories via Bell's theorem. *Phys. Rev. Lett.* **47**, 460–463 (1981).

[11] Burnham, D. C. & Weinberg, D. L. Observation of simultaneity in parametric production of optical photon pairs. *Phys. Rev. Lett.* **25**, 84–87 (1970).

[12] Kwiat, P. G., Waks, E., White, A. G., Appelbaum, I. & Eberhard, P. H. Ultrabright source of polarization-entangled photons. *Phys. Rev. A* **60**, 773–776 (1999).

[13] Secure communication based on quantum cryptography. *http://www.secoqc.net/* (2012).

[14] Langford, N. *Encoding, manipulating and measuring quantum information in optics*. Ph.D. thesis, University of Queensland (2007).

[15] Nielsen, M. A. & Chuang, I. L. *Quantum Computation and Quantum Information* (Cambridge University Press, 2000).

[16] Kok, P. *et al.* Linear optical quantum computing with photonic qubits. *Rev. Mod. Phys.* **79**, 135–174 (2007).

[17] Walls, D. F. & Milburn, G. J. *Quantum Optics* (Springer-Verlag Berlin Heidelberg, 2008), 2nd edn.

[18] Hecht, E. *Optics* (Addison-Wesley, 1794), 2nd edn.

[19] Simon, R. & Mukunda, N. Minimal three-component su(2) gadget for polarization optics. *Physics Letters A* **143**, 165 – 169 (1990).

[20] Y. Yamamoto, M. K. & Igeta, K. Quantum mechanical aspects of optical communication and optical computing. *Proceedings of the 3rd Asia Pacific Physics Conference* 779–799 (1988).

[21] Milburn, G. J. Quantum optical fredkin gate. *Phys. Rev. Lett.* **62**, 2124–2127 (1989).

[22] Hutchinson, G. D. & Milburn, G. J. Nonlinear quantum optical computing via measurement. *Journal of Modern Optics* **51**, 1211–1222 (2004).

[23] Raussendorf, R. & Briegel, H. J. A one-way quantum computer. *Phys. Rev. Lett.* **86**, 5188–5191 (2001).

[24] Matsuda, N., Shimizu, R., Mitsumori, Y., Kosaka, H. & Edamatsu, K. Observation of optical-fibre kerr nonlinearity at the single-photon level. *Nature Photonics* **3**, 95–98 (2009).

[25] Knill, E., Laflamme, R. & Milburn, G. J. A scheme for efficient quantum computation with linear optics. *Nature* **409**, 46–52 (2001).

[26] O'Brien, J. L., Pryde, G. J., White, A. G., Ralph, T. C. & Branning, D. Demonstration of an all-optical quantum controlled-NOT gate. *Nature* **426**, 264–267 (2003).

[27] Langford, N. K. *et al.* Demonstration of a simple entangling optical gate and its use in Bell-state analysis. *Phys. Rev. Lett.* **95**, 210504 (2005).

[28] O'Brien, J. L. *et al.* Quantum process tomography of a controlled-NOT gate. *Phys. Rev. Lett.* **93**, 080502 (2004).

[29] Pittman, T. B., Fitch, M. J., Jacobs, B. C. & Franson, J. D. Experimental controlled-NOT logic gate for single photons in the coincidence basis. *Phys. Rev. A* **68**, 032316 (2003).

[30] Kiesel, N., Schmid, C., Weber, U., Ursin, R. & Weinfurter, H. Linear optics controlled-phase gate made simple. *Phys. Rev. Lett.* **95**, 210505 (2005).

[31] Okamoto, R., Hofmann, H. F., Takeuchi, S. & Sasaki, K. Demonstration of an optical quantum controlled-NOT gate without path interference. *Phys. Rev. Lett.* **95**, 210506 (2005).

[32] Lanyon, B. P. *et al.* Simplifying quantum logic using higher-dimensional Hilbert spaces. *Nature Physics* **5**, 134–140 (2009).

[33] Lanyon, B. P. *et al.* Experimental demonstration of a compiled version of Shor's algorithm with quantum entanglement. *Phys. Rev. Lett.* **99**, 250505 (2007).

[34] Lu, C.-Y., Browne, D. E., Yang, T. & Pan, J.-W. Demonstration of a compiled version of Shor's quantum factoring algorithm using photonic qubits. *Phys. Rev. Lett.* **99**, 250504 (2007).

[35] Politi, A., Cryan, M. J., Rarity, J. G., Yu, S. & O'Brien, J. L. Silica-on-silicon waveguide quantum circuits. *Science* 1155441 (2008).

[36] Hong, C. K., Ou, Z. Y. & Mandel, L. Measurement of subpicosecond time intervals between two photons by interference. *Phys. Rev. Lett.* **59**, 2044–2046 (1987).

[37] Jennewein, T., Ursin, R., Aspelmeyer, M. & Zeilinger, A. Performing high-quality multi-photon experiments with parametric down-conversion. *Journal of Physics B: Atomic, Molecular and Optical Physics* **42**, 114008 (2009).

[38] Ralph, T. C., Langford, N. K., Bell, T. B. & White, A. G. Linear optical controlled-NOT gate in the coincidence basis. *Phys. Rev. A* **65**, 062324 (2002).

[39] Hofmann, H. F. & Takeuchi, S. Quantum phase gate for photonic qubits using only beam splitters and postselection. *Phys. Rev. A* **66**, 024308 (2002).

[40] Barbieri, M. *et al.* Parametric downconversion and optical quantum gates: two's company, four's a crowd. *Journal of Modern Optics* **56**, 209–214 (2009).

[41] Tittel, W., Brendel, J., Zbinden, H. & Gisin, N. Violation of Bell inequalities by photons more than 10 km apart. *Phys. Rev. Lett.* **81**, 3563–3566 (1998).

[42] Gisin, N., Ribordy, G., Tittel, W. & Zbinden, H. Quantum cryptography. *Rev. Mod. Phys.* **74**, 145–195 (2002).

[43] Higgins, B. L. *et al.* Demonstrating Heisenberg-limited unambiguous phase estimation without adaptive measurements. *New Journal of Physics* **11** (2009).

[44] Boyd, R. W. *Nonlinear Optics* (Academic Press, London, 2008), 3rd edn.

[45] Franken, P. A., Hill, A. E., Peters, C. W. & Weinreich, G. Generation of optical harmonics. *Phys. Rev. Lett.* **7**, 118–119 (1961).

[46] White, A. *Classical and quantum dynamics of optical frequency conversion.* Ph.D. thesis, Australian National University (1997).

[47] Midwinter, J. E. & Warner, J. The effects of phase matching method and of uniaxial crystal symmetry on the polar distribution of second-order non-linear optical polarization. *British Journal of Applied Physics* **16**, 1135 (1965).

[48] Mosley, P. J. *et al.* Heralded generation of ultrafast single photons in pure quantum states. *Phys. Rev. Lett.* **100**, 133601 (2008).

CHAPTER 3

Reducing multi-photon rates in pulsed down-conversion by temporal multiplexing

Published: *Optics Express* **19**, 22698-22708 (2011)

M. A. Broome, M P. Almeida, A. Fedrizzi and A. G. White

Department of Physics, Centre for Quantum Computer Technology, University of Queensland,
Brisbane, Australia

Abstract

We present a simple technique to reduce the emission rate of higher-order photon events from pulsed spontaneous parametric down-conversion. The technique uses extra-cavity control over a mode locked ultrafast laser to simultaneously increase repetition rate and reduce the energy of each pulse from the pump beam. We apply our scheme to a photonic quantum gate, showing improvements in the non-classical interference visibility for 2-photon and 4-photon experiments, and in the quantum-gate fidelity and entangled state production in the 2-photon case.

3.1 Introduction

True single-photon sources are an essential requirement for scalable applications of quantum information processing. Ideally such sources should deterministically provide a Fourier limited wave-packet, having one and only one photon in a well defined spatio-temporal mode, and desirably with a high brightness [1]. Additionally, and in particular for the scalability of linear optics quantum computing [2], multiple devices should produce identical spectral emission to enable heralded and indistinguishable single-photons. Unfortunately, it is challenging to engineer single-photon emitters meeting all of these requirements. Solid state solutions, such as quantum dots [3, 4] despite demonstrating both triggered single-photon emission [5] and high collection efficiencies [6], have yet to achieve equivalent spectral properties across multiple sources. Systems based on color centers in diamond [7, 8], can suffer from low collection efficiencies due to isotropic emission and other candidates like atoms [9, 10] and molecules [11, 12] have similar issues with low output coupling and as of yet have not demonstrated high brightness.

One approach to produce single-photons is to employ pair sources, where conditional detection of one of a pair of photons is used to herald single-photon events. The current state-of-the art for heralded single-photon sources is spontaneous parametric down-conversion (SPDC) [13, 14, 15, 16]. Here a pump laser is used to create a pair of photons in a nonlinear birefringent material. However, creating single-photons in a pure state requires careful engineering of the properties of a down-conversion source. First, photon pairs from down-conversion are naturally entangled in energy and momentum, demanding special techniques to tailor their joint correlations and avoid heralding single-photons into mixed states [17, 18, 19, 20]. Second, since the process is spontaneous, there is a probability of emitting more than a single photon into the same spatio-temporal mode [21]. This effect is intensified when strong pump pulses are used to drive the down-conversion. These multi-photon, or higher-order, emissions have detrimental effects in applications such as quantum cryptography, where they can compromise the security of quantum key distribution [22]; and in linear optical quantum computing, where the noise resulting from these higher-order events significantly increases the error rates in quantum circuits [23, 24].

There are several techniques which can minimise multi-photon SPDC emissions. The simplest is to run an experiment at lower pump power, if one can afford the resulting decrease in source brightness. If this is not an option, several sources at lower power can be multiplexed. In the *spatial* multiplexing scheme suggested in [25], several down-converters are run in parallel as a photon switchyard. Whenever one source produces a trigger photon, the signal photon is switched into one common output mode. The efficiency for this scheme has been simulated in detail in [26] and demonstrated on a small scale in [27]. Alternatively, sources can be multiplexed in time.

In this letter, we implement a passive temporal multiplexing scheme. We show that increasing the repetition rate of the pump laser while simultaneously lowering the energy of each pump

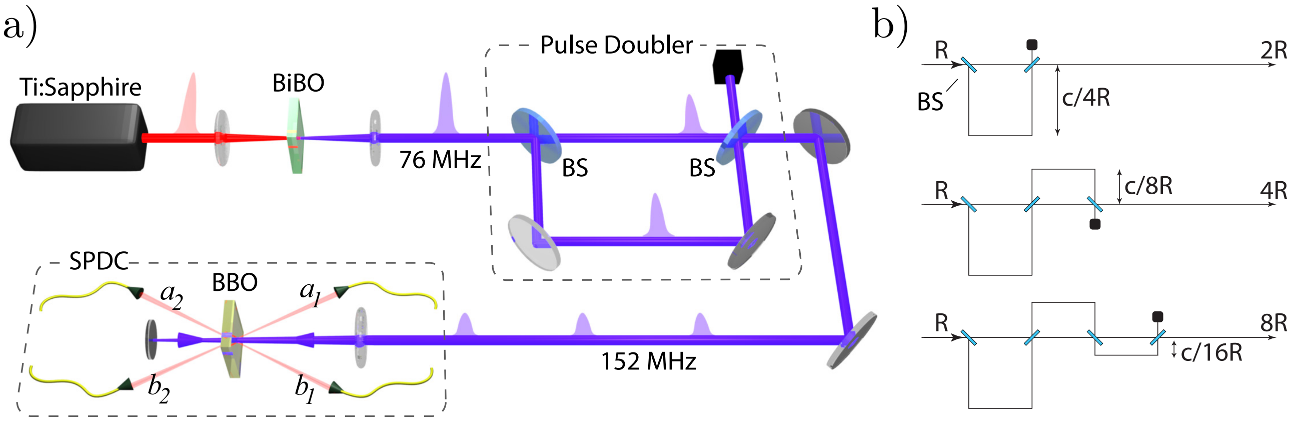

Figure 3.1: Experimental scheme. a) Doubling the pump laser repetition rate. A *Coherent MIRA 900 HP* mode-locked Ti:Sapphire laser outputs approximately 3.8 W of 820 nm pulses with a repetition rate of 76 MHz and a pulse length of approximately 100 fs. This light is frequency doubled via second harmonic generation in a non-linear bismuth borate (BiBO) crystal giving 1.53 W centred at 410 nm. An optical delay loop, consisting of two beamsplitters and two high-precision mirrors, splits off half of the laser light and feeds it back to the pump mode with a 6.6 ns delay which is equal to half the initial separation between two pulses (approximately 2 m). Photon pairs are created via spontaneous parametric downconversion in a type-I phase-matched β-barium-borate crystal (BBO), pumped bidirectionally. The photons are sent through interference filters centred at 820 nm with a full-width at half-maximum (FWHM) bandwidth of 2.5 nm before being coupled into single mode optical fibers. Photon were counted using standard avalanche photo-diodes. The output of each detector is fed into a commercially available counting logic with a coincident time window of 3 ns. The 152 MHz source was pumped with a maximum power of 1.53 W, with approximately 50% of this power available in the 76 MHz regime. The two photon coincidence brightness were 38.4 counts/s/mW and 40.3 counts/s/mW for the 152 MHz and 76 MHz sources respectively. b) The repetition rate is increased by introducing additional 50:50 beam splitters for delay loops, where each delay decreases in length by a half with respect to the previous one. This scheme can increases the repetition rate R beyond a factor of two with no further overall loss in pump power.

pulse decreases the emission of multi-photon events. Our technique allows an improvement of signal-to-noise ratio for heralded single-photon sources from pulsed down-conversion, without compromising the brightness of single-photon emission. Compared to previous multiplexing approaches, our scheme relies on a simple optical arrangement to perform extra-cavity control over the pump power and repetition rate. As a quality benchmark, we demonstrate the improvement in the non-classical interference visibility between photons emitted by a single or by independent down-conversion sources, as well as the overall quality of a photonic entangling quantum gate.

3.2 Pump repetition rate and higher-order terms

We start by showing the effects of increasing the pulse repetition rate of the pump on multi-photon emission in a single down-conversion source. The interaction of the pump beam with the nonlinear medium during each pulse is described by the Hamiltonian [28]

$$\mathrm{H} = i\xi\hbar\left(a_1^\dagger\ b_1^\dagger + \text{h.c.}\right), \tag{3.1}$$

where $a_1^\dagger$ and $b_1^\dagger$ are the photon creation operators into signal and idler modes a_1 and b_1 respectively; and ξ is the overall efficiency parameter, which represents the non-linear interaction strength and carries information about spectral properties of the pump laser. Furthermore, ξ is linearly proportional to the electric field amplitude of each pump pulse. The output state of the down-conversion process can be written as [29]

$$|\Psi_{SPDC}\rangle = \sqrt{1-|\lambda|^2}\sum_{n=0}^{\infty}\lambda^n\,|n,n\rangle_{a_1,b_1}, \tag{3.2}$$

with $\lambda{=}\xi\tau$, where τ is the interaction time inside the down-conversion medium. From Eq. 3.2 we see that the probability of creating n photon pairs per pulse is given by

$$P(n) = (1-|\lambda|^2)\,|\lambda|^{2n}. \tag{3.3}$$

Thus the joint photodetection rate per second for modes a_1 and b_1 using so-called bucket detectors, i.e. photodetectors without photon-number resolution is

$$C_{coinc} = R\sum_{n=1}^{\infty}(1-(1-\eta)^n)^2P(n), \tag{3.4}$$

where R is the repetition rate of the laser and η is the product of the detector efficiency and the optical efficiency to include optical losses and optical coupling [29]. As pump power per pulse is increased in an effort to increase single-photon brightness multi-photon terms increase more rapidly leading to lower signal-to-noise ratios. From Eqs. 3.3 and 3.4 the signal-to-noise ratio can be approximated by the single pair (n=1) emission over the double pair (n=2) emission,

$$SNR \approx \frac{\eta^2}{(1-(1-\eta)^2)^2\,|\lambda|^2}. \tag{3.5}$$

If we now halve the power of each pump pulse, such that $\xi \rightarrow \xi/\sqrt{2}$, while simultaneously doubling the repetition rate, $R \rightarrow 2R$, the joint photodetection rate becomes

$$C_{coinc} = 2R\sum_{n=1}^{\infty}\frac{(1-(1-\eta)^n)^2P(n)}{2^n}. \tag{3.6}$$

Note that the rate of generating just one pair of photons per second is not affected, while events

$n \geq 2$ are reduced by a factor of 2^{n-1}. In fact, an equivalent argument can be made for an arbitrary multiple increase in repetition rate, m, such that the generic formula for this scheme becomes,

$$C_{coinc}(m) = R \sum_{n=1}^{\infty} \frac{(1-(1-\eta)^n)^2 P(n)}{m^{(n-1)}}, \tag{3.7}$$

and the signal to noise ratio becomes

$$SNR \approx \frac{m\eta^2}{(1-(1-\eta)^2)^2 \left|\lambda\right|^2}. \tag{3.8}$$

Perhaps more importantly, the same is true for *independent* sources where two passes through the same down-conversion crystal (or equivalently two separate crystals) are used to produce independent photon pairs, see Fig. 3.1a. Since the mathematical argument is equivalent to above we omit it here and direct the interested reader to the appendix.

3.3 Experimental details

Since most commercial laser systems do not offer the feature of a tunable repetition rate, we developed a simple extra-cavity arrangement to do this, see Fig. 3.1. We used this scheme to double the repetition rate of the second harmonic light produced by frequency doubling the 820 nm line of a 76 MHz Ti:Sapphire laser (*Coherent Mira 900 HP*). Using two 50:50 beam splitters placed in series we introduce a delay of 6.6 ns, approximately half the time lapse between two original laser pulses, in one arm of the pulse doubler circuit while simultaneously lowering the peak pulse power. High precision mirror mounts are used to steer light into the down-conversion crystal to ensure the same phase matching conditions from both arms of the pulse doubling circuit. Note that the doubler has to be installed after the second-harmonic stage, because of the non-linear dependence of the second-harmonic process on pump power. Note furthermore, that the delay loop does not require active phase stabilisation, and that the temporal delay does not have to not be an exact multiple of the master laser, provided the pulses are separated by at least the timing jitter of the detectors.

Our scheme reduces the *total* available pump power by a factor of 2 due to the probabilistic recombination of the delayed and the original pump mode. This tradeoff is acceptable since multi-photon experiments relying on SPDC in bulk crystals already have to operate at reduced power to minimise noise. Modern SPDC sources based on periodically poled crystals only require a few hundred microwatt of pump power [30] and would benefit from even higher repetition rates. Figure 3.1b shows how our scheme can be extended to repetition rates of 4, 8 etc. without additional optical loss except that introduced by the beamsplitters.

To demonstrate the effectiveness of this scheme we measured the rate at which higher-order events from SPDC occur as a function of pump power. Figure 3.2 shows the ratio, $P(n{=}2)/P(n{=}1)$ between 4-photon and 2-photon events, as a function of the SPDC pump power for pumps at 76 MHz and 152 MHz. These results were obtained using spatially multiplexed

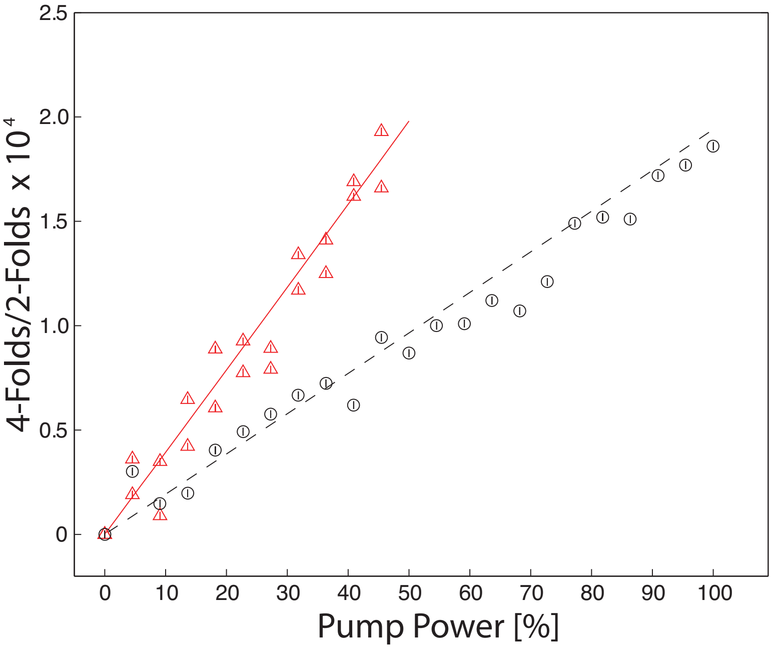

Figure 3.2: Ratio of 4-photon to 2-photon events for varying photon source pump power with pump repetition rates of 76 MHz (red triangles) and 152 MHz (black circles). The red solid and black dashed lines show the theoretical predictions. Since the pump beam at 76 MHz is only one arm of the pulse doubling circuit, the maximum power available is equal to 50% of the total power at 152 MHz. Errors due to Poissonian counting statistics are not visible on this scale.

single-photon avalanche diodes in order to count the number of photons in each down-conversion mode. The results show that in both pump regimes the ratio of 4-photon to 2-photon events varies linearly with pump pulse power as predicted by Eq. 3.6. However, there is a clear difference between the inclination of the two curves due to a decrease in the power available *per* pump pulse for the pump beam at 152 MHz compared to that at 76 MHz. The calculated slopes of both curves have a ratio of 2.12 ± 0.07, which is consistent with the fact that emission of single-photons per down-conversion mode is not altered in this scheme.

3.4 Application in linear optics quantum computing

It is interesting to test this scheme in the practical application of optical quantum information processing. As previously discussed in Refs. [23, 24] higher-order events from SPDC are the major factor in degrading the quality of entangled states produced by linear optical quantum gates: non-single photon inputs have a larger impact over the total error-per-gate operation than, for example, errors due to spatial-mode mismatch.

We built a photonic controlled-phase (CZ) gate to test the effectiveness of the pulse-doubling scheme, see Fig 3.3c. The circuit implementation is based on Hong-Ou-Mandel interference of the two optical input modes at a partially polarising beam-splitter (PPBS)—a detailed description of the gate can be found at [31], or Section 2.2.4 of this thesis. Ideally the PPBS will have

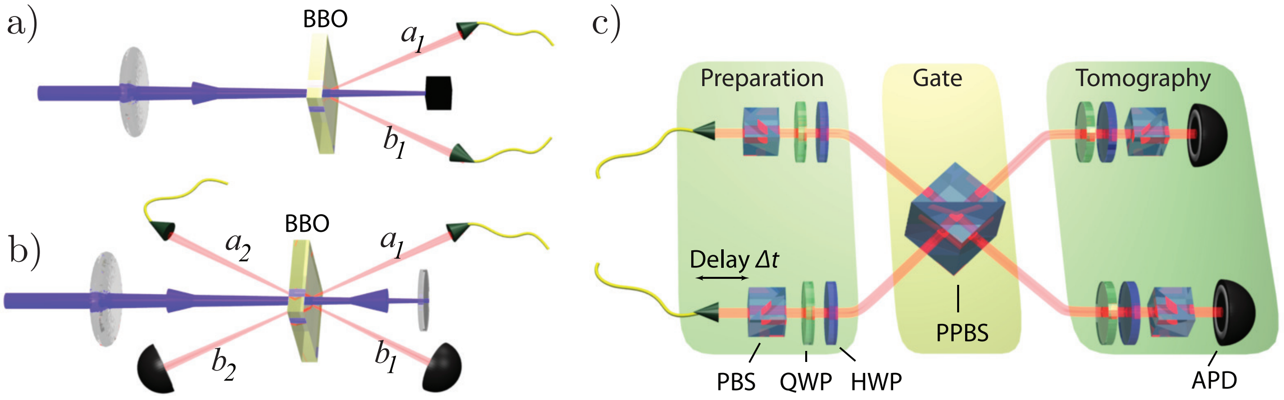

Figure 3.3: Schematic of the experimental setup. a) Input photons at modes a_1 and b_1 produced in a single down-conversion crystal; b) two independent photons are heralded at modes a_1 and a_2 by coincident detection of photons b_1 and b_2. c) A controlled-phase gate implemented by Hong-Ou-Mandel interference of the input modes at a partial polarised beam splitter (PPBS) using two different photon sources. Input photons are launched from single-mode optical fibres into the quantum gate, where one input arm is used to control the temporal delay, Δt, between the two interfering optical modes. The state preparation and tomography is implemented using quarter- (QWP) and half-wave plates (HWP) and polarising beam-splitters (PBS). The two input optical modes are superposed at a single partially polarizing beam splitter (PPBS) with nominal reflectivities of η_H=0 for horizontally, and η_V=2/3 for vertically polarized light respectively. Photons are detected using standard avalanche photo-diodes (APD).

reflectivities of η_H=0 and η_V=2/3 for horizontally and vertically polarised light respectively. Each input photon encodes a polarization qubit in the horizontal and vertical ($|H\rangle$,$|V\rangle$) basis. Successful operation of the gate is post-selected by the detection of at least one photon in each output mode, which occurs non-deterministically with a probability of 1/9. Conditioned on post-selection the gate acts to induce a non-linear phase shift when both input states are vertically polarized i.e. $|VV\rangle \rightarrow -|VV\rangle$. Furthermore, the gate is entangling and produces the maximally entangled state $|HD\rangle + |VA\rangle$ for an input $|DD\rangle$.

We used three measurements to assess the effectiveness of our scheme in a photonic quantum gate: i) the quality non-classical interference, ii) the fidelity of bipartite quantum states and iii) an entanglement measure between two qubits.

When two indistinguishable photons are superposed at a beam splitter they will bunch, that is, preferably exit the beamsplitter via the same optical output mode. Experimentally, as the relative path difference between input photons, Δt, is reduced (and hence their temporal indistinguishability is reduced) the bunching effect is seen as a drop in coincident photon detection at the two output modes. This is known as Hong-Ou-Mandel (HOM) [32] interference and its quality is measured by the visibility, V=$(C_{dist} - C_{indist})/C_{dist}$, where C_{dist} and C_{indist} are the coincidence counts at the output of the beam splitter for distinguishable and indistinguishable photon inputs respectively. Non-single photon inputs increase the likelihood of photons being detected in both output modes leading to spurious coincidence events. Therefore the quality of HOM interference degrades as the ratio of multi-photon events to single-photon events from

SPDC increases, see Eq. 3.5. In particular, the visibility of HOM interference is a direct measure of photon-number purity once spatio-temporal mode mismatch is accounted for [33], it therefore serves as a benchmark for the quality of any linear optics quantum gate.

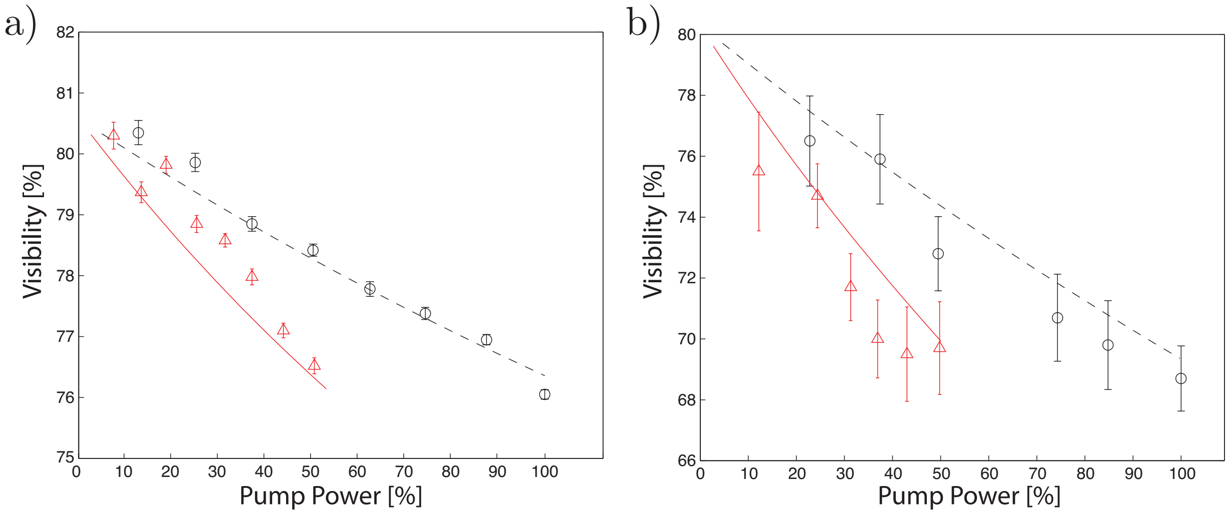

Figure 3.4: Experimental data for Hong-Ou-Mandel visibilities, for varying photon source pump power, in a photonic controlled-phase gate. The two photon input state $|VV\rangle$ is interfered at a PPBS by reducing the relative path difference between the input photons. a) Interference visibilities for dependent photon inputs and b) visibilities for independent photon inputs for varying pump powers. Red triangles show results using a pump laser with a repetition rate of 76 MHz and black circles with a repetition rate of 152 MHz. The red solid and black dashed lines show the theoretical predictions and the errors are calculated using Poissonian counting statistics.

In the case of a controlled-phase gate a visibility of 80% would be observed for a perfect single-photon source and an ideal PPBS with reflectivity η_V=2/3. Fig. 3.4 shows how our doubling scheme reduces the detrimental effect on the visibility of non-classical interference while increasing the pump power. We show this effect for two scenarios: i) for input photons produced by a single down-conversion crystal shown in Fig. 3.3a and ii) photons produced by two down-conversion sources (independent photon inputs) shown in Fig. 3.3b. In the latter scenario the signal photon from each pass of the crystal is heralded with the detection of the corresponding idler photon. The experimental data is compared to a numeric model created with the Matlab *quantum optics toolbox* by Sze M. Tan [34] and associated linear optical quantum computing tools written by T. Jennewein, see [26]. This model generates photon number states for a source derived from the Hamiltonian in Eq. 3.1. It propagates the SPDC state through a series of optical components as described in [26] and detects them with counting devices that act like bucket detectors, i.e. they click for photon events $n \geq 1$. The theoretical plots in all figures were based on this Matlab model, assuming imperfect non-number resolving detectors with a nominal efficiency of 60% and a measured PPBS reflectivity of η_v=0.682±0.002.

Lastly we examine the effects of our pulse doubling scheme on the quality of entangled states generated by a quantum gate. Although the data presented here was taken with the dependent photon source an equivalent result would be found for the independent case. We characterized the entangled state generated by the CZ gate using quantum state tomography for dependent photon inputs produced by a single down-conversion crystal [35]. We prepare the initial input state, $|DD\rangle$ and make projective measurements on each output photon with the over complete set $\{|H\rangle, |V\rangle, |D\rangle, |A\rangle, |R\rangle, |L\rangle\}$, where $|D\rangle = (|H\rangle + |V\rangle)/\sqrt{2}$, $|A\rangle = (|H\rangle - |V\rangle)/\sqrt{2}$, $|R\rangle = (|H\rangle + i|V\rangle/\sqrt{2}$, and $|L\rangle = (|H\rangle - i|V\rangle/\sqrt{2}$ giving a total of 36 measurements. The input state $|DD\rangle$ gives the maximally entangled output state $|HD\rangle + |VA\rangle$ and, as such, is most affected by higher-order photon emissions as shown in [23, 24]. The measured density matrix, ρ, is reconstructed using a maximum likelihood algorithm and compared to the ideal state, ρ_{ideal}. We chose the measures of state fidelity, given by,

$$F \equiv \mathrm{Tr}^2(\sqrt{\rho^{1/2}\rho_{ideal}\rho^{1/2}}), \tag{3.9}$$

and tangle (concurrence squared) as a test for entangled state quality. Figure. 4.3a shows the results. We observe a stark reduction in the rate of state degradation, whilst increasing source pump power, as we switch from a 76 MHz to 152 MHz pump repetition rate. The results show the effect for a dependent downconversion source where the goal is to reduce the number of $n \geq 2$ events per down-conversion mode.

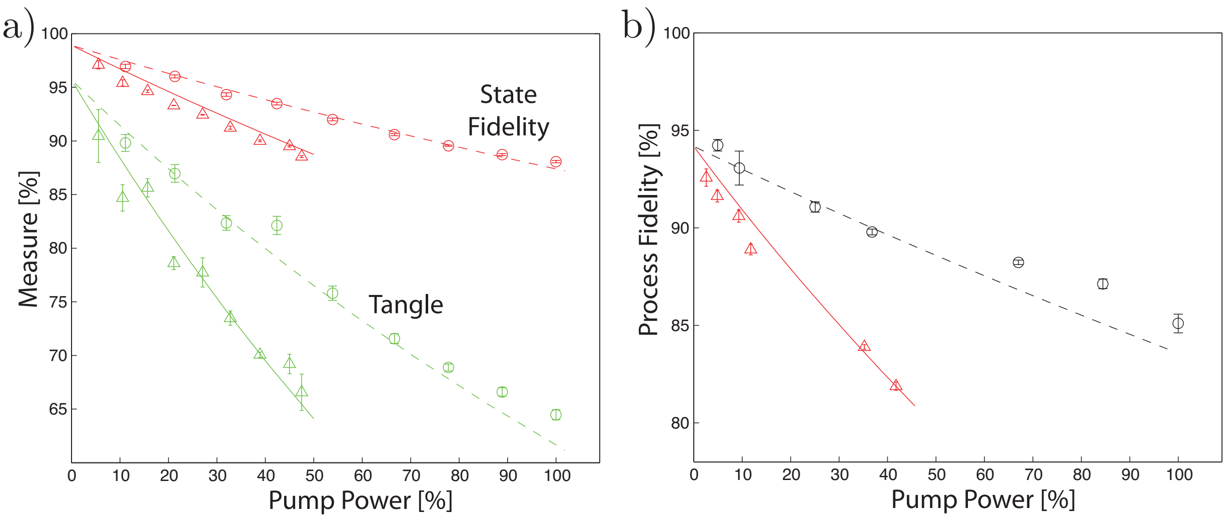

Figure 3.5: Photonic CZ gate performance for varying source pump powers and repetition rates. a) Photons from a dependent SPDC source are prepared in the initial state $|DD\rangle$. The state quality degrades as source pump power, and hence the relative number of higher-order terms, increases. This effect is suppressed by doubling the repetition rate of the source pump laser. Data was obtained with a pump laser at 76 MHz (triangles) and 152 MHz (circles). The dashed and solid lines show theoretical predictions. b) Similarly the process of the entangling operation performed by the gate degrades with source pump power. Red triangles show results using a pump laser with a repetition rate of 76 MHz and black circles with a repetition rate of 152 MHz, the red solid and black dashed lines show the theoretical predictions. Errors are calculated using Poissonian counting statistics.

We also characterised the overall gate performance via quantum *process* tomography as detailed in Ref. [35]. The process fidelity is calculated by comparing the resulting process matrix obtained from experiment, X, to that of an ideal process for a CZ gate, X_{ideal}. Figure 4.3b shows the effect of increasing laser power on process fidelity, defined equivalently to Eq. 3.9.

Finally, we simulated Hong-Ou-Mandel interference inside a controlled-phase gate between photons from two independent sources. Figure 3.6a shows the effect on non-classical interference visibility as a function of both photodetection efficiency and repetition rate of the pump laser. Notably, we see that increasing the repetition rate by a factor of 10 dramatically increases the interference quality. We also show separately the variation of the non-classical interference visibility as function of detection efficiency, shown in Fig. 3.6b, and pump repetition rate, shown in Fig. 3.6c. While the interference visibility can also be increased by employing highly efficient photodetectors, this technique is less effective and doing so is considered technologically more difficult.

We note that the maximum possible repetition rate used to drive a SPDC source is limited to $R = 1/\Delta t$, where Δt is the coincidence time window which, in turn, is dominated by the combined electronic jitter of single photodetectors and the coincidence counting logic. Commercial silicon avalanche photon diodes exhibit a timing jitter of typically 400 ps, which can be matched by commercial counting electronics based on field-programmable gate arrays (FPGA). An experiment using these detectors can thus in principle resolve between two down-conversion events created by laser pulses at a maximum repetition rate of 1 GHz, which can be reached with the extra-cavity control detailed in this paper. This is well worth considering for SPDC experiments relying on the widely used 76 MHz laser we used for our work. However, it should be pointed out that femtosecond Ti:sapphire lasers with 500 MHz and even 1 GHz repetition rate are now commercially available [36] and are probably a more reasonable approach for a newly designed experiment which does not require abundant pump power.

3.5 Discussion

In conclusion, we have demonstrated a simple temporal multiplexing scheme that reduces the number of higher-order photon events from heralded single-photon sources based on SPDC. Our technique improves the signal-to-noise ratio as a result of reducing multi-photon events, without compromising the brightness and quality of the desired single-photon states. We also demonstrated an improvement in the performance of a linear photonic quantum gate using our source. Our technique could be integrated with spatially multiplexed down-conversion schemes where multiple crystals and optical switches are used to herald single photons into purer Fock-states [27]. In such a scheme one could reduce the number of spatially multiplexed down-conversion crystals to achieve a desired signal-to-noise ratio. Future improvements in single-photon technologies such as linear optics quantum computing and quantum communications will require a combination of improvements in sources and detection, in particular efficient number resolving photon detection. In practice, although number resolving detectors reduce

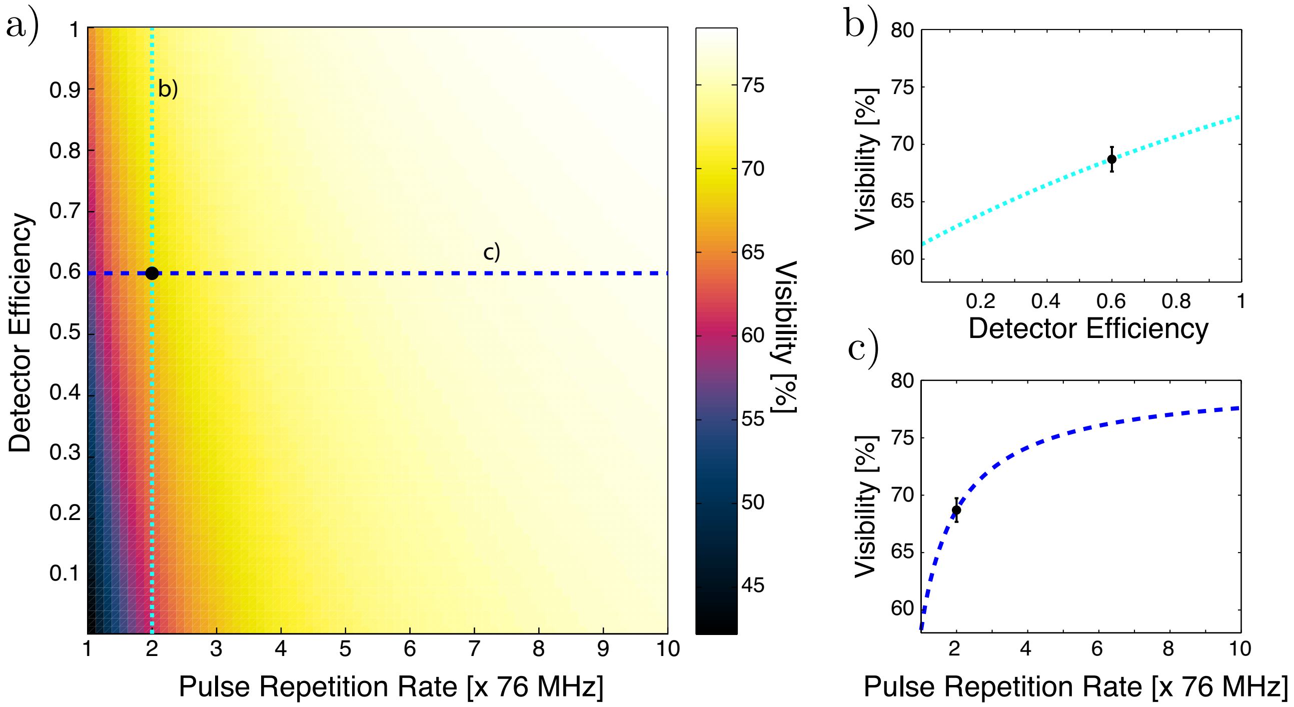

Figure 3.6: a) Theoretical simulation of non-classical interference visibility in a controlled-phase gate from two independent photon sources. The visibility of interference is shown by the color scale and depends on both the detector efficiency and repetition rate of the laser. The simulation assumes an input state of $|VV\rangle$ from independent photon sources pumped with 100 % of the available pump power and detected with non-number resolving photodetectors. The free parameter in this plot is the optical loss which, fitted to the experimental data, is 40%. b) and c) show cross-sections of the simulated data, shown in a), for varying detector efficiency and varying pulse repetition rate respectively. The black marker in these plots shows the experimental data point taken from Fig.3.4b

the chance of spurious counting statistics, because of optical loss, they do not remove the need to suppress the number of higher-order terms from SPDC.

3.6 Appendix

The Hamiltonian that describes the creation of photons for both forward and backward emission from a type-I down-conversion source, see Fig. 3.1a, can be written as [28],

$$\mathrm{H} = i\xi_1\hbar a_1^\dagger\, b_1^\dagger \;+\; i\xi_2\hbar a_2^\dagger\, b_2^\dagger \;+\; \text{h.c.}, \tag{3.10}$$

where the ξ_1 and ξ_2 represent the overall efficiencies and non-linear interaction strengths for the forward and backward emissions, respectively, they are also linearly proportional to the electric field amplitude of each pulse; $a_j^\dagger$, $b_j^\dagger$, with $j = \{1, 2\}$ are the creation operators of the forward and backward down-conversion modes. From the above equation we obtain the following state,

$$|\Psi_{SPDC}\rangle = \sqrt{(1-|\lambda_1|^2)(1-|\lambda_2|^2)}\sum_{n_1=0}^{\infty}\lambda_1^{n_1}\,|n_1, n_1\rangle_{a_1,b_1}\sum_{n_2=0}^{\infty}\lambda_2^{n_2}\,|n_2, n_2\rangle_{a_2,b_2}, \tag{3.11}$$

with $\lambda_1 = \xi_1\tau$ and $\lambda_2 = \xi_2\tau$. Therefore, the probability of creating n_1 and n_2 photons from crystal passes 1 and 2 per pulse is given by

$$P(n_1, n_2) = (1-|\lambda_1|^2)(1-|\lambda_2|^2)\left|\lambda_1^{2n_1}\right|\left|\lambda_2^{2n_2}\right|. \tag{3.12}$$

For independent sources the presence of photons in modes a_1 and a_2 are heralded upon a detection event in modes b_1 and b_2 respectively. Again, using non-number resolving detectors with detection efficiency η, the rate per second of jointly heralding photons in modes a_1 and a_2 is given by

$$C_{coinc} = R\sum_{n_1=1}^{\infty}\sum_{n_2=1}^{\infty}(1-(1-\eta)^{n_1})^2(1-(1-\eta)^{n_2})^2 P(n_1, n_2). \tag{3.13}$$

Similarly to the previous argument for dependent photons, halving the power per pulse while simultaneously doubling the repetition rate gives

$$C_{coinc} = 2R\sum_{n_1=1}^{\infty}\sum_{n_2=1}^{\infty}\frac{(1-(1-\eta)^{n_1})^2(1-(1-\eta)^{n_2})^2}{2^{n_1+n_2}}P(n_1, n_2). \tag{3.14}$$

References

[1] Lounis, B. & Orrit, M. Single-photon sources. *Reports on Progress in Physics* **68**, 1129 (2005).

[2] Knill, E., Laflamme, R. & Milburn, G. J. A scheme for efficient quantum computation with linear optics. *Nature* **409**, 46–52 (2001).

[3] Michler, P. *et al.* Quantum correlation among photons from a single quantum dot at room temperature. *Nature* **406**, 968–970 (2000).

[4] Santori, C., Fattal, D., Vuckovic, J., Solomon, G. S. & Yamamoto, Y. Indistinguishable photons from a single-photon device. *Nature* **419**, 594–597 (2002).

[5] Rivoire, K. *et al.* Fast quantum dot single photon source triggered at telecommunications wavelength. *Applied Physics Letters* **98**, 3 (2011).

[6] Claudon, J. *et al.* A highly efficient single-photon source based on a quantum dot in a photonic nanowire. *Nature Photonics* **4**, 174–177 (2010).

[7] Beveratos, A. *et al.* Room temperature stable single-photon source. *Eur. Phys. J. D* **18**, 191–196 (2002).

[8] Kurtsiefer, C., Mayer, S., Zarda, P. & Weinfurter, H. Stable solid-state source of single photons. *Phys. Rev. Lett.* **85**, 290–293 (2000).

[9] McKeever, J. *et al.* Deterministic generation of single photons from one atom trapped in a cavity. *Science* **303**, 1992–1994 (2004).

[10] Chou, C. W., Polyakov, S. V., Kuzmich, A. & Kimble, H. J. Single-photon generation from stored excitation in an atomic ensemble. *Phys. Rev. Lett.* **92**, 213601 (2004).

[11] Lounis, B. & Moerner, W. E. Single photons on demand from a single molecule at room temperature. *Nature* **407**, 491–493 (2000).

[12] Lettow, R. *et al.* Quantum interference of tunably indistinguishable photons from remote organic molecules. *Phys. Rev. Lett.* **104**, 123605 (2010).

[13] Lvovsky, A. I. *et al.* Quantum state reconstruction of the single-photon fock state. *Phys. Rev. Lett.* **87**, 050402 (2001).

[14] Pittman, T. B., Jacobs, B. C. & Franson, J. D. Heralding single photons from pulsed parametric down-conversion. *Optics Communications* **246**, 545–550 (2005).

[15] U'Ren, A. B., Silberhorn, C., Banaszek, K. & Walmsley, I. A. Efficient conditional preparation of high-fidelity single photon states for fiber-optic quantum networks. *Phys. Rev. Lett.* **93**, 093601 (2004).

[16] U'Ren, A. B., Jeronimo-Moreno, Y. & Garcia-Gracia, H. Generation of fourier-transform-limited heralded single photons. *Phys. Rev. A* **75**, 023810 (2007).

[17] Grice, W. P., U'Ren, A. B. & Walmsley, I. A. Eliminating frequency and space-time correlations in multiphoton states. *Phys. Rev. A* **64**, 063815 (2001).

[18] U'Ren, A. B., Erdmann, R. K., de la Cruz-Gutierrez, M. & Walmsley, I. A. Generation of two-photon states with an arbitrary degree of entanglement via nonlinear crystal superlattices. *Phys. Rev. Lett.* **97**, 223602 (2006).

[19] Neergaard-Nielsen, J. S., Nielsen, B. M., Takahashi, H., Vistnes, A. I. & Polzik, E. S. High purity bright single photon source. *Opt. Express* **15**, 7940–7949 (2007).

[20] Brańczyk, A., Fedrizzi, A., Stace, T., Ralph, T. & White, A. Engineered optical nonlinearity for quantum light sources. *Optics Express* **19**, 55–65 (2011).

[21] Weinfurter, H. & Żukowski, M. Four-photon entanglement from down-conversion. *Phys. Rev. A* **64**, 010102 (2001).

[22] Brassard, G., Lütkenhaus, N., Mor, T. & Sanders, B. C. Limitations on practical quantum cryptography. *Phys. Rev. Lett.* **85**, 1330–1333 (2000).

[23] Weinhold, T. J. *et al.* Understanding photonic quantum-logic gates: The road to fault tolerance. *arXiv:0808.0794v1* (2008).

[24] Barbieri, M. *et al.* Parametric downconversion and optical quantum gates: two's company, four's a crowd. *Journal of Modern Optics* **56**, 209–214 (2009).

[25] Migdall, A. L., Branning, D. & Castelletto, S. Tailoring single-photon and multiphoton probabilities of a single-photon on-demand source. *Phys. Rev. A* **66**, 053805 (2002).

[26] Jennewein, T., Barbieri, M. & White, A. G. Single-photon device requirements for operating linear optics quantum computing outside the post-selection basis. *Journal of Modern Optics* **58**, 276–287 (2011).

[27] Ma, X.-s., Zotter, S., Kofler, J., Jennewein, T. & Zeilinger, A. Experimental generation of single photons via active multiplexing. *Phys. Rev. A* **83**, 043814 (2011).

[28] Ou, Z.-Y. J. *Multi-Photon Quantum Interference* (Springer, 2010), 1st edn.

[29] Kok, P. *et al.* Linear optical quantum computing with photonic qubits. *Rev. Mod. Phys.* **79**, 135–174 (2007).

[30] Evans, P. G., Bennink, R. S., Grice, W. P., Humble, T. S. & Schaake, J. Bright source of spectrally uncorrelated polarization-entangled photons with nearly single-mode emission. *Phys. Rev. Lett.* **105**, 253601 (2010).

[31] Langford, N. K. *et al.* Demonstration of a simple entangling optical gate and its use in Bell-state analysis. *Phys. Rev. Lett.* **95**, 210504 (2005).

[32] Hong, C. K., Ou, Z. Y. & Mandel, L. Measurement of subpicosecond time intervals between two photons by interference. *Phys. Rev. Lett.* **59**, 2044–2046 (1987).

[33] Brańczyk, A., Ralph, T., Helwig, W. & Silberhorn, C. Optimized generation of heralded fock states using parametric down-conversion. *New Journal of Physics* **12**, 063001 (2010).

[34] Tan, S. M. A computational toolbox for quantum and atomic optics. *Opt. B: Quantum and Semiclassical Optics* **1** (1999).

[35] O'Brien, J. L. *et al.* Quantum process tomography of a controlled-NOT gate. *Phys. Rev. Lett.* **93**, 080502 (2004).

[36] Gigaoptics website (http://www.gigaoptics.com/, last checked in August 2011).

CHAPTER 4

Hardy’s paradox and violation of a state-independent Bell inequality in time

Published: *Physical Review Letters* **106**, 200402 (2011)

A. Fedrizzi[1], Marcelo P. Almeida[1], M. A. Broome[1], A. G. White[1]
and Marco Barbieri[2]

[1]Centre for Engineered Quantum Systems and Centre for Quantum Computer and Communication Technology, School of Mathematics and Physics, University of Queensland, 4072 Brisbane, QLD, Australia
[2]Groupe d’Optique Quantique, Laboratoire Charles Fabry, Institut d’Optique, CNRS, Université Paris-Sud XI, Campus Polytechnique, RD 128, 91127 Palaiseau cedex, France

Abstract

Measurement probabilities and correlations between distant particles in quantum mechanics cannot be reproduced by means of local realistic theories. This result is established by tests such as Bell’s inequality and Hardy’s paradox. Here we experimentally demonstrate these concepts in the time domain. We measured a much stronger form of Hardy’s paradox and demonstrate violation of a Bell inequality in time, independent of the quantum state, including for fully mixed states.

4.1 Introduction

Quantum mechanics depicts a world with fuzzier contours than our intuitive mind would suggest. In our common experience, we would naively picture a measurement as a way of revealing some objective property of an object. This view is disproved by several counterexamples, of which the most common is provided by an entangled system: the correlations between measurement outcomes can not be explained by a theory assuming that each subsystem has values determined independently from of measurement itself. Well-proven tests such as Hardy's paradox [1] and Bell's inequality [2, 3] capture these features of spatial entanglement.

This inconsistency can be expressed in a different setting; as pointed out by Legget and Garg in their seminal paper [4], one can consider correlations between measurements on the *same object* occurring at *different times*. Their aim was to find a particular instance where a realistic view was untenable, which has subsequently been the subject of numerous theoretical [5, 6, 7, 8] investigations and experimental demonstrations [9, 10, 11]. In a more general context, temporal quantum phenomena, in particular "entanglement in time", have subsequently been studied in [12, 13, 14].

Here, we report the first experimental implementation of temporal quantum phenomena beyond the Leggett-Garg inequality: that Hardy's paradox is much stronger in time [14], and that a temporal Bell inequality can be state-independent—it can be violated by all quantum states, even fully mixed ones [12]. Our experiment highlights surprising aspects of quantum foundations—such as all quantum states are entangled in time. For quantum technology, entanglement in time constitutes a, so far, virtually untapped new resource—it might lead to more efficient protocols in quantum information, communication and control [12].

Consider a quantum system located at two points in spacetime, A and B, where a quantum particle exists at each point. A classical model of such a system is based on two assumptions: (i) realism, that the particle at each point has definite properties prior to, and independent of measurements; and (ii) non-disturbance, that results of measurements at A are not influenced by measurements at B, and vice-versa. In the spatial case, Fig. 4.1a, there are separate particles at A and B, and special relativity ensures that disturbances cannot propagate between them faster than the speed of light. Thus tenet (ii)—now termed *locality*—can be enforced by a space-like separation. In the temporal case, Fig. 4.1b, there is a single particle at different times, t_A and t_B, and no known physical principle exists to enforce locality. However, it can be substituted by the ad hoc hypothesis of *measurement non-invasiveness*, i.e. that any (classical) measurement can be performed such that it does not influence the outcome of a subsequent measurement on the same system at a later (or earlier) time.

It might seem logically inconsistent to assume non-invasiveness and then compare it with an invasive theory such as quantum mechanics. It has been observed however, that non-invasiveness is in some sense equivalent to demanding perfect repeatability of a quantum measurement. This requirement is compatible with quantum mechanics and allows the construction of hidden variable models, which are identical to the ones originating from the assumption of

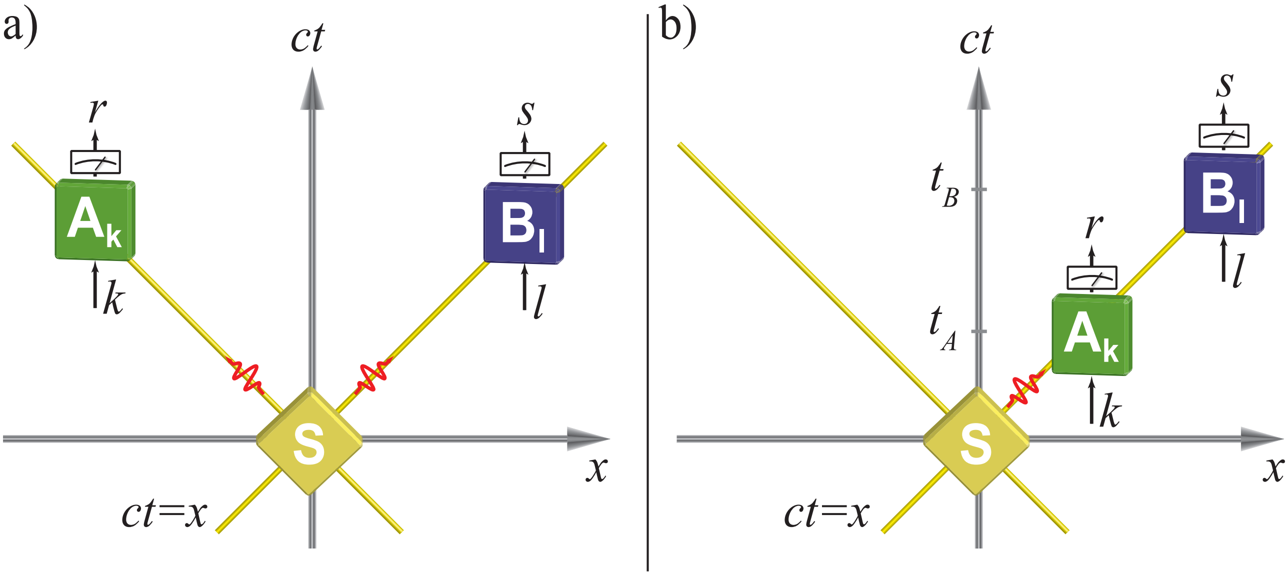

Figure 4.1: Thought experiment for the violation of local realistic theories. a) Spatial scenario: A source S emits two (entangled) qubits, which are sent to two remote observers A and B. Each subsystem is subject to two measurements A_k and B_l, where k and l denote the measurement settings at different sites. The outcomes of individual measurements are labelled r and s. b) Thought experiment for the violation of non-invasive, realistic theories. A single system is subjected to two measurements A_k and B_l , in this case occurring at different times $t_B > t_A$.

non-invasiveness [13, 14].

4.2 Hardy's paradox in time

Despite the fact that two-body correlations in space and time are mathematically equivalent [12], there are remarkable differences between measurements on quantum systems in the two domains. The first can be found in the temporal version [14] of Hardy's paradox [1, 15, 16, 17, 18, 19, 20]. It describes a paradoxical situation in which quantum mechanics allows a set of probabilities which are logically inconsistent within a classical framework. Consider two observers, Alice and Bob, sharing a single system on which they conduct a joint measurement with the choices A_k and B_l, with $k, l = \{0, 1\}$, at two different times, Fig. 4.1b. The measurements are dichotomic, with the possible outcomes $r, s = \{0, 1\}$, and the probability of a result r for Alice and s for Bob is $P(r, s|l, k)$. For a classical system, which obeys realism and non-invasiveness, r and s are defined before the measurement, and the choice $k(l)$ cannot possibly affect the value of $s(r)$. We also stress that in this view measurement outcomes exist as objective properties, either when the measurement actually took place or not.

Now consider the following set of outcome probabilities for different choices of measurements on this system:

$$P(1,1|1,1) > 0 \tag{4.1}$$
$$P(1,0|1,0) = 0 \tag{4.2}$$
$$P(0,1|0,1) = 0$$
$$P(1,1|0,0) = 0. \tag{4.3}$$

Due to Eq. 4.1, Alice and Bob will occasionally obtain the outcome r=1 and s=1 for a joint measurement A_1, B_1. By virtue of probabilities (4.2) they cannot observe the outcome r=0, s=0 for the alternative measurement choice A_0, B_0. In order to explain (4.1), their system must now however allow simultaneous outcomes r=1, s=1 for A_0, B_0. This, however, contradicts requirement (4.3) [1, 14].

Quantum mechanics, of course, resolves the paradox [14]. Consider a single two-level quantum system (qubit) prepared in the state $|\mathbf{0}\rangle$. With the Pauli measurements A_0=B_1=$-Z$, and A_1=B_0=X, where Z and X are the Pauli operators corresponding to the measurement along the z and, respectively, x directions on the Bloch sphere, it satisfies the equalities (4.1)-(4.3), with $P(1,1|1,1)$=0.25, see section 4.5.

In principle, a single observation of a detection event for the settings $k,l = 1$ (4.1) would—in the absence of detections for settings (4.2)—provide a compelling proof that nature does not obey the classical worldview established by the assumptions of realism and non-invasiveness (or perfect repeatability [13, 14]). However, even in an ideal scenario, zero probabilities can only ever be established to within an error governed by the number of measurement runs. In practice, we have to deal with imperfect states, measurements and detectors, which exacerbates this problem. We can instead, following Mermin [24], place a bound on $P(1,1|1,1)$, given the measured values of the other probabilities:

$$\begin{aligned}\mathcal{H} =& P(1,1|1,1) - P(1,1|0,0) \\ &-P(1,0|1,0) - P(0,1|0,1) \leq 0.\end{aligned} \tag{4.4}$$

We test this inequality in a two-photon experiment, see Fig. 4.3a. A system qubit is encoded in the polarisation of a single photon; horizontal (H) and vertical (V) polarisations determine the z-axis of the Bloch sphere. We implement the first, necessarily non-destructive, measurement using a non-deterministic, photonic controlled-phase (CZ) gate, Fig. 4.2b. It acts on two polarisation qubits, the signal $|\psi\rangle_s$, and the meter $|\phi\rangle_m$. The state of the signal qubit controls the meter, acting as the target qubit. An input state $|V\rangle_s |D\rangle_m$, for example, undergoes the controlled rotation $|V\rangle_s |D\rangle_m \rightarrow |V\rangle_s |A\rangle_m$ while $|H\rangle_s |D\rangle_m \rightarrow |H\rangle_s |D\rangle_m$. The polarisation of the signal can then be inferred by its action on the meter [9, 25, 26]. If the arbitrary state $|\psi\rangle_s |D\rangle_m$ is injected, we can measure Z on the signal just by observing whether the meter has been rotated or not. Arbitrary directions can be chosen for the measurement by inserting a proper rotation on the signal before the gate, as one would do with a regular polariser. This

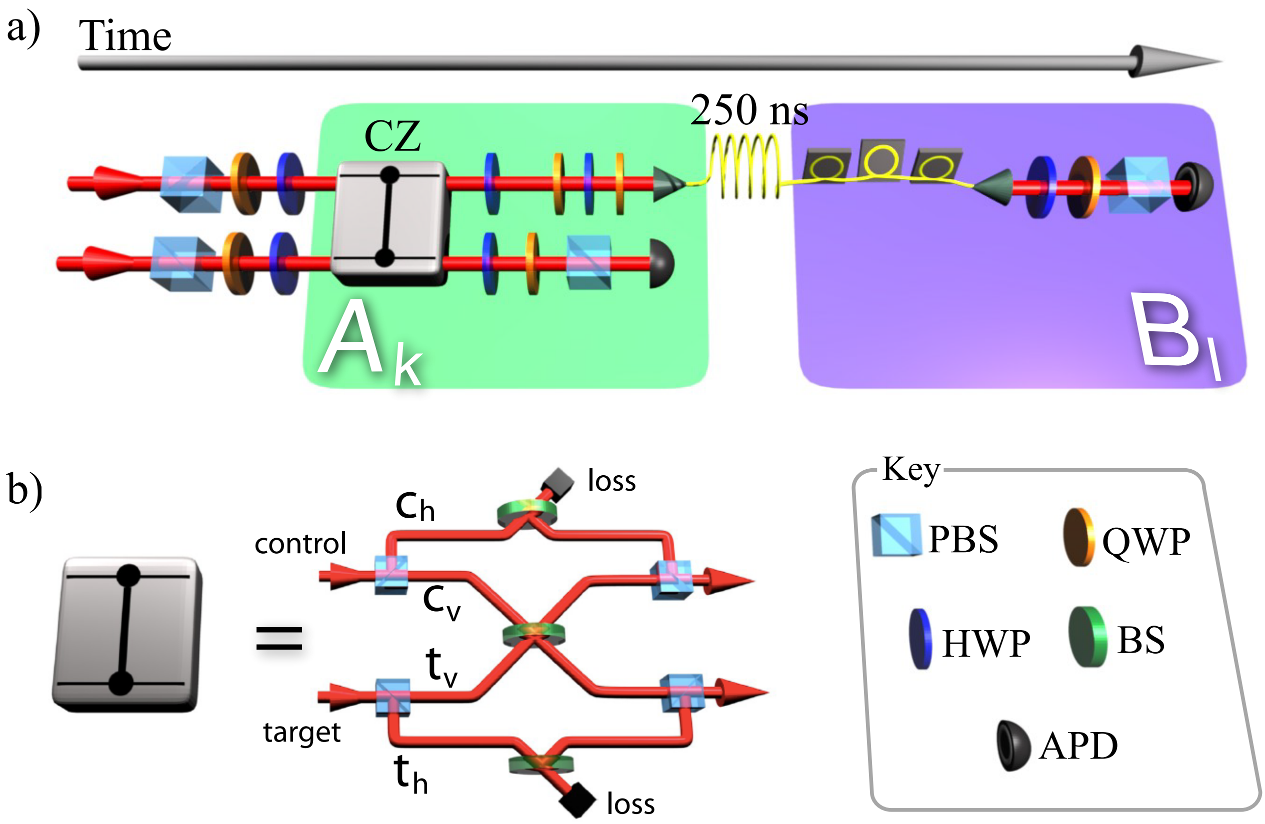

Figure 4.2: Experimental scheme. a) Temporal measurements. The signal and meter qubit are encoded in orthogonal polarization states of two single photons, which are created via spontaneous parametric down-conversion in a nonlinear crystal, pumped by a pulsed (76 MHz, 200 fs), frequency-doubled Ti:Sapphire laser at λ=820 nm. States are prepared with polarising beamsplitters (PBS), a quarter- (QWP) and a half-wave plate (HWP). The signal photon passes a controlled-phase gate (CZ), where it acts as the control qubit, with the meter photon being the target. Behind the gate, we analyze the meter photon polarization and detect it with a single-photon avalanche photo diode (APD), implementing the first measurement A_k. Two HWPs (one incorporated into the preparation stage) set the basis for this non-destructive measurement. The signal is stored in a 50 meter long fiber spool and, after A_k is concluded, measured projectively, implementing B_l. A fiber polarization controller and a combination of wave plates compensate for polarization rotation in the fiber. A coincidence logic analyzes detection events within a time window of 4.4 ns. b) The CZ gate in detail, here shown in dual-rail representation. We realize it with a single partially polarising beam splitter (PPBS), with reflectivities $\eta_V = 2/3$ ($\eta_H = 0$) for the H (V) polarisation [21, 22, 23]. Quantum interference results in a relative π phase shift of the vertical polarization components $|V\rangle_s |V\rangle_m$. The correct functioning is heralded by a coincidence count between the two output arms of the PPBS, which occurs with probability 1/9.

rotation must be undone at the gate output, as shown in Fig. 4.2.

We experimentally measured $P(1,1|1,1) = 0.2372 \pm 0.0040$, $P(1,1|0,0) = 0.0181 \pm 0.0008$, $P(1,0|1,0) = 0.0190 \pm 0.0013$, $P(0,1|0,1) = 0.0070 \pm 0.0005$, yielding

$$\mathcal{H}_{\text{exp}}{=}0.193{\pm}0.004,$$

which violates inequality (4.4) by 45 standard deviations.

The key feature is that this temporal version of Hardy's proof is considerably stronger than its spatial analogue, where the left-hand side of (4.4) can be no greater than ~ 0.09 [24]; our results surpass this limit by more than 24 standard deviations. The violation of Hardy's inequality in time can be achieved by any pure quantum state, provided that the observables are chosen appropriately.

4.3 CHSH inequality in time

Surprisingly, and in stark contrast to its spatial analogue, such pure states are not required for the Clauser-Horne-Shimony-Holt (CHSH) form of a temporal Bell inequality [27]. Unlike Hardy's paradox, the CHSH inequality considers correlations between points A and B. The two results will be correlated whenever $r = s$ and anti-correlated in the other case. Hence, the correlation function for two observables A_k and B_l is

$$C_{k,l}{=}\sum_{r,s}(-1)^{r+s}P(r,s|k,l). \tag{4.5}$$

By invoking realism and non-invasiveness to establish a bound on correlations one can then define the temporal Bell inequality [12]:

$$S = |C_{0,0} + C_{1,0} + C_{0,1} - C_{1,1}| \leq 2, \tag{4.6}$$

which has the same form as the CHSH inequality in the spatial domain [27]. Observing a value above 2 implies entanglement in time.

For a quantum state ρ, the expectation value of $C_{k,l}$ is

$$C_{k,l} = \mathrm{Tr}(\rho \cdot \frac{1}{2}[A_k, B_l]_+), \tag{4.7}$$

where $[A_k, B_l]_+$ is the anti-commutator of the measurement operators [14]. For a single qubit, a maximal violation of inequality 4.6, $S_{QM} = 2\sqrt{2}$, can be obtained by choosing appropriate measurements on the Bloch sphere. We select the same directions as in spatial CHSH experiments: $A_0{=}Z$, $A_1{=}X$, $B_0{=}(Z{+}X)/\sqrt{2}$ and $B_1{=}(Z{-}X)/\sqrt{2}$. Remarkably, the correlators $C_{k,l}$, in Eq. 4.7, and thus the parameter S do not depend on the choice of ρ, but only on the measurement operators. If we denote a_k and b_l as the directions associated with A_k and B_l, the correlation is simply given by [12] $C_{k,l}{=}a_k \cdot b_l$, and for the indicated set of measurements, we

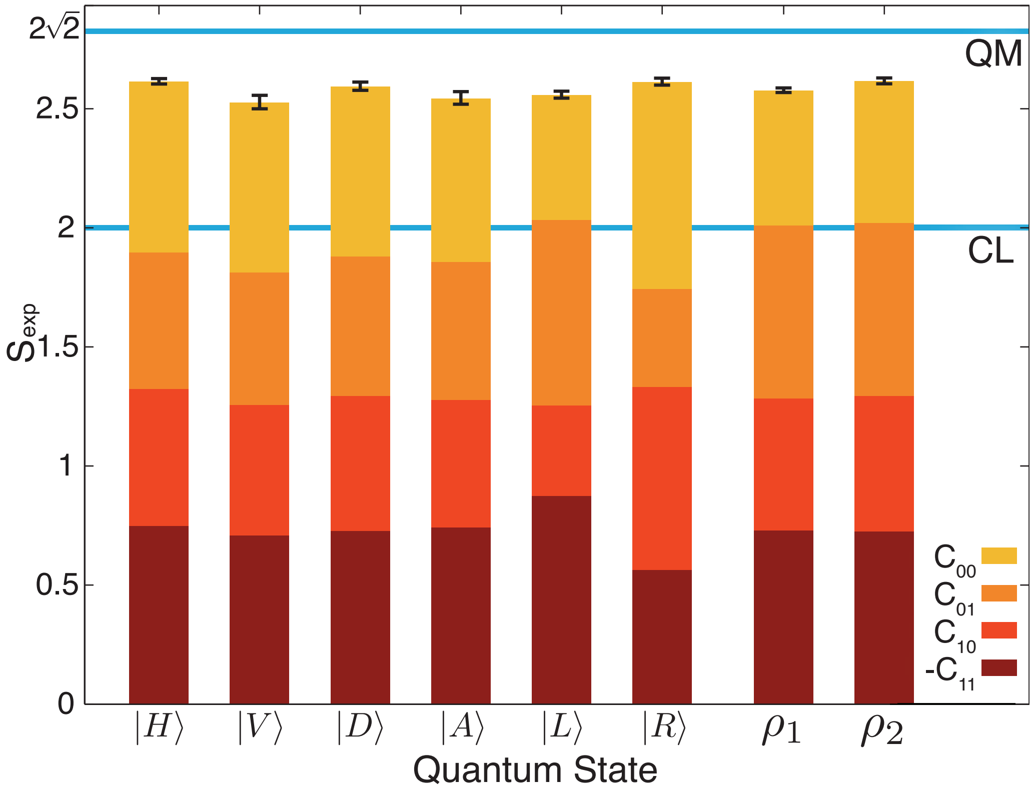

Figure 4.3: Experimental violation of the state-independent temporal Bell inequality (4.6). The classical limit is indicated by CL and the maximal achievable quantum value by QM. The first six bars correspond to pure signal states the remaining two to mixed inputs, as explained in the main text. The latter were obtained by switching the signal state between states $|D\rangle$ and $|A\rangle$ while measurements were performed. The relative integration for $|D\rangle$ and $|A\rangle$ were chosen according to the target purity of 0.5 for ρ_1 and 0.75 for ρ_2. The mixed states were verified via single-qubit tomography.

will reach a maximal violation for *any* quantum state. This is not the case for the Leggett-Garg form of a temporal Bell inequality [4, 5, 6].

We tested the temporal Bell inequality, Eq. (4.6), for a total of eight states; six (almost) pure input states, $\{|H\rangle, |V\rangle, |D\rangle, |A\rangle, |L\rangle, |R\rangle\}$; one mixed state $\rho_1{\sim}(0.84\,|H\rangle\,\langle H|+0.16\,|V\rangle\,\langle V|)$ with purity $\mathcal{P}$=0.74±0.01, and one fully mixed state $\rho_2{\sim}1/2(|H\rangle\,\langle H|+|V\rangle\,\langle V|)$ with purity $\mathcal{P}$=0.50±0.01. The experimental results for these states are summarised in Fig. 4.3. The obtained S-parameter was, on average,

$$S_{\text{exp}} = 2.58 \pm 0.03,$$

which violates inequality (4.6) by 19 standard deviations. It is quite remarkable that we get a clear violation even with a fully mixed state, for which one would—intuitively—not expect any evident quantum signature.

In spatial Bell demonstrations, a less-than-maximal violation is usually blamed on the quality of the prepared quantum state. For the state-independent temporal inequality here, it is due to imperfect measurement, which is in turn mainly limited by less-than-ideal two-photon interference in the gate. In simple terms, the observed Bell value corresponds to a two-point visibility of 0.91 ± 0.01. We can assess the measurement performance in more detail by performing quantum process tomography [28] on our gate. The experimental process χ_{exp} associated with the measurement has a purity of $92.4 \pm 0.2\%$ and a fidelity with an ideal CZ process of $93.7 \pm 0.1\%$. The error bounds are calculated from 10 Monte Carlo runs assuming Poissonian photon count statistics. The upper bound on the CHSH value (4.6), calculated from χ_{exp}, is 2.54 ± 0.01 averaged over all input states and, within error, in good agreement with the measured value. For the Hardy inequality (4.4), the estimated bound is 0.184 ± 0.003—slightly below the respective experimental result, which is most likely due to temporal drift in the optical setup.

4.4 Discussion

The study of temporal quantum phenomena provides a new resource for quantum information. The authors of [12], e.g., propose a temporal quantum communication complexity protocol where temporal entanglement provides a memory advantage over classical physics. It is conceivable that we can also find classically-impossible, or more efficient quantum communication tasks based on the strong quantum signature of temporal probabilities. A more fundamental question is—analogous to *non-local* realistic models [29, 30] for spatially separated systems—if, and to which degree, non-invasiveness might be relaxed while still allowing violation by quantum mechanics. Intriguingly, for the Leggett-Garg inequality, the connection between the measurement strength and the amount of violation is not straightforward: the less invasive the measurement, the higher the violation [6, 9].

Another topic is the link between temporal quantum phenomena and quantum contextuality [31]. Contextuality is a further example highlighting that quantum mechanics is incompatible with a classical worldview and, similar to the Bell inequality violation demonstrated here, this incompatibility can also be state-independent [32]. Ultimately, the fundamental differences of quantum effects in the two domains may teach us more about the structure of space and time and the abstract formalism of quantum theory [12].

4.5 Additional experimental details

Here we show explicitly that the probabilities given in inequality 4.1 and equations 4.2-4.3 are satisfied for the observables $A_0{=}B_1{=}-Z$, and $A_1{=}B_0{=}X$ and an initially prepared qubit state $|\mathbf{0}\rangle$. Each observable is dichotomic with outcomes $r, s{=}\{0,1\}$ given by the projection operators, or eigenvectors, of each observable. We define the projection operators as $\mathcal{A}_{i,j}$ and $\mathcal{B}_{i,j}$ for the measurement outcome i from a measurement choice of j for Alice and Bob respectively. They are given explicitly as,

$$\begin{aligned}\mathcal{A}_{0,0} &= \mathcal{B}_{0,1} = |\mathbf{0}\rangle\langle\mathbf{0}|\,, \;\; \mathcal{A}_{0,1} = \mathcal{B}_{0,0} = |-\rangle\langle-| \\ \mathcal{A}_{1,0} &= \mathcal{B}_{1,1} = |\mathbf{1}\rangle\langle\mathbf{1}|\,, \;\; \mathcal{A}_{1,1} = \mathcal{B}_{1,0} = |+\rangle\langle+|\,,\end{aligned} \tag{4.8}$$

where $|\pm\rangle = (|\mathbf{0}\rangle \pm |\mathbf{1}\rangle)/\sqrt{2}$. Alice makes her projective measurement first followed by Bob's, so from Eqs. 1.19 and 1.21 in section 1.1.7 we have that,

$$\begin{aligned}P(r,s|k,l) &= P_{\mathcal{A}}(r|k)\,\langle\psi'|\,\mathcal{B}_{s,l}\,|\psi'\rangle \\ &= \langle\mathbf{0}|\,\mathcal{A}^{\dagger}_{r,k}\mathcal{B}_{s,l}\mathcal{A}_{r,k}\,|\mathbf{0}\rangle\,,\end{aligned} \tag{4.9}$$

where $|\psi'\rangle$ is the state of the system after Alice's measurement and $P_{\mathcal{A}}(r|k)$ is the probability of measuring r after Alice's initial measurement $\mathcal{A}_{r,k}$. Here we have used the fact that after Alice's initial projective measurement $\mathcal{A}_{r,k}$, the state $|\psi\rangle$ is projected into the state $\mathcal{A}_{r,k}\,|\psi\rangle\,/\sqrt{P_{\mathcal{A}}(r|k)}$ with probability $P_{\mathcal{A}}(r|k)$. Importantly though, this measurement is non-destructive, leaving the state intact for the subsequent measurement $\mathcal{B}_{r,k}$. The explicit probabilities given in inequality 4.1 and equations 4.2-4.3 are

$$\begin{aligned}P(1,1|1,1) &= \langle\mathbf{0}\,|+\rangle\,\langle+\,|\mathbf{1}\rangle\,\langle\mathbf{1}\,|+\rangle\,\langle+\,|\mathbf{0}\rangle = 0.25 \\ P(1,0|1,0) &= \langle\mathbf{0}\,|+\rangle\,\langle+\,|-\rangle\,\langle-\,|+\rangle\,\langle+\,|\mathbf{0}\rangle = 0 \\ P(0,1|0,1) &= \langle\mathbf{0}\,|\mathbf{0}\rangle\,\langle\mathbf{0}\,|\mathbf{1}\rangle\,\langle\mathbf{1}\,|\mathbf{0}\rangle\,\langle\mathbf{0}\,|\mathbf{0}\rangle = 0 \\ P(1,1|0,0) &= \langle\mathbf{0}\,|\mathbf{1}\rangle\,\langle\mathbf{1}\,|+\rangle\,\langle+\,|\mathbf{1}\rangle\,\langle\mathbf{1}\,|\mathbf{0}\rangle = 0.\end{aligned} \tag{4.10}$$

4.6 Proposed extension: polygamy of temporal entanglement

An extension to this experiment is the investigation of quantum correlations between measurements made at *three* separate points in time. In this scenario, additional to Alice's and Bob's measurements, A_k and B_l at times t_1 and t_2 respectively, there is a third party who makes a measurement of the dichotomic observable D_m along the direction d_m at a time t_3. It can be shown that the two-fold correlation between the measurements performed at t_1 and t_3, where $t_1 < t_2 < t_3$, is given by [12]

$$C_{k,m} = (a_k \cdot b_l)(b_l \cdot d_m). \tag{4.11}$$

A correlation of this type for any projective measurement b_l, with the exception of when b_l=a_k [12], is incapable of violating the CHSH inequality defined in Eq. 4.6. One can think of the measurement b_l as "disentangling" the measurement outcomes at times t_1 and t_3 and therefore rending any correlations between them lost in the measurement process.

However, since the two-fold correlation function between consecutive measurements is independent of the initial state (see Eq. 4.7) we find that there exists just as strong a correlation between measurements A_k and B_l as between B_l and D_m. In contrast to the correlations between systems of 3 or more spatially separated qubits, which display a tradeoff between the number of entangled qubits and the total amount of distributed entanglement, or a "monogamy" of entanglement [33], in the temporal case there is no such tradeoff: there can be a "polygamy" of entanglement [12].

Experimentally both measurements A_k and B_l have to be non-destructive so we are required to implement the circuit shown in Fig. 4.4. At times t_1 and t_2, two non-destructive measurements A_k and B_l are implemented by a controlled-phase gate and the necessary basis rotations R_{A_k} and R_{B_l} respectively. Finally the usual destructive projective measurement D_m is made at the time t_3. A maximal violation of the CHSH inequality between measurements made at t_1-t_2 and t_2-t_3, could be achieved using the following set of measurement operators

$$\begin{aligned} A_0 &= D_0 = Z \\ B_0 &= (Z + X)/\sqrt{2} \\ A_1 &= D_1 = X \\ B_1 &= (Z - X)/\sqrt{2}. \end{aligned} \tag{4.12}$$

Importantly, the experiment depicted in Fig. 4.4 is feasible with current quantum optics capabilities. The circuit shown here is a simple extension of the one in Fig. 4.2 of the main text. It requires two non-deterministic CZ gates which perform subsequent non-destructive measurements on the signal qubit, giving a heralded success probability of $(1/9)^2$, see Section 2.2.4. Additionally, as such an experiment would require the use of two independent SPDC sources to generate two pairs of photons (three photons are used in the circuit, one is used as a trigger)

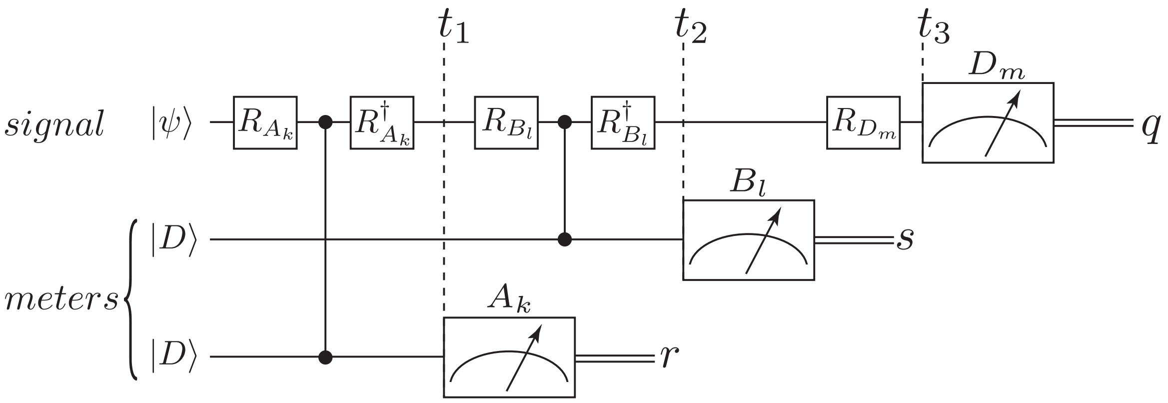

Figure 4.4: Circuit diagram to demonstrate the polygamy of temporal quantum correlations. An arbitrary state $|\psi\rangle$ is subject to two non-destructive measurements A_k and B_l, implemented by two controlled-phase gates, at times t_1 and t_2 respectively and a destructive projective measurement D_m at time t_3. The basis for each measurement is chosen by implementing the appropriate local rotations R on the signal qubit which is undone by $R^\dagger$ after the first two measurements. In the photonic implementation all qubits could be encoded onto the polarisation degree of freedom of single photons which themselves are generated by spontaneous parametric downconversion from two independent sources, see Section 2.2.5.

the count rates would be further lowered.

References

[1] Hardy, L. Nonlocality for two particles without inequalities for almost all entangled states. *Phys. Rev. Lett.* **71**, 1665–1668 (1993).

[2] Bell, J. On the problem of hidden variables in quantum mechanics. *Reviews of Modern Physics* **38**, 447–452 (1966).

[3] Aspect, A. Quantum mechanics - to be or not to be local. *Nature* **446**, 866–867 (2007).

[4] Leggett, A. J. & Garg, A. Quantum mechanics versus macroscopic realism: Is the flux there when nobody looks? *Phys. Rev. Lett.* **54**, 857–860 (1985).

[5] Jordan, A. N., Korotkov, A. N. & Büttiker, M. Leggett-Garg inequality with a kicked quantum pump. *Phys. Rev. Lett.* **97**, 26805 (2006).

[6] Williams, N. S. & Jordan, A. N. Weak values and the Leggett-Garg inequality in solid-state qubits. *Phys. Rev. Lett.* **100**, 26804 (2008).

[7] Kofler, J. & Brukner, Č. Conditions for quantum violation of macroscopic realism. *Phys. Rev. Lett.* **101**, 90403 (2008).

[8] Barbieri, M. Multiple-measurement Leggett-Garg inequalities. *Phys. Rev. A* **80**, 34102 (2009).

[9] Goggin, M. E. *et al.* Violation of the Leggett-Garg inequality with weak measurements of photons. *Proceedings of the National Academy of Sciences* (2011).

[10] Xu, J.-S., Li, C.-F., Zou, X.-B. & Guo, G.-C. Experimental violation of the Leggett-Garg inequality under decoherence. *Scientific Reports* **1** (2011).

[11] Palacios-Laloy, A. *et al.* Experimental violation of a Bell's inequality in time with weak measurement. *Nature Physics* **6**, 442–447 (2010).

[12] Brukner, C., Taylor, S., Cheung, S. & Vedral, V. Quantum entanglement in time. *arXiv:quant-ph/0402127v1* (2004).

[13] Lapiedra, R. Joint reality and Bell inequalities for consecutive measurements. *Europhysics Letters* **75**, 202 (2006).

[14] Fritz, T. Quantum correlations in the temporal Clauser-Horne-Shimony-Holt (CHSH) scenario. *New Journal of Physics* **12** (2010).

[15] Boschi, D., Branca, S., De Martini, F. & Hardy, L. Ladder proof of nonlocality without inequalities: Theoretical and experimental results. *Phys. Rev. Lett.* **79**, 2755–2758 (1997).

[16] White, A. G., James, D. F. V., Eberhard, P. H. & Kwiat, P. G. Nonmaximally entangled states: production, characterization, and utilization. *Phys. Rev. Lett.* **83**, 3103–3107 (1999).

[17] Barbieri, M., De Martini, F., Di Nepi, G. & Mataloni, P. Towards a test of non-locality without supplementary assumptions. *Phys. Lett. A* **334**, 23–29 (2005).

[18] Irvine, W. T. M., Hodelin, J. F., Simon, C. & Bouwmeester, D. Realization of Hardy's Thought Experiment with Photons. *Phys. Rev. Lett.* **95**, 30401 (2005).

[19] Lundeen, J. S. & Steinberg, A. M. Experimental joint weak measurement on a photon pair as a probe of Hardy's Paradox. *Phys. Rev. Lett.* **102**, 20404 (2009).

[20] Yokota, K., Yamamoto, T., Koashi, M. & Imoto, N. Direct observation of Hardy's paradox by joint weak measurement with an entangled photon pair. *New Journal of Physics* **11**, 033011 (2009).

[21] Langford, N. K. *et al.* Demonstration of a simple entangling optical gate and its use in Bell-state analysis. *Phys. Rev. Lett.* **95**, 21 (2005).

[22] Kiesel, N., Schmid, C., Weber, U., Ursin, R. & Weinfurter, H. Linear optics controlled-phase gate made simple. *Phys. Rev. Lett.* **95**, 210505 (2005).

[23] Okamoto, R., Hofmann, H. F., Takeuchi, S. & Sasaki, K. Demonstration of an optical quantum controlled-NOT gate without path interference. *Phys. Rev. Lett.* **95**, 210506 (2005).

[24] Mermin, N. D. Quantum mysteries refined. *American Journal of Physics* **62**, 880 (1994).

[25] Pryde, G. J., O'Brien, J. L., White, A. G., Bartlett, S. D. & Ralph, T. C. Measuring a photonic qubit without destroying it. *Phys. Rev. Lett.* **92**, 190402 (2004).

[26] Barbieri, M., Goggin, M. E., Almeida, M. P., Lanyon, B. P. & White, A. G. Complementarity in variable strength quantum non-demolition measurements. *New Journal of Physics* **11**, 093012 (2009).

[27] Clauser, J. F., Horne, M. A., Shimony, A. & Holt, R. A. Proposed Experiment to Test Local Hidden-Variable Theories. *Phys. Rev. Lett.* **23**, 880–884 (1969).

[28] O'Brien, J. L. *et al.* Quantum process tomography of a controlled-NOT gate. *Phys. Rev. Lett.* **93**, 080502 (2004).

[29] Gröblacher, S. *et al.* An experimental test of non-local realism. *Nature* **446**, 871–875 (2007).

[30] Branciard, C. *et al.* Testing quantum correlations versus single-particle properties within Leggett's model and beyond. *Nature Physics* **4**, 681–685 (2008).

[31] Kochen, S. & Specker, E. The problem of hidden variables in quantum mechanics. *J. Math. Mech.* **17**, 59 (1967).

[32] Kirchmair, G. *et al.* State-independent experimental test of quantum contextuality. *Nature* **460**, 494–497 (2009).

[33] Coffman, V., Kundu, J. & Wootters, W. K. Distributed entanglement. *Phys. Rev. A* **61**, 052306 (2000).

Part II

Quantum Walks

CHAPTER 5

Introduction to Quantum Walks

In this chapter we lay out a mathematical framework for dealing with quantum walks. However, to begin with we will remind ourselves of the classical random walk, or "drunkards" walk [1]. The classical random walk [1] describes the motion of a particle moving in random directions in space. The mathematical formalism of a random walk is the basis for describing physical processes from diffusion of molecules in liquids (Brownian motion), to economics where it is used to model the stock markets. Its most basic form is that of a single particle, on a 1-dimensional lattice, which moves either left or right randomly at each time interval. Such a system is identical to that of an old style 'Galton board' shown in Fig. 5.1a. When the particle has an equal probability of moving left or right at each time step, or walk iteration, the probability of finding the particle at a position x on the lattice after $N \gg 1$ steps approaches a normal distribution given by,

$$p(x, N) = \frac{2}{\sqrt{2N\pi}} e^{-\frac{x^2}{2N}}. \tag{5.1}$$

5.1 Quantum walks

A quantum walk describes the motion of a quantum particle on a lattice and is the quantum analogue of the classical random walk. The key difference between quantum and classical random walks is the presence of coherence in the quantum case. This leads to interference and therefore drastically different probability distributions which unlike the classical case have a strong dependence on the initial state of the quantum walker. In addition, the walker can spread much faster than is classically possible. We quantify the spread of the walker using the standard deviation which, for discrete variables as in the case of a walker's lattice, is given by,

$$\text{S.D.} = \sqrt{\sum_i p_i(x_i - \bar{x})}, \quad \text{with} \quad \bar{x} = \sum_i^N p_i x_i, \tag{5.2}$$

where p_i is the probability of being at lattice position x_i after N steps. In the quantum case the standard deviation scales linearly with the number of steps N, as opposed to $\sqrt{N}$ in the classical case, see Fig. 5.2. The idea of a quantum particle moving about on a lattice and interfering with itself can be traced back as early as 1958 [2] although the term 'quantum random' walk was not coined until much later in 1993 by Aharonov *et. al.* [3]. In this more recent paper, Aharonov *et.*

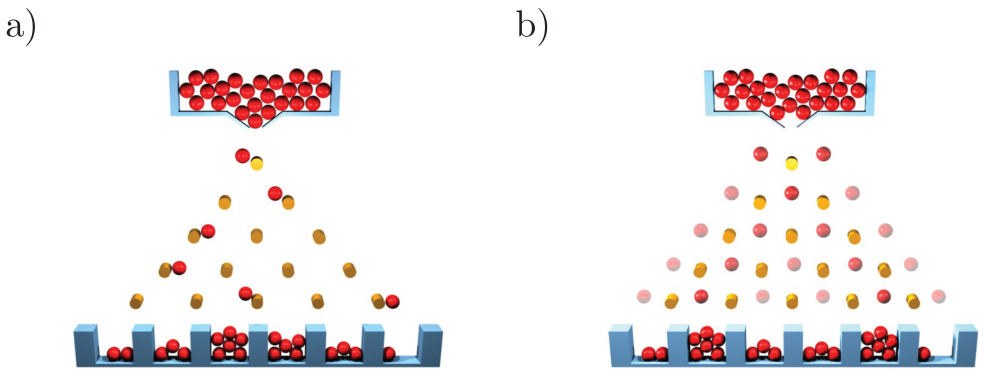

Figure 5.1: Classical random walks and quantum walks. a) The Galton board is an example of a physical system that exhibits the properties of a classical random walk. In the game balls fall from the top and encounter pegs which they bounce off of, either going left or right. The final distribution of balls at the bottom is a binomial distribution. b) A toy example of a quantum Galton board. Instead of bouncing left or right at each peg of the Galton board, a quantum particle is placed in a *coherent* superposition of left and right. The final probability distribution in the quantum case is starkly different from the classical one. In b the transparency of the balls represent the probability of finding the ball at that position and time step.

al. describe the relationship between the quantum 'coin' and position of the walker and even go on to describe a physical implementation of a quantum walk using an optics experiment.

There are two limits to the time evolution of quantum walks: *discrete*− and *continuous*−time. In both cases the quantum walker spreads coherently across a lattice, but in the discrete case the walker has an encoded 'coin' state that determines the direction it moves at each time step and lattice position. In the continuous-time quantum walk the walker does not have an internal coin state, but couples constantly to other lattice positions.

5.2 Discrete-time quantum walks

In the discrete case the walker exists in a Hilbert space made up of its 'coin' and position states. The coin state is encoded into the internal state of the walker and in the simplest case is a two level quantum state, or a qubit defined in the computational basis as

$$|\psi_{coin}\rangle = \alpha\,|\mathbf{0}\rangle + \beta\,|\mathbf{1}\rangle\,, \tag{5.3}$$

where $|\alpha|^2 + |\beta|^2 = 1$, see Section 1.1.1. The position state of the walker is a coherent superposition of discrete lattice positions, j, such that

$$|\psi_{pos}\rangle = \sum_j c_j\,|j\rangle\,, \tag{5.4}$$

where $\sum_j |c_j|^2 = 1$. The total state of the walker is given by the tensor product of these two states, $|\Psi\rangle = |\psi_{coin}\rangle \otimes |\psi_{pos}\rangle$.

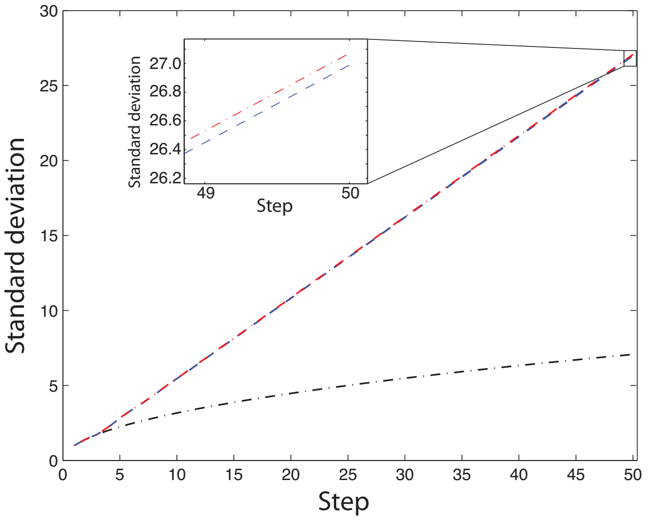

Figure 5.2: Theoretical standard deviation of quantum (blue and red lines) and classical (black line) random walks calculated using Eq. 5.2. Due to coherent interference a quantum walker spreads much faster than a classical one. Although the final probability distribution of the quantum walk is highly dependent on the initial state of the walker, the standard deviations for the six pure initial states $\{|\mathbf{0}\rangle, |\mathbf{1}\rangle, |+\rangle, |-\rangle\}$ (blue line) and $\{|+i\rangle, |-i\rangle\}$ (red line) show little difference in the spread of the walker, shown by the inset.

Each step of the quantum walk is composed of two operators that act independently on these two degrees of freedom. The coin operator C, is an arbitrary rotation of the qubit state $|\psi_{coin}\rangle$ and the shift, or translation operator S, couples the coin state to the lattice positions j and is given by

$$S = \sum_j |j-1\rangle \langle j| \otimes |\mathbf{0}\rangle \langle \mathbf{0}| + |j+1\rangle \langle j| \otimes |\mathbf{1}\rangle \langle \mathbf{1}| . \tag{5.5}$$

Given that the walker evolves coherently between each time step the state of the walker at time $t = N\delta t$ is given by

$$|\Psi(t)\rangle = W^N |\Psi(0)\rangle = (SC)^N |\Psi(0)\rangle , \tag{5.6}$$

where W is the one step operator and $|\Psi(0)\rangle = |\psi_{coin}\rangle |\psi_{pos}\rangle$ is the initial state of the walker. The most widely studied coin operator is the Hadamard, H (discussed earlier in Section 1.1.6), which does the following transformation to the initial coin state,

$$H \begin{bmatrix} \alpha \\ \beta \end{bmatrix} = \frac{1}{\sqrt{2}} \begin{bmatrix} 1 & 1 \\ 1 & -1 \end{bmatrix} \begin{bmatrix} \alpha \\ \beta \end{bmatrix} = \frac{1}{\sqrt{2}} \begin{bmatrix} \alpha + \beta \\ \alpha - \beta \end{bmatrix} . \tag{5.7}$$

This coin operator creates an equal superposition state in the computational basis and for this reason it is often referred to as the unbiased coin. Figure 5.3 shows a number of quantum walk probability distributions using the unbiased coin for various initial states after N=50 steps.

For homogeneous quantum walks, the walker experiences the same coin operator at every lattice position, and it is these types of walks that produce the signature ballistic spread of the walker with a standard deviation N, shown in Fig. 5.2. However, in the more general case

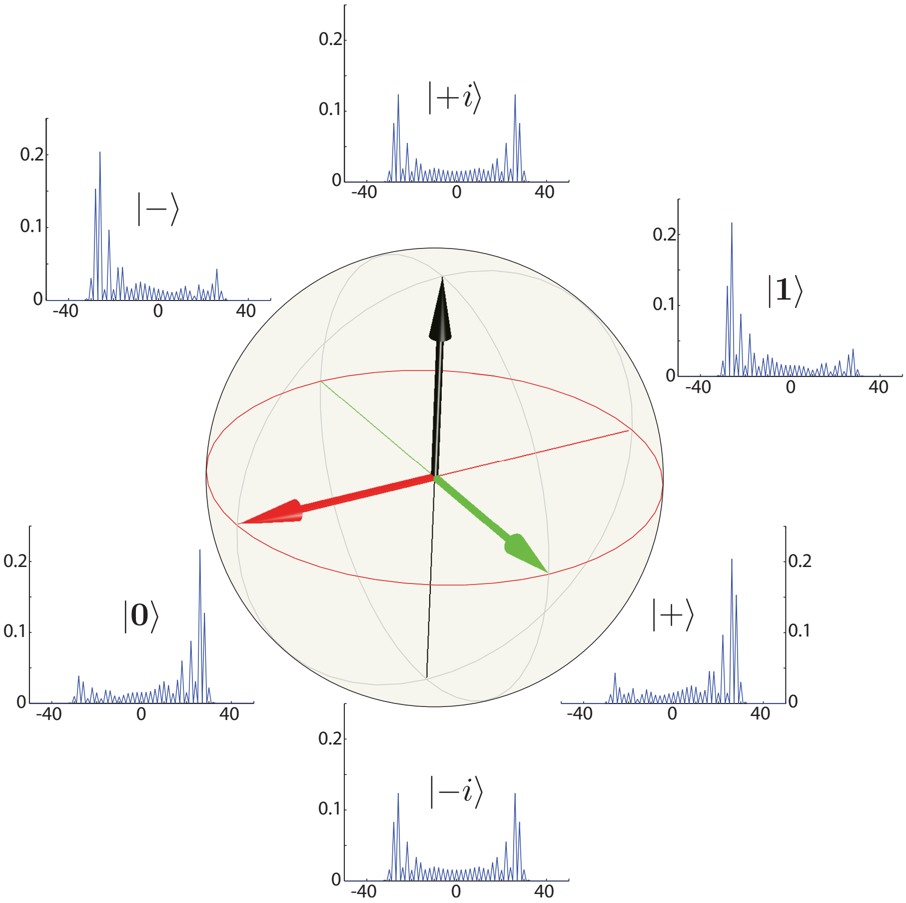

Figure 5.3: Theoretical quantum walk probability distributions for various initial states, shown on each graph in the ket and depicted on the qubit sphere. Each graph shows the lattice position on the $x-$axis and the probability of detection on the $y-$axis. The number of steps, N, in every case is 50.

of inhomogeneous quantum walks the walker can be subject to different coin rotations at each lattice position [4]. This class of quantum walks is examined further in Chapter 7, where we create a boundary between two topologically distinct quantum walks and observe interesting behaviour at its interface.

5.3 Continuous-time quantum walks

Unlike in the discrete-time case the walker has no internal coin state in a continuous-time quantum walk, instead the walk occurs entirely in position space and experiences a continuous coupling to adjacent lattice sites. The continuous-time quantum walk was first described by E. Farhi and S. Gutmann and we will use their formalism here [5]. We define the N position states of the walker with an orthonornal set of states $\{|i\rangle\}$, where i=$1, \ldots, N$ and $\langle i\,|j\,\rangle = \delta_{i,j}$. The Hamiltonian with matrix elements $H_{i,j}$, describing the coupling between sites i and j is

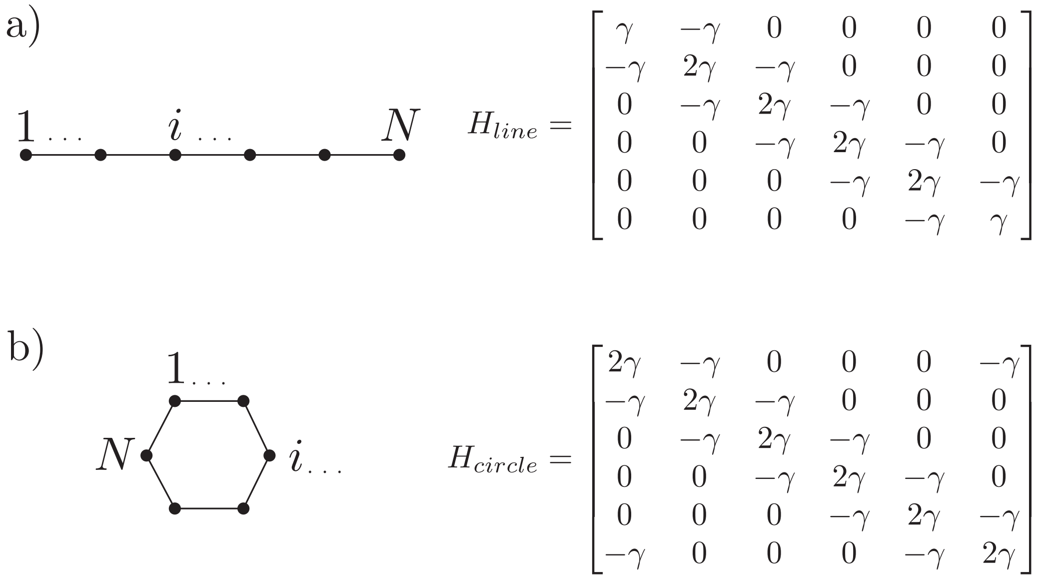

$$H_{line} = \begin{bmatrix} \gamma & -\gamma & 0 & 0 & 0 & 0 \\ -\gamma & 2\gamma & -\gamma & 0 & 0 & 0 \\ 0 & -\gamma & 2\gamma & -\gamma & 0 & 0 \\ 0 & 0 & -\gamma & 2\gamma & -\gamma & 0 \\ 0 & 0 & 0 & -\gamma & 2\gamma & -\gamma \\ 0 & 0 & 0 & 0 & -\gamma & \gamma \end{bmatrix}$$

$$H_{circle} = \begin{bmatrix} 2\gamma & -\gamma & 0 & 0 & 0 & -\gamma \\ -\gamma & 2\gamma & -\gamma & 0 & 0 & 0 \\ 0 & -\gamma & 2\gamma & -\gamma & 0 & 0 \\ 0 & 0 & -\gamma & 2\gamma & -\gamma & 0 \\ 0 & 0 & 0 & -\gamma & 2\gamma & -\gamma \\ -\gamma & 0 & 0 & 0 & -\gamma & 2\gamma \end{bmatrix}$$

Figure 5.4: Pictorial representation of continuous-time quantum walk graphs. a) The walker spreads out along a line and will experience a reflection at the edges of the lattice. b) In the case of a circular graph the walker is subject to periodic boundary conditions, signified by the extra off diagonal elements in the Hamiltonian.

given by

$$\langle i| H |j\rangle = \begin{cases} -\gamma_{i,j} & \text{if } i \neq j \text{ and } i \text{ is connected to } j \\ 0 & \text{if } i \neq j \text{ and } i \text{ is not connected to } j \\ d_i\gamma_{i,j} & \text{if } i = j \end{cases}, \tag{5.8}$$

where d_i is the degree of position i, specifying how many adjacent sites it is connected to, and the coupling rate between sites i and j is given by $\gamma_{i,j}$. That is, a particle at site i has a probability $\gamma_{i,j}\delta t$ of being at site j after a time δt and in general all the $\gamma_{i,j}$'s can be different. Figure 5.4 shows two commonly studied graphs, the line and circle, and gives the Hamiltonians in the cases where all $\gamma_{i,j}$'s are equal.

To determine the time dynamics, that is the probability of finding the walker at a particular position state $|i\rangle$ at time t, we define the state

$$|\Psi(t)\rangle = \sum_i C_i(t) |i\rangle , \tag{5.9}$$

where $\sum_i |C_i(t)|^2 = 1$ for all t, and project it onto the i^{th} position state. The probability amplitudes evolve under a Schrödinger like equation given by,

$$
\begin{aligned}
i\frac{\partial \langle i\,|\Psi(t)\rangle}{\partial t} &= \langle i|\,H\,|\Psi(t)\rangle \\
i\frac{\partial C_i(t)}{\partial t} &= d_i\gamma_{i,i}C_i(t) - \sum_j \gamma_{i,j}C_j(t).
\end{aligned}
\tag{5.10}
$$

The probability of finding the walker at site i at time t is given by $P_i(t){=}\,|C_i(t)|^2$.

5.4 Motivations for studying quantum walks

Perhaps the most discussed application of the quantum walk formalism is in quantum computing. This prospect came out of work by Childs [6] and Lovett [7] who showed that quantum walks, in the continuous- and discrete-time regimes respectively, are universal for quantum computation, but did so only for a single quantum walker. However, there is a caveat to these proofs, which is that while the formalism of quantum walks has been proven to be universal for quantum computation, the physical resources required to implement a quantum algorithm scale exponentially with the size of the problem in the single walker scenario, therefore rending them inefficient for quantum computation. The proof then becomes non-useful in the sense that one would never consider encoding a large quantum algorithm into the quantum walk formalism because of this scaling issue. Multiple walkers on the other hand may be the answer to this scalability problem [8]. With multiple walkers one is able to produce true multi-partite entanglement, a resource that has been shown to be crucial in the development of many quantum algorithms [9]. Recently it was shown by Childs *et al.* [10] that multiple-walker continuous-time quantum walks can indeed be used to perform efficient universal quantum computation.

For a quantum system, specifying the potential that a particle moves in determines its Hamiltonian and therefore through the Schödinger equation, the particle's time dynamics. The quantum walk formalism therefore provides a perfect model for studying coherent transport of excitations between different potential sites [11, 12]. By creating the correct particle potential, one is able to emulate a variety of interesting physical systems using quantum walks. Interesting examples include the simulation of Zitterberwegung (trembling motion) [13], Klein tunnelling [14], Anderson localisation [15] and topological phases [16]. The last of these is an experiment performed as part of this thesis and is the subject of Chapter 7. Another recent proposal yet to be realised, uses the continuous-time quantum walk as a model system for energy transport in photosynthetic systems [17, 18]. In 2007 the authors of [19] found that long-lived quantum coherence plays a substantial role in the energy transfer mechanisms of the Fenna-Matthews-Olsen (FMO) complex in green sulphur bacteria. Subsequently, it was shown by the authors of [17] and [18] that the system could be modelled as an excitation undergoing a continuous-time quantum walk lattice. Interestingly, they found that added decoherence in the quantum walk could be responsible for the high energy-transfer efficiencies in FMO complex, in a process called environmentally-assisted quantum-transport.

The prospects of performing quantum computations and quantum simulations with quantum walks provide the motivation for their experimental realisations. As a contribution to this effort in the next three chapters we present three quantum walk experiments with single and multiple photon inputs.

References

[1] Pearson, K. The problem of the random walk. *Nature* **72**, 294 (1905).

[2] Riazanov, G. V. The feynman path integral for the dirac equation. *Soviet Phys. JETP* **6**, 1107 (1958).

[3] Aharonov, Y., Davidovich, L. & Zagury, N. Quantum random walks. *Phys. Rev. A* **48**, 1687 (1993).

[4] Linden, N. & Sharam, J. Inhomogeneous quantum walks. *Phys. Rev. A* **80**, 052327 (2009).

[5] Farhi, E. & Gutmann, S. Quantum computation and decision trees. *Phys. Rev. A* **58**, 915–928 (1998).

[6] Childs, A. M. Universal computation by quantum walk. *Phys. Rev. Lett.* **102**, 180501 (2009).

[7] Lovett, N. B., Cooper, S., Everitt, M., Trevers, M. & Kendon, V. Universal quantum computation using the discrete-time quantum walk. *Phys. Rev. A* **81**, 042330 (2010).

[8] Rohde, P. Are quantum walks the saviour of optical quantum computing? *arXiv:1010.4608v2* (2010).

[9] Bruß, D. & Macchiavello, C. Multipartite entanglement in quantum algorithms. *Phys. Rev. A* **83**, 052313 (2011).

[10] Andrew M Childs, D. G. & Webb, Z. Universal computation by multi-particle quantum walk. *arXiv:1205.3782v1* (2012).

[11] Mülken, O. & Blumen, A. Continuous-time quantum walks: Models for coherent transport on complex networks. *Physics Reports* **502**, 37–87 (2011).

[12] Longhi, S. Quantum-optical analogies using photonic structures. *Laser and Photonics Reviews* **3**, 243–261 (2009).

[13] Dreisow, F. *et al.* Classical simulation of relativistic Zitterbewegung in photonic lattices. *Phys. Rev. Lett.* **105**, 143902 (2010).

[14] Dreisow, F. *et al.* Klein tunneling of light in waveguide superlattices. *Europhysics Letters* **97**, 10008 (2012).

[15] Naether, U. *et al.* Anderson localization in a periodic photonic lattice with a disordered boundary. *Opt. Lett.* **37**, 485–487 (2012).

[16] Kitagawa, T. *et al.* Observation of topologically protected bound states in photonic quantum walks. *Nature Communications* **3** (2012).

[17] Mohseni, M., Rebentrost, P., Lloyd, S. & Aspuru-Guzik, A. Environment-assisted quantum walks in photosynthetic energy transfer. *J. Chem. Phys.* **129**, 174106 (2008).

[18] Plenio, M. B. & Huelga, S. F. Dephasing-assisted transport: quantum networks and biomolecules. *New Journal of Physics* **10**, 113019 (2008).

[19] Engel, G. S. *et al.* Evidence for wavelike energy transfer through quantum coherence in photosynthetic systems. *Nature* **446**, 782–786 (2007).

CHAPTER 6

Discrete single-photon quantum walks with tunable decoherence

Published: *Physical Review Letters* **104**, 153602 (2010)

M. A. Broome[1], A. Fedrizzi[1], B. P. Lanyon[1], I. Kassal[2], A. Aspuru-Guzik[1] and A. G. White[1]

[1]Department of Physics and Centre for Quantum Computer Technology, University of Queensland, Brisbane 4072, Australia
[2]Department of Chemistry and Chemical Biology, Harvard University, Cambridge MA 02138, United States

Abstract

Quantum walks have a host of applications, ranging from quantum computing to the simulation of biological systems. We present an intrinsically stable, deterministic implementation of discrete quantum walks with single photons in space. The number of optical elements required scales linearly with the number of steps. We measure walks with up to 6 steps and explore the quantum-to-classical transition by introducing tunable decoherence. Finally, we also investigate the effect of absorbing boundaries and show that decoherence significantly affects the probability of absorption.

6.1 Introduction

The random walk is a fundamental model of dynamical processes that has found extensive application in science. The quantum walk (QW) is the extension of the random walk to the quantum regime [1, 2]. Here, the classical walker is replaced by a quantum particle, such as an electron, atom or photon, and the stochastic evolution by a unitary process. A key difference is that the many possible paths of the quantum walker can exhibit interference, leading to a very different probability distribution for finding the walker at a given location.

An important motivation for work on QW's have been their applications to quantum computation: not only were they instrumental to Feynman's original quantum computer (as the clock mechanism [3]), but it has since been shown that they represent a universal computational primitive [4, 5] and have inspired novel quantum algorithms [6, 7, 8]. QW's have also been used to analyze energy transport in biological systems [9, 10].

Despite a few early experimental demonstrations [11, 12, 13, 14], experimentalists have only recently begun to develop the level of control over single quantum particles required to implement discrete-time QW's, leading to demonstrations with neutral atoms in position space [15], ions in phase space [16, 17] and single photons in time [18]. Continuous-time quantum walks have different outcomes, applications and experimental challenges, see, e.g., [19].

6.2 Quantum walks with single photons

In this work, we present discrete-time QW's of single photons in space. Our approach is robust, due to the use of intrinsically stable interferometers, yet highly versatile—enabling control over every operation at every step of the walk. Of particular interest is the ability to introduce a controlled amount of decoherence, which we use to explore the quantum-to-classical transition. Besides being of fundamental interest, decoherence in QW's can improve the performance of certain computational protocols [20] and is particularly important in their application to describing energy transport [9, 10]. Finally, we investigate the effect of introducing absorbing boundaries into the walk, as theoretically investigated by [21, 22].

The simplest random walk occurs on a one-dimensional lattice. The particle begins at one site and each step of the walk consists of a move to a neighboring site on the left or right, determined by the outcome of a coin flip. In the analogous QW, the coin is represented by a two-level quantum system whose orthogonal levels we will designate $|H\rangle$ (horizontal) and $|V\rangle$ (vertical). Each step of the QW starts with an analogue of the coin flip: a unitary *coin operator* C is applied to the coin space. An unbiased, or Hadamard, coin operator transforms the coin so that $|H\rangle \rightarrow |D\rangle = (|H\rangle + |V\rangle)/\sqrt{2}$,
$|V\rangle \rightarrow |A\rangle = (|H\rangle - |V\rangle)/\sqrt{2}$. Following each coin operation is the *shift operator*,

$$S = \sum_j |j-1\rangle \langle j| \otimes |H\rangle \langle H| + |j+1\rangle \langle j| \otimes |V\rangle \langle V| , \tag{6.1}$$

which moves the particles to one of the neighboring lattice sites, conditional on the quantum coin state. Therefore, the operation $W = SC$ makes up a single step of the QW, and a walker in an initial state $|\psi\rangle$ is found in the state $W^N |\psi\rangle$ after N steps.

The quantum and random walks can be considered the extremes of a spectrum, with pure quantum evolution turning into classical evolution if there is sufficient decoherence [23, 24, 25]. In addition, all the intermediate walks are special cases of the broad category of quantum stochastic walks [26]. Various mechanisms of decoherence have been studied [25]; here we consider pure dephasing, since this corresponds to the decoherence mechanism in our experiment. The system is described by a density matrix ρ which at each step undergoes the evolution

$$\rho_{N+1} = (1-q)W\rho_N W^\dagger + q\sum_i K_i W\rho_N W^\dagger K_i^\dagger, \tag{6.2}$$

where the Kraus operators $K_i = |i\rangle\langle i|$ correspond to pure dephasing. The parameter q is the probability of a dephasing event occuring at each step. If $q = 0$, the walk is a pure QW, while $q = 1$ reproduces the random walk. Note that to observe the quantum-to-classical transition, gradual decoherence must be applied at each step, not just to the initial coin state [23, 24, 25].

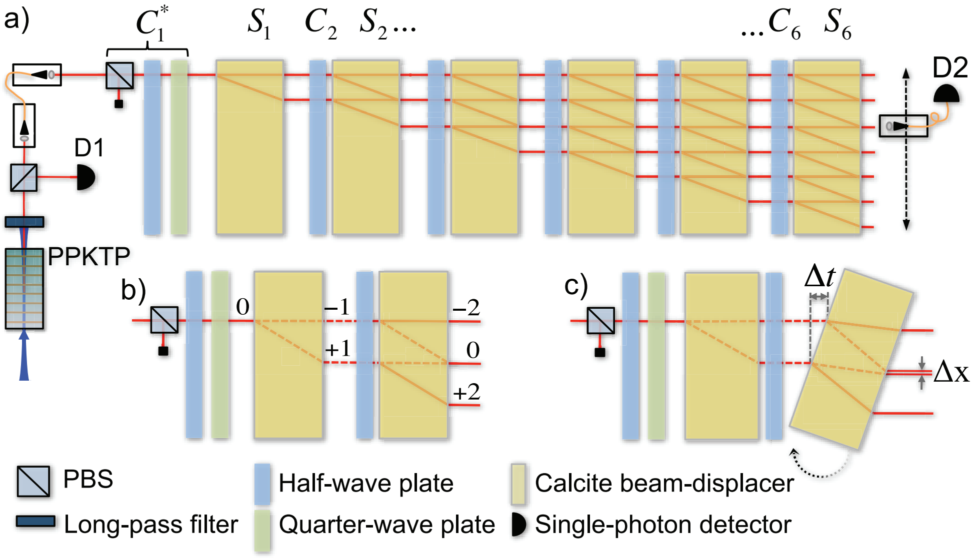

Figure 6.1: Experimental schematic. a) From each pair of single photons created via spontaneous parametric downconversion in a PPKTP crystal, one is injected into the free-space mode “0” of the quantum walk. Arbitrary initial coin (polarization) states are prepared by the first polarizing beam splitter (PBS) and waveplate combination. Six pairs of coin (C_i) and shift (S_i) operators implement six steps of the walk. Coincident detection of photons at detectors D2 and D1 (4.4 ns time window) herald a successful run of the walk. b) Details of our optical mode numbering convention for the first two steps. The dashed lines trace out one of the interferometers which are used to align the quantum walk. c) A relative angle between two beam displacers reduces the recombined photon’s temporal (Δt) and spatial (Δx) mode overlap, thereby implementing tunable decoherence.

6.3 Experimental setup

Our implementation of the discrete QW on a line represents a polarization analogue of the originally proposed linear-optical version of the Galton board based on beamsplitters and phase-shifters [27, 13]. A similar, polarization-encoded setup has been proposed for cube polarizing beamsplitters [28]. Figure 6.1a shows a schematic of the experiment.

Pairs of single photons were created via type-II spontaneous parametric downconversion in a, non-linear, potassium titanyl phosphate (PPKTP) crystal. This crystal was pumped by a 5 mW diode laser centred at 410 nm and emitted orthogonally polarized photon pairs with a wavelength of 820 nm and a FWHM bandwidth of 0.6 nm. The pairs were separated at a polarizing beamsplitter; one photon from each pair served as a trigger, while the second photon was launched into the QW. At an average heralded photon rate of $\sim$20,000 s^{-1}, the mean longitudinal distance between two photons was about 250,000 times longer than the setup length of $\sim$60 cm. The probability of randomly creating more than one photon pair simultaneously was $\sim 9 \cdot 10^{-5}$, i.e., only one photon was in the setup at any given time.

Quantum coin states were encoded in the polarization $|H\rangle$ and $|V\rangle$ of the input photon. Throughout our experiment, the initial coin state was set to left-circular polarization, $|L\rangle = (|H\rangle + i\,|V\rangle)/\sqrt{2}$, using a quarter- and a half-wave plate, leading to symmetric probability distributionsm, see Fig. 5.3 in Section 5.2. For the results presented here, the remaining coin operators C were Hadamards, realised with half-wave plates set to 22.5°. We can, however, prepare arbitrary pure input states as well as arbitrary coin operators for each step with suitable wave plate settings.

The lattice sites of the QW were represented by longitudinal spatial modes. The shift operator S acting on these modes was implemented by a 27 mm long, birefringent calcite beam-displacer. The displacers had a clear aperture of 20×10 mm^2 and were mounted on manual, tip-tilt rotation stages with a resolution of $217\mu\mathrm{rad}/5^\circ$ turn. The optical axis of each calcite prism was cut so that vertically polarized light was directly transmitted and horizontal light underwent a 2.7 mm lateral displacement into a neighboring mode. Lattice sites were, typical for discrete walks on a line, labeled so that there were odd sites at odd time steps and even sites at even times.

The first two steps of the QW are shown in detail in Fig. 6.1b. The spatial modes after step 1 were recombined interferometrically in step 2. A series of steps then formed an interferometric network, Fig. 6.1a. We aligned this network iteratively, to a single interferometer per step. For example, the second beam displacer was aligned to maximize the interference visibility of the interferometer in Fig. 6.1b: the state $|D\rangle$ was input in mode "0" and the beam displacer rotated to maximize the overlap of the output mode "0" with $|D\rangle$. The third displacer was then aligned to the second and so on. We reached interference visibilities of typically $\sim$ 99.8% per step.

The photons emerging in the $N+1$ spatial modes at the output of an N-step QW were coupled into an optical fiber and subsequently detected by a single-photon avalanche photodiode, in coincidence with the trigger photon. We measured the probability distributions sequentially, translating the fiber coupler between the individual modes using a manual translation stage.

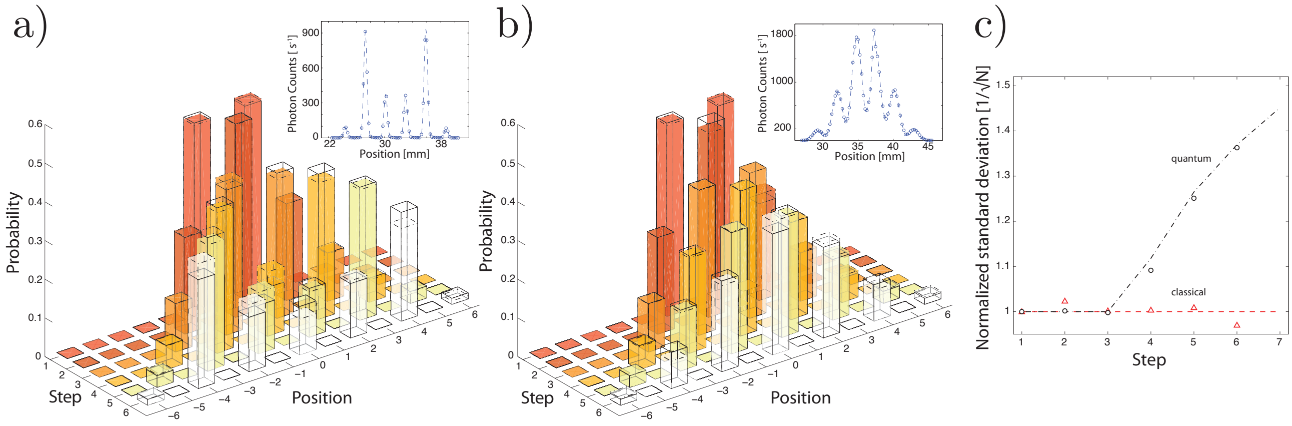

Figure 6.2: Probability distributions for successive steps of the a) quantum and b) fully decohered (classical) walks up to the sixth step. Dashed lines show experimental data and solid lines show theoretical predictions. Probabilities are obtained by normalizing photon counts at each position to the total number of counts for the respective step. The insets show horizontal scans across the walk lattice for the 5-step quantum walk (coupled into single-mode fiber) and decohered random walk (multi-mode fiber), respectively. c) Normalized standard deviation of the probability distribution for quantum (black circles) and classical (red triangles) walks for 1 to 6 steps. Lines show the theoretical values; error bars are smaller than symbol size.

6.4 Results

The measured probability distributions for detecting the photon at a given site, for 1 to 6 steps, are shown in Fig. 6.2a. The experimental data is in excellent agreement with theory, with an average L_1-norm distance, given by,

$$d=\frac{1}{2}\sum_i \left|p_i^{exp}-p_i^{th}\right|, \tag{6.3}$$

of 0.031 for the coherent and 0.017 for the decohered walks. The quality of our data degrades somewhat for a higher number of steps, largely due to non-planar optical surfaces, which caused small relative phase shifts between the multiple interferometers. The decohered walk is insensitive to phase errors and therefore better agrees with theory.

Our scheme has several advantages: first, the interferometric network is inherently stable. The transversal mode-match is fulfilled because two beams emerging from one displacer will always be parallel, independent of small deviations in the optical alignment. The stability and alignment procedure of the QW grid are facilitated by the fact that the N interferometers between steps N and $(N{+}1)$ are formed between only 2 optical components. Our setup—even though it is interferometric—does therefore not require active phase locking. Secondly, our system scales well, with the number of optical components increasing as $2N$ (as opposed to

$(N^2+N)/2$ in [27, 13]), and exhibits low optical loss of $\sim 1\%$ per step. The remaining obstacle to scalability are non-ideal optical components, a problem that can be alleviated with careful manufacturing or the use of shorter displacers.

6.4.1 Implementing decoherence

A unique feature of this setup is that tunable decoherence can be introduced by intentional misalignment of QW steps, Fig. 6.1c. Setting a non-zero relative angle between neighboring beam displacers leads to both a temporal delay and a transversal mode mismatch between interfering wave packets. Because the coincidence time window was much longer than the temporal shift we essentially integrated over the timing information, which corresponds to dephasing, cf. Eq. 6.2. Similarly, we traced over the spatial mode information by coupling the photons into a multi-mode fiber—as opposed to the single-mode fiber used for the coherent walks shown in Fig. 6.2a. In practice, this reduced the interference contrast in all interferometers in the respective step. The QW was fully decohered (q=1 in Eq. 6.2) when the interference visibility in each individual step reduced to 0, which occured at a relative angle of 10.5° in our experiment. Figure 6.2b shows the experimental results given by our system at full decoherence for steps 1 to 6. The probabilities—as expected for a classical random walk—follow a binomial distribution around the origin.

A distinguishing feature of an ideal QW is the speed at which the walker traverses the line. In particular, the standard deviation of the QW is proportional to the number of steps and not, as for the classical walk, its square root [2]. This has been exploited to design quantum-walk–based search algorithms that exhibit a Grover-like quadratic speedup [7]. The measured standard deviations for both our quantum and fully decohered walks are shown in Fig. 6.2c. The results show very good agreement with theory: the fully decohered walk spreads diffusively, while the quantum walk spreads ballistically.

Tunable decoherence enabled us to investigate the quantum-to-classical transition for a 5-step walk. By applying Eq. 6.2 to a two-step walk, see Fig. 6.1b, we calculated the interference visibility in output mode “0” after the second beam-displacer as a function of the decoherence q. We then adjusted the relative angle, Fig. 6.1c, between beam displacers to a target visibility. Fig. 6.3 shows the resulting probability distributions, compared to theory (Eq. 6.2).

6.4.2 Investigating absorbers in a quantum walk

Finally, we demonstrate another qualitative difference between classical and quantum walks, by incorporating absorbing boundaries. While a classical walker is eventually absorbed in the presence of an absorbing boundary, a quantum walker escapes with probability $1-2/\pi$ [21, 22]. A difference between the two exit probabilities first occurs after 5 steps, making it experimentally accessible with our current setup and providing a novel way of characterizing the degree of coherence in the walk. Absorbing boundaries were implemented using beam blocks in every “-1” spatial mode. Figure 6.4 shows the measured single photon transmission probabilities in

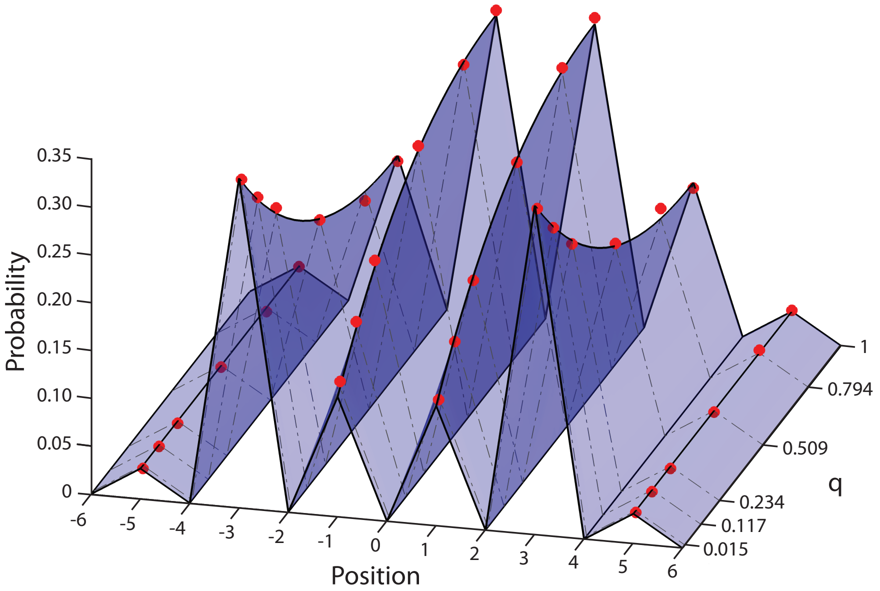

Figure 6.3: Transition of a 5-step quantum walk to a classical random walk. The decoherence parameter q for a given data set was obtained from a least-squares fit to theory, Eq. 6.2. All error bars are smaller than symbol size; the shaded area represents the theoretical probability distributions.

the quantum and fully decohered (classical) cases.

6.5 Discussion

The most compelling features of our scheme are the ability to add tunable decoherence to a QW and the fact that every individual lattice site is fully accessible at any given time step. Future work could be to implement random or position-dependent coin operators to study walks on random environments [29], inhomogeneous walks [30] and topological insulators [31]. Indeed, in Chapter 7 we present an experimental study of inhomogeneous quantum walks in the context of their topological properties.

Importantly, the results we have presented in this work rely only on single particle interference, that is to say, the single particle quantum walk behaviour is obtainable using classical light fields alone. Should one wish to obtain truly non-classical behaviour, the introduction of two or more walkers is required. In our case we could add another walker on a separate line, using the existing setup with a vertical offset between input beams, or on the same line, with two or more photons launched in the same (or neighboring) spatial modes. This would allow exploration of entangled QW's [32], as high-quality polarization-entangled photons can be routinely produced at high rates [33]. Finally, the setup can be used to prepare photon-number and path-entangled states across a large number of modes [34].

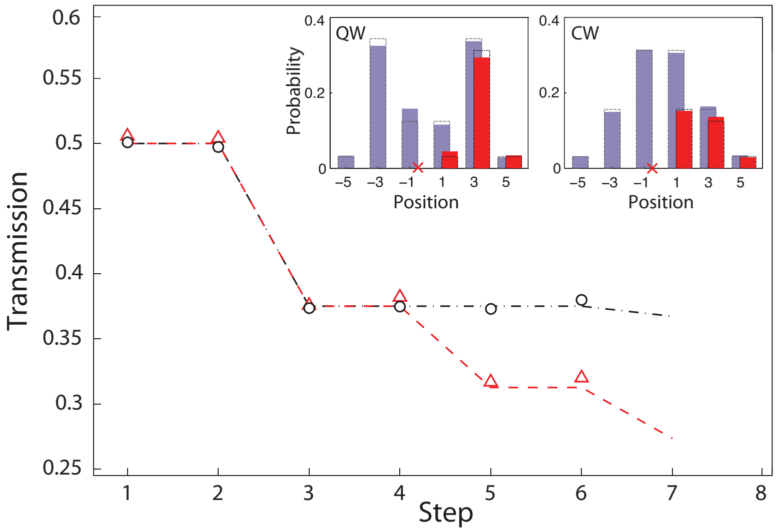

Figure 6.4: Transmission probability of quantum (black circles) and classical (red triangles) walkers with an absorber located at position −1 and initial coin state $|L\rangle$. The transmission was obtained as the ratio of the number of transmitted photons measured with absorbers in place to the number measured without them. Error bars are smaller than symbol size. The insets show the fifth step walk with an absorber at position −1 (red columns) compared to the original walk (blue columns) for the quantum (QW) and classical case (CW).

6.6 Note: Limitations of single-particle quantum walks

Although the number of optical elements in our physical quantum walk architecture scales efficiently ($2N$) with the number of optical modes N, following the previous argument laid out in Section 5.4 of this thesis, all single particle quantum walks scale inefficiently for performing scalable quantum computation. In our case the number of optical modes for example would scale exponentially as 2^N, meaning a useful quantum computation would require an exponential number of resources. This scalability flaw rules out the use of single particle quantum walks for any type of universal quantum computation.

Recent work however [35] shows that with the introduction of multiple particles—in particular those subject to bosonic statistics such as photons—it becomes computationally intractable to predict the probability distributions as the number of particles increases. It has been proposed that this is due to the path entanglement generated by the multiple walkers, leading to an exponential scaling of the number of parameters required to describe such a system of multiple walkers [36]. A more formal argument is given in the work of Asronson and Arkhipov [35] who show that calculating multi-photon scattering probabilities in linear optical networks is equivalent to the computationally intractable problem of calculating the permanents sub-matricies of the unitary evolution describing the optical network. The computational problem, dubbed BosonSampling [35], has also been shown to be isomorphic with the quantum walk formalism [37].

6.7 Proposed extension: Multi-photon quantum walks

To explore multiple walkers with our photonic setup we could implement the scenario depicted in Fig. 6.5. In this setup both photons from the spontaneous parametric downconversion source are injected into the walk setup at positions -1 and $+1$. Each photon is then subject to the same initial state preparation and subsequent coins operators using half- and quarter-wave plates as in the single photon case. Theoretical probability distributions for coincident photon measurements at the output are shown in Fig. 6.6.

Importantly, if the photons are injected into the setup at the same time, and are entirely indistinguishable, they will exhibit photon bunching throughout the walk seen as a generalised Hong-Ou-Mandel interference (see Section 2.2.4). As a measure of this non-classical interference the right-most column of Fig. 6.5 shows the visibility of interference at modes i and j, which is defined as

$$\mathcal{V}_{i,j} = \frac{P^{dist}_{i,j} - P^{ind}_{i,j}}{P^{dist}_{i,j}} \tag{6.4}$$

where $P^{dist}_{i,j}$ and $P^{ind}_{i,j}$ are the probabilities of observing a coincident photon pair at modes i and j for distinguishable and indistinguishable photons respectively.

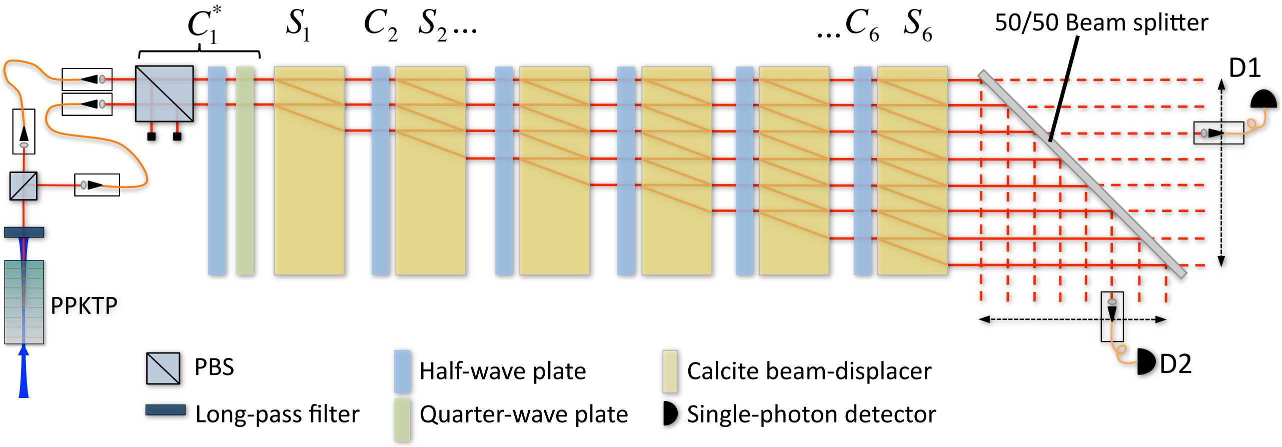

Figure 6.5: Experimental setup for a two-photon discrete-time quantum walk. Two photons are created via spontaneous parametric downconversion and injected into the quantum walk setup at lattice positions -1 and $+1$. The coin state of each photon is initialised using a polarising beam splitter and a half- and quarter-wave plate. After the photons propagate through the optical network they are detected using two single photon detectors, D1 and D2. The 50/50 beam splitter at the output ensures that we can measure two photons in the same optical mode, however, it comes at the expense of a 50% reduction in the overall coincident photon count rate.

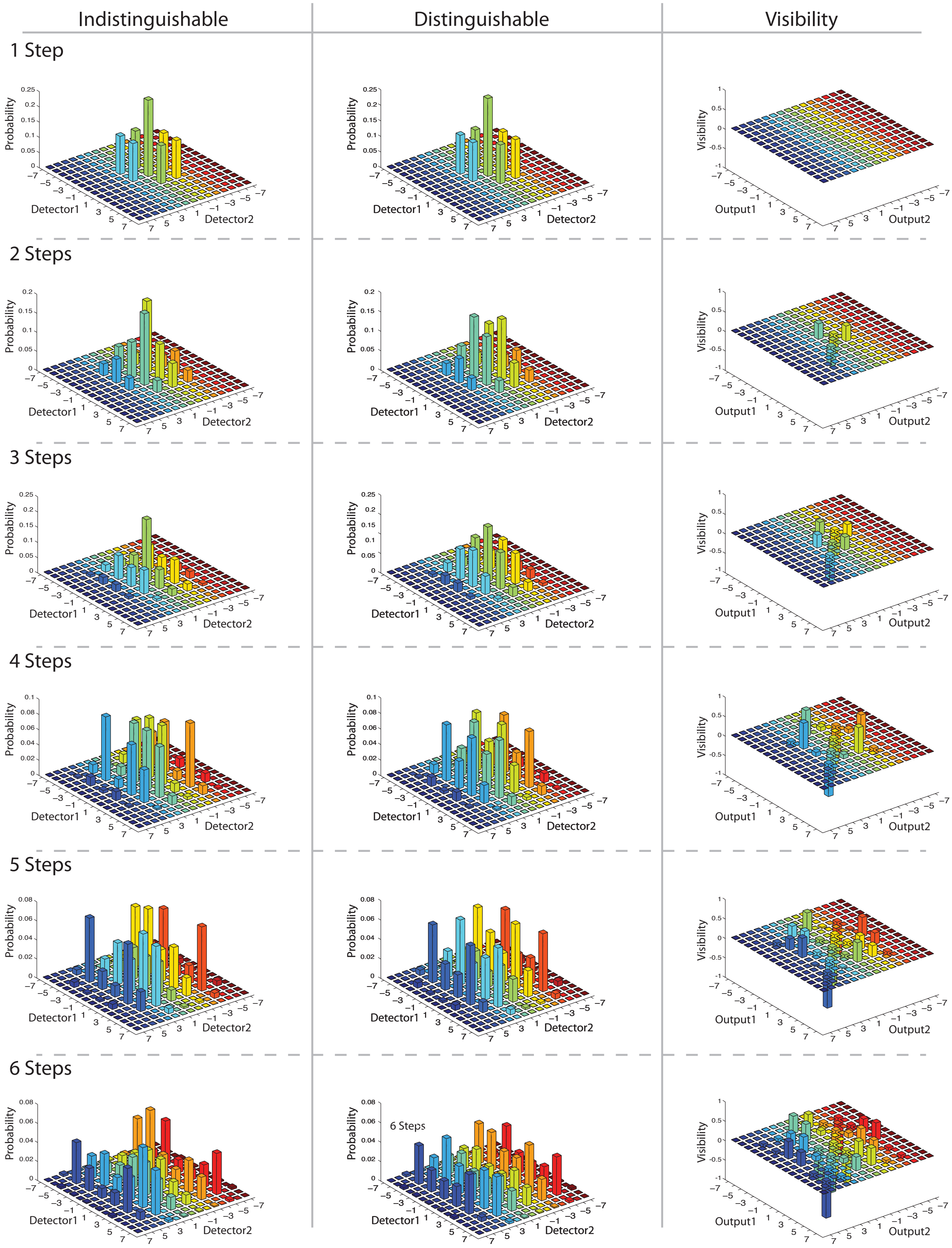

Figure 6.6: Probability distributions for two-photon quantum walks initialised at positions -1 and $+1$, each with the initial coin state $|R\rangle = |H\rangle - i\,|V\rangle$. The plots show the probability of detecting coincident photons at detectors 1 and 2 at the positions indicated on the horizontal axes for indistinguishable photons (left column) and distinguishable photons (centre column). The visibility for each step is plotted on in the right column.

References

[1] Aharonov, Y., Davidovich, L. & Zagury, N. Quantum random walks. *Phys. Rev. A* **48**, 1687 (1993).

[2] Kempe, J. Quantum random walks - an introductory overview. *Contemp. Phys.* **44**, 307 (2003).

[3] Feynman, R. Quantum mechanical computers. *Found. Phys.* **16**, 507 (1986).

[4] Childs, A. M. Universal computation by quantum walk. *Phys. Rev. Lett.* **102**, 180501 (2009).

[5] Lovett, N. B., Cooper, S., Everitt, M., Trevers, M. & Kendon, V. Universal quantum computation using the discrete-time quantum walk. *Phys. Rev. A* **81**, 042330 (2010).

[6] Childs, A. *et al.* Exponential algorithmic speedup by quantum walk. In *Proc. 35th Annual ACM Symposium on the Theory of Computing*, 59–68 (2003).

[7] Shenvi, N., Kempe, J. & Whaley, K. B. Quantum random-walk search algorithm. *Phys. Rev. A* **67**, 052307 (2003).

[8] Ambainis, A. Quantum walk algorithm for element distinctness. *SIAM J. Comput.* **37**, 210 (2007).

[9] Mohseni, M., Rebentrost, P., Lloyd, S. & Aspuru-Guzik, A. Environment-assisted quantum walks in photosynthetic energy transfer. *J. Chem. Phys.* **129**, 174106 (2008).

[10] Rebentrost, P., Mohseni, M., Kassal, I., Lloyd, S. & Aspuru-Guzik, A. Environment-assisted quantum transport. *New Journal of Physics* **11**, 033003 (2009).

[11] Bouwmeester, D., Marzoli, I., Karman, G. P., Schleich, W. & Woerdman, J. P. Optical galton board. *Phys. Rev. A* **61**, 013410 (1999).

[12] Ryan, C. A., Laforest, M., Boileau, J. C. & Laflamme, R. Experimental implementation of a discrete-time quantum random walk on an NMR quantum-information processor. *Phys. Rev. A* **72**, 062317 (2005).

[13] Do, B. *et al.* Experimental realization of a quantum quincunx by use of linear optical elements. *J. Opt. Soc. Am. B* **22**, 499 (2005).

[14] Souto Ribeiro, P. H., Walborn, S. P., Raitz, C., Davidovich, L. & Zagury, N. Quantum random walks and wave-packet reshaping at the single-photon level. *Phys. Rev. A* **78**, 012326 (2008).

[15] Karski, M. *et al.* Quantum walk in position space with single optically trapped atoms. *Science* **325**, 174–177 (2009).

[16] Zähringer, F. *et al.* Realization of a quantum walk with one and two trapped ions. *Phys. Rev. Lett.* **104**, 100503 (2010).

[17] Schmitz, H. *et al.* Quantum walk of a trapped ion in phase space. *Phys. Rev. Lett.* **103**, 090504 (2009).

[18] Schreiber, A. *et al.* Photons walking the line: A quantum walk with adjustable coin operations. *Phys. Rev. Lett.* **104**, 050502 (2010).

[19] Bromberg, Y., Lahini, Y., Morandotti, R. & Silberberg, Y. Quantum and classical correlations in waveguide lattices. *Phys. Rev. Lett.* **102**, 253904 (2009).

[20] Kendon, V. & Tregenna, B. Decoherence can be useful in quantum walks. *Phys. Rev. A* **67**, 042315 (2003).

[21] Ambainis, A., Bach, E., Nayak, A., Vishwanath, A. & Watrous, J. One-dimensional quantum walks. In *Proc. 33rd Annual ACM Symposium on the Theory of Computing*, 37–49 (2001).

[22] Bach, E., Coppersmith, S., Goldschen, M. P., Joynt, R. & Watrous, J. One-dimensional quantum walks with absorbing boundaries. *J. Comput. Syst. Sci.* **69**, 562 (2004).

[23] Brun, T. A., Carteret, H. A. & Ambainis, A. Quantum to classical transition for random walks. *Phys. Rev. Lett.* **91**, 130602 (2003).

[24] Kendon, V. & Sanders, B. Complementarity and quantum walks. *Phys. Rev. A* **71**, 022307 (2005).

[25] Kendon, V. Decoherence in quantum walks – a review. *Math. Struct. Comp. Sci.* **17**, 1169–1220 (2006).

[26] Rodriguez-Rosario, C. A., Whitfield, J. D. & Aspuru-Guzik, A. Quantum stochastic walks: A generalization of classical random walks and quantum walks. *Phys. Rev. A* **81**, 022323 (2010).

[27] Jeong, H., Paternostro, M. & Kim, M. Simulation of quantum random walks using the interference of a classical field. *Phys. Rev. A* **69**, 12310 (2004).

[28] Zhao, Z. *et al.* Implement quantum random walks with linear optics elements. *arXiv:quant-ph/0212149* (2002).

[29] Yin, Y., Katsanos, D. & Evangelou, S. Quantum walks on a random environment. *Phys. Rev. A* **77**, 22302 (2008).

[30] Linden, N. & Sharam, J. Inhomogeneous quantum walks. *Phys. Rev. A* **80**, 052327 (2009).

[31] Kitagawa, T., Rudner, M. S., Berg, E. & Demler, E. Exploring topological phases with quantum walks. *Phys. Rev. A* **82**, 033429 (2010).

[32] Omar, Y., Paunkovic, N., Sheridan, L. & Bose, S. Quantum walk on a line with two entangled particles. *Phys. Rev. A* **74**, 042304 (2006).

[33] Fedrizzi, A., Herbst, T., Poppe, A., Jennewein, T. & Zeilinger, A. A wavelength-tunable fiber-coupled source of narrowband entangled photons. *Opt. Express* **15**, 15377–15386 (2007).

[34] Papp, S. *et al.* Characterization of multipartite entanglement for one photon shared among four optical modes. *Science* **324**, 764 (2009).

[35] Aaronson, S. & Arkhipov, A. The computational complexity of linear optics. *Proceedings of the 43rd annual ACM symposium on Theory of computing. ACM* (2011).

[36] Rohde, P. P., Schreiber, A., Štefaňák, M., Jex, I. & Silberhorn, C. Multi-walker discrete time quantum walks on arbitrary graphs, their properties and their photonic implementation. *New Journal of Physics* **13**, 013001 (2011).

[37] Rohde, P. P. & Ralph, T. C. Error tolerance of the boson-sampling model for linear optics quantum computing. *Phys. Rev. A* **85**, 022332 (2012).

CHAPTER 7

Observation of topologically protected bound states in photonic quantum walks

Published: *Nature Communications* **3**, 882 (2012)

T. Kitagawa[1†], M. A. Broome[3†], A. Fedrizzi[3], M. S. Rudner[1], E. Berg[1], I. Kassal[2],
A. Aspuru-Guzik[2], E. Demler[1], A. G. White[3],
[1]Department of Physics and [2]Department of Chemistry and Chemical Biology, Harvard University,
Cambridge MA 02138, United States,
[3]ARC Centre for Engineered Quantum Systems and ARC Centre for Quantum Computation and Communication Technology, School of Mathematics and Physics, University of Queensland, Brisbane 4072, Australia
†These authors contributed equally to this work.

Abstract

Topological phases exhibit some of the most striking phenomena in modern physics. Much of the rich behaviour of quantum Hall systems, topological insulators, and topological superconductors can be traced to the existence of robust bound states at interfaces between different topological phases. This robustness has applications in metrology and holds promise for future uses in quantum computing. Engineered quantum systems—notably in photonics, where wavefunctions can be observed directly—provide versatile platforms for creating and probing a variety of topological phases. Here we use photonic quantum walks to observe bound states between systems with different bulk topological properties and demonstrate their robustness to perturbations—a signature of topological protection. While such bound states are usually discussed for static (time-independent) systems, here we demonstrate their existence in an explicitly time-dependent situation. Moreover, we discover a new phenomenon: a topologically protected pair of bound states unique to periodically driven systems.

7.1 Introduction

PHASES of matter have long been characterised by their symmetry properties, with each phase classified according to the symmetries that it possesses [1]. The discovery of the integer and fractional quantum Hall effects in the 1980s has led to a new paradigm, where quantum phases of matter are characterised by the topology of their ground-state wavefunctions. Since then, topological phases have been identified in physical systems ranging from condensed-matter [2, 3, 4, 5, 6, 7, 8, 9] and high-energy physics [10] to quantum optics [11] and atomic physics [12, 13, 14, 15].

Topological phases of matter are parametrised by integer topological invariants. As integers cannot change continuously, a consequence is exotic phenomena at the interface between systems with different values of topological invariants. For example, a topological insulator supports conducting states at the surface, precisely because its bulk topology is different to that of its surroundings [9, 8]. Creating and studying new topological phases remains a difficult task in a solid-state setting because the properties of electronic systems are often hard to control. Using controllable simulators may be advantageous in this respect.

Here we simulate one-dimensional topological phases using a discrete time quantum walk [16], a protocol for controlling the motion of quantum particles on a lattice. We create regions with distinct values of topological invariants and directly image the wavefunction of bound states at the boundary between them. The controllability of our system allows us to make small changes to the Hamiltonian and demonstrate the robustness of these bound states. Finally, using the quantum walk we can access the dynamics of strongly driven systems far from the static or adiabatic regimes [17, 18, 19], to which most previous work on topological phases has been restricted. In this regime, we discover a topologically protected pair of non-degenerate bound states, a phenomenon that is unique to periodically driven systems.

7.2 Results

7.2.1 Split-step quantum walks

Discrete time quantum walks have been realised in several physical architectures [20, 21, 22, 23, 24]. Here we use the photonic setup demonstrated in ref. [24] to implement a variation of these walks, the split-step quantum walk [25] of a single photon, with two internal states encoded in its horizontal, $|H\rangle$, and vertical, $|V\rangle$, polarisation states. The quantum walk takes place on a one dimensional lattice (Fig. 7.1). One step of the split-step quantum walk consists of four steps. First, a polarisation rotation $R(\theta_1)$ of the single photon is achieved with a suitable wave plate (see Methods), then a polarisation-dependent translation T_1 of $|H\rangle$ to the right by one lattice site using a calcite beam displacer. This is followed by a second rotation $R(\theta_2)$, and finally another translation T_2 of $|V\rangle$ to the left. The quantum walk is implemented by repeated applications of the one-step operator $U(\theta_1, \theta_2)=T_2R(\theta_2)T_1R(\theta_1)$.

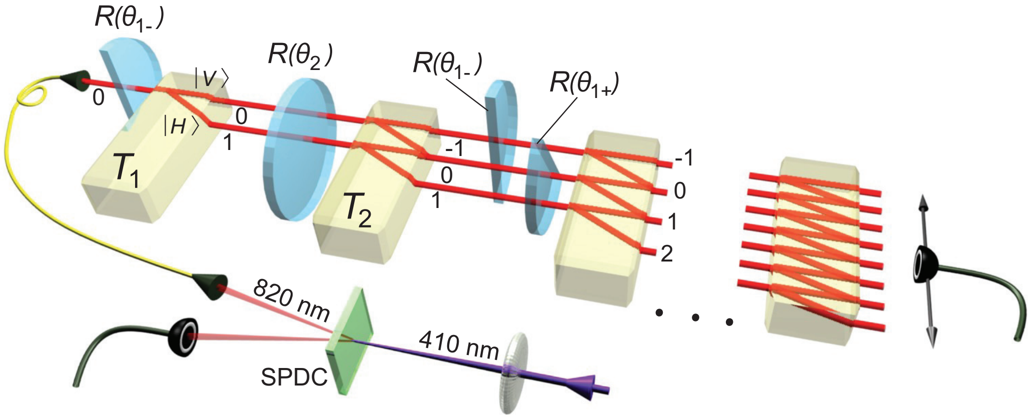

Figure 7.1: Experimental scheme for split-step quantum walks. A polarisation-encoded single photon, created via spontaneous parametric downconversion (SPDC), undergoes a succession of steps consisting of polarisation rotations, $R(\theta_1), R(\theta_2)$, and translations, T_1, T_2, which displace $|H\rangle$ to the right and $|V\rangle$ to the left, respectively. The rotations are implemented by half-wave plates while the translations are implemented using birefringent calcite beam displacers. To probe the topological properties of the quantum walk, semi-circular half-wave plates are used to create spatially inhomogeneous rotations, $R(\theta_{1-})$, $R(\theta_{1+})$ for lattice positions $x \leq 0$ and $x > 0$ respectively. The photon starts near the boundary between $R(\theta_{1-})$ and $R(\theta_{1+})$ at the lattice position '0' and is therefore subject to the rotation $R(\theta_{1-})$ initially. From then on as the photon spreads throughout the interferometer it is subject to both rotations that make up $R(\theta_1)$. The output probability distribution is imaged with a single-photon avalanche detector.

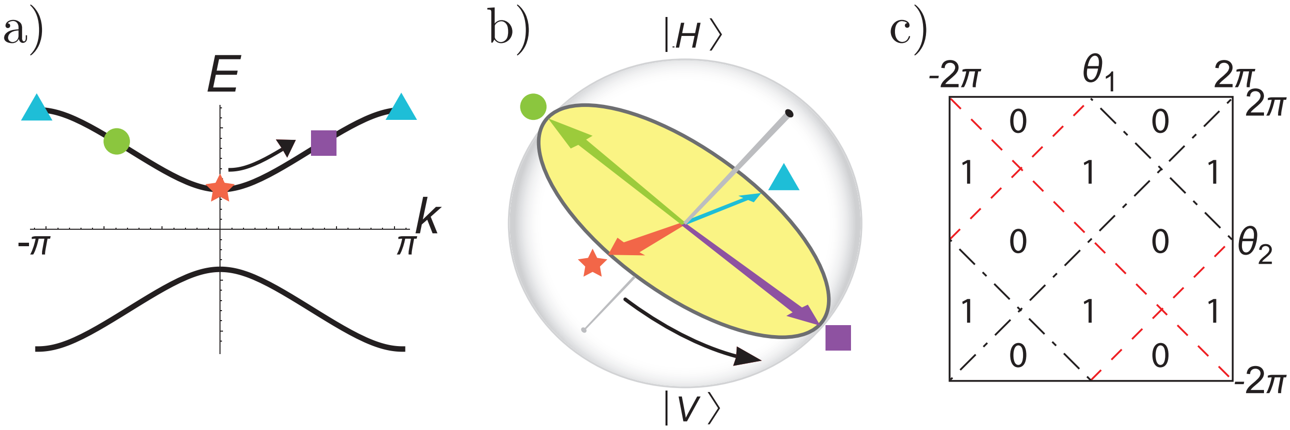

Figure 7.2: Band structure and phase diagram of split-step quantum walks. a) A typical band structure of the effective Hamiltonian $H_{\text{eff}}(\theta_1, \theta_2)$ for the split-step quantum walk (here, $\theta_1{=}\pi/2$ and $\theta_2{=}0$). For most θ_1 and θ_2, the spectrum displays a gap. b) Topology of $H_{\text{eff}}(\theta_1, \theta_2)$. Each eigenstate of $H_{\text{eff}}(\theta_1, \theta_2)$ consists of a quasi-momentum k (see Methods Section 7.4.2) and a corresponding polarisation, shown here on a Bloch sphere using the symbols from a. As k runs from $-\pi$ to π (black arrow in a), the polarisation follows a closed trajectory around a great circle (black arrow in b). The winding number of this trajectory, W, characterises the topology of $H_{\text{eff}}(\theta_1, \theta_2)$. c) Phase diagram of $H_{\text{eff}}(\theta_1, \theta_2)$ that shows the winding number W as a function of θ_1 and θ_2. The transition lines correspond to points where the spectral gap of $H_{\text{eff}}(\theta_1, \theta_2)$ closes at eigenvalues $E{=}0$ (black dash-dotted line) and $E{=}\pi$ (red dashed line).

The propagation of the photon in the static experimental setup can be described by an effective time-dependent Schrödinger equation with periodic driving. The dynamics of the quantum walk can be understood through the effective Hamiltonian $H_{\text{eff}}(\theta_1, \theta_2)$, defined through $U(\theta_1, \theta_2){=}e^{-iH_{\text{eff}}(\theta_1,\theta_2)\tau/\hbar}$, where τ is the time required for one step of the quantum walk. Throughout this paper, we chose units such that $\tau/\hbar = 1$. Therefore, the quantum walk described by the evolution $U(\theta_1, \theta_2)$ corresponds to a stroboscopic simulation of the effective Hamiltonian $H_{\text{eff}}(\theta_1, \theta_2)$ viewed at unit time intervals. That is, after n steps of the quantum walk, the photon evolves according to $U^n(\theta_1, \theta_2){=}e^{-inH_{\text{eff}}(\theta_1,\theta_2)}$, meaning that the evolution under the quantum walk coincides with the evolution under $H_{\text{eff}}(\theta_1, \theta_2)$ for integer multiples of τ.

The topological structure underlying split-step quantum walks is revealed by studying the structure and symmetry of $H_{\text{eff}}(\theta_1, \theta_2)$. $H_{\text{eff}}(\theta_1, \theta_2)$ has a gapped spectrum, with two bands corresponding to opposite polarisations (Fig. 7.2a). Because the quantum walk is translationally invariant, each eigenstate is associated with a quasi-momentum k and a superposition of $|H\rangle$ and $|V\rangle$. In addition, this class of quantum walks has a chiral symmetry described in ref. [25] (also detailed in the Methods), which requires that the polarisation component of any eigenstate be confined to a particular great circle on the Bloch sphere. Therefore, as the quasi-momentum k traverses the first Brillouin zone from $-\pi$ to π, the polarisation component of the eigenstate traces a closed path confined to that great circle, see Fig. 7.2b and Methods. The total number of times W that this closed path winds about the origin is the winding number and gives the topological invariant of $H_{\text{eff}}(\theta_1, \theta_2)$.

Because W has to be an integer, it cannot be changed by small modifications of the effective Hamiltonian. That is, W can only change when the spectrum of $H_{\text{eff}}(\theta_1, \theta_2)$ closes its gap while preserving chiral symmetry. For the split-step quantum walk, two distinct topological phases with $W{=}0$ and $W{=}1$ exist as can be seen in the phase diagram shown in Fig. 7.2c. The two phases are separated by lines along which the gap closes.

As we mentioned above, non-trivial topological phases support localised states at their boundaries. Because our experimental setup allows access to individual lattice sites, we can probe this phenomenon by creating a boundary between regions where the dynamics are governed by two different gapped Hamiltonians $H_{\text{eff}}(\theta_{1-}, \theta_2)$ and $H_{\text{eff}}(\theta_{1+}, \theta_2)$, characterised by winding numbers W_- and W_+ respectively. We create the boundary by making θ_1 spatially inhomogeneous with $\theta_1(x){=}\theta_{1-}$ for lattice positions $x{\leq}0$ and $\theta_1(x){=}\theta_{1+}$ for $x{>}0$. Although this breaks translational symmetry, the chiral symmetry remains (see Methods). When $W_-{\neq}W_+$, it is expected that topologically robust localised states exist at the boundary near $x{=}0$. This can be understood in a heuristic fashion as follows. When $W_-{\neq}W_+$, the winding number W_- of the bulk gapped Hamiltonian $H_{\text{eff}}(\theta_{1-}, \theta_2)$ can only be changed to that of $H_{\text{eff}}(\theta_{1+}, \theta_2)$ given by W_+ by closing the gap of the system. Thus, near the boundary between these two regions, the energy gap closes, and it is expected that states exist within the gaps of the bulk spectra of $H_{\text{eff}}(\theta_{1-}, \theta_2)$ and $H_{\text{eff}}(\theta_{1+}, \theta_2)$. Because extended states do not exist inside the gap, such a state is necessarily localised at the boundary. That is, a change in topology at a boundary is accompanied by the presence of a localised state. Furthermore, we are able to show that the localised states are robust against perturbations[26] such as small changes of quantum walk parameters or the presence of a static disordered potential caused by, for example, small spatial variations of rotation angles θ_1 and θ_2.

7.2.2 Experimental confirmation of bound states

To probe the existence of the bound states, we initialise a photon next to the boundary between two topologically distinct quantum walks (Fig. 7.1). In the absence of bound states, the photon is expected to spread ballistically, with the detection probability at the origin quickly decreasing to zero. However, if there is a bound state, the bound state component of the initial state will remain near this boundary even after many steps.

We first implemented split-step quantum walks with $\theta_2{=}\pi/2$ and θ_{1-} and θ_{1+} such that $W_-{=}W_+{=}1$, as shown on the phase diagram in Fig. 7.3a. For initial photon polarisations of $|H\rangle$ and $|V\rangle$, shown in Fig. 7.3b,c respectively, the detection probability at the origin quickly decreases to zero. On the other hand, in Fig. 7.3d, with parameters chosen to create a boundary between topologically distinct phases $W_-{=}0$ and $W_+{=}1$, we observe the existence of at least one bound state as a peak in the probability distribution near the origin after four steps.

We note that our experiment is able to detect bound states with fewer steps than the theoretical study in ref. [25], because we use a sharper boundary between distinct topological

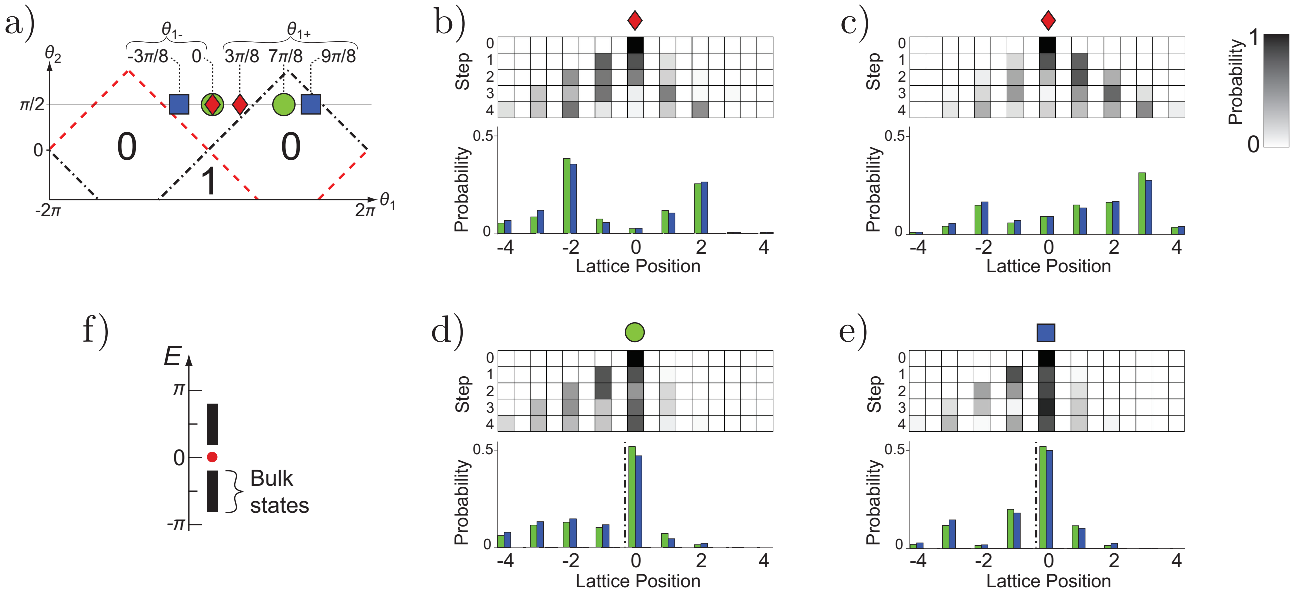

Figure 7.3: Experimental quantum walks with topologically protected bound states. a) Phase diagram, with symbols indicating the parameters (θ_{1-}, θ_{1+}, θ_2), and the corresponding winding numbers for each experimental case b-e. b)-e) Experimental probability distributions of split-step quantum walks for $\theta_2{=}\pi/2$ and a spatially inhomogeneous rotation $R(\theta_1)$. The probabilities of finding the photon at a particular site are indicated by the shading in the upper panel. The bar graphs below each dataset compare the measured (blue) and predicted (green) probabilities after the fourth step. Experimental errors due to photon counting statistics are not visible on this scale. b) and c) show the absence of a bound state near $x{=}0$ for initial polarisations $|H\rangle$ and $|V\rangle$ respectively. d) Initial polarisation of $|H\rangle$, the presence of a bound state with a pronounced peak near $x{=}0$ after the fourth step. The phase boundary is indicated on the bar plot by the dash-dotted black line. e) Initial polarisation of $|H\rangle$, the presence of the bound state is robust against changes to the parameters in d). f) Calculated quasi-energy spectrum of the effective Hamiltonian for d. The bound state with quasi-energy $E{=}0$ is indicated by the red dot.

phases. As a result, the bound states become narrower and are more easily detected.

We can test the robustness of these bound states against a variety of changes in microscopic parameters to confirm that they are topologically protected. In Fig. 7.3e, θ_{1-} and θ_{1+} are shifted from those of Fig. 7.3d while maintaining W_{-}=0 and W_{+}=1, and we confirmed the continued existence of a bound state. The quasi-energy E of this localised state, that is, the eigenvalue of the effective Hamiltonian associated with this state, can be found by explicit calculation (Fig. 7.3f). We indeed find a single state at $E = 0$.

7.2.3 Observation of pairs of bound states in quantum walks

Our experiment also reveals a new topological phenomenon unique to periodically driven systems, which can be probed by studying split-step quantum walks with θ_2=0, and the θ_1 parameters shown in Fig. 7.4a. With the appropriate choice of basis (see Methods), this quantum walk becomes equivalent to the one described by the one-step operator U=$iTR(\theta_1)$, where T=T_1T_2 can be implemented with a single calcite beam displacer, extending the experiment to seven steps. This class of quantum walks can only realise a single topological phase characterised by the winding number W=0. Therefore, we do not expect bound states for spatially inhomogeneous θ_1 based on winding numbers. However, the evolution of the probability distribution shown in Fig. 7.4b displays period-2 oscillations in the vicinity of the origin. This observation strongly suggests the existence of at least two bound states whose quasi-energies differ by π.

Again, we can demonstrate that these bound states are robust against small perturbations to the walk parameters. The parameters for Fig. 7.4c are chosen so that they are continuously connected with those for Fig. 7.4b. As expected, we observe the period-2 oscillations in the evolution of probability distributions indicating the existence of a pair of bound states whose quasi-energies differ by π.

We confirm the absence of bound states for split-step quantum walks with θ_2=0 when θ_{1-} and θ_{1+} are continuously connected without crossing a phase boundary. The results in Fig. 7.4d,e show detection probabilities that quickly decrease to zero near the boundary for initial polarisations $|H\rangle$ and $|V\rangle$, respectively. As $|H\rangle$ and $|V\rangle$ span the space of internal states for the walker, this shows that indeed there is no bound state near x=0.

The existence of a pair of bound states with quasi-energy difference π is a previously unknown topological phenomenon. It is a consequence of chiral symmetry, defined as the existence of an operator Γ that anti-commutes with the Hamiltonian, $\Gamma H \Gamma^{-1} = -H$. An eigenstate $|\psi\rangle$ with energy E therefore implies the existence of an eigenstate $\Gamma^{-1}|\psi\rangle$ with energy $-E$. That is, states with energies E and $-E$ generally come in pairs—the only exception is if $E = -E$. In a static system, a single state with energy zero can exist because its energy satisfies $E = -E$ [26]. It is topologically protected: it cannot be shifted in energy by weak, symmetry-preserving perturbations because a single state cannot be split into two. In a periodically driven system, because the effective Hamiltonian is defined through a one-step evolution operator by U=$e^{-iH_{\text{eff}}(\theta_1,\theta_2)}$, the quasi-energies of $H_{\text{eff}}(\theta_1, \theta_2)$ are defined only up to 2π. In particular, E=π and $E = -\pi$ correspond to the same quasi-energy, and therefore $E = \pi$ represents another spe-

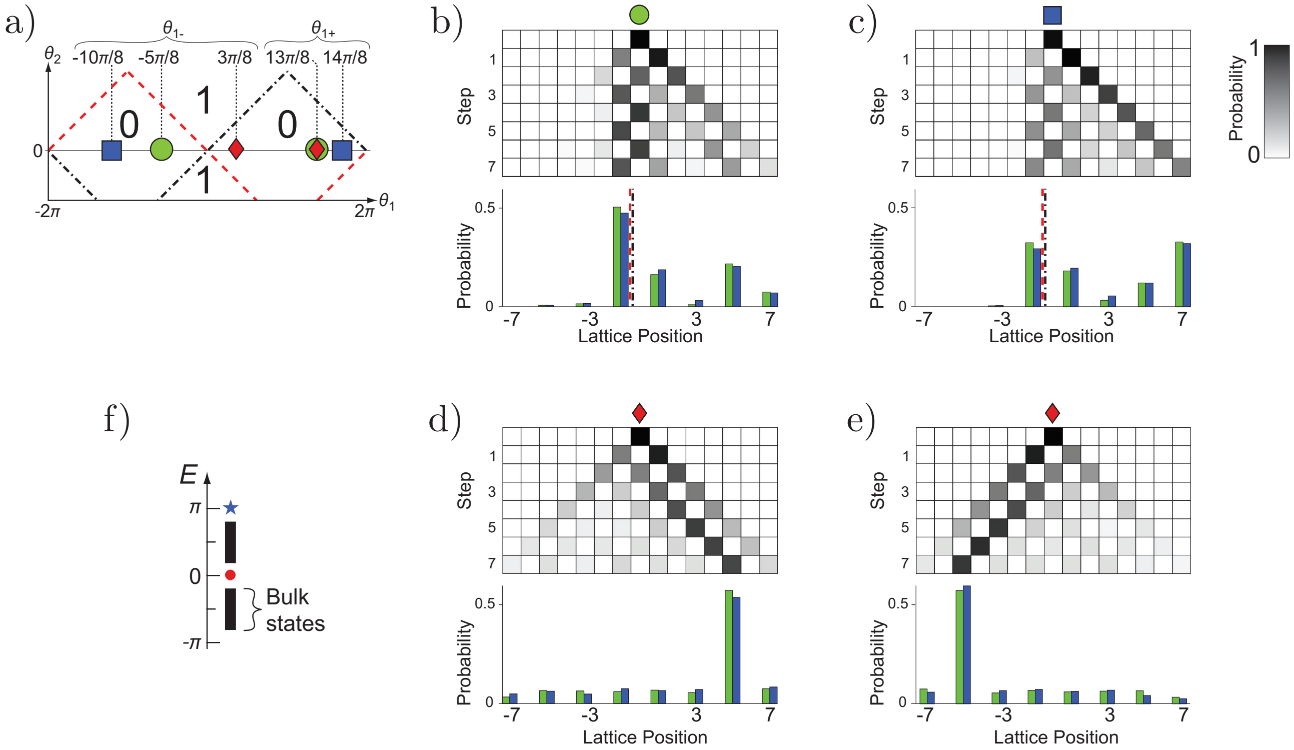

Figure 7.4: Experimental quantum walks with a pair of topologically protected bound states. a) Phase diagram, with symbols indicating the parameters (θ_{1-}, θ_{1+}, θ_2), and corresponding winding numbers for each experimental case b-e. b)-e) Experimental probability distributions of split-step quantum walks for θ_2=0 and a spatially inhomogeneous rotation $R(\theta_1)$. The probabilities of finding the photon at a particular site are indicated by the shading in the upper panel. The bar graphs below each dataset compare the measured (blue) and predicted (green) probabilities after the seventh step. Experimental errors due to photon counting statistics are not visible on this scale. b) Initial polarisation $|H\rangle$. A pair of bound states with period-2 oscillations are present and there is a large probability of detecting the photon near the boundary after seven steps. The phase boundary is indicated on the bar plot by both the dash-dotted black and dashed red lines. b) Initial polarisation $|H\rangle$. Small perturbations made to the quantum walk parameters of b) do not change the topology and therefore the bound states remain. d) and e) show the absence of a bound state near x=0 for initial polarisations $|H\rangle$ and $|V\rangle$, respectively. f) Quasi-energy spectrum of the effective Hamiltonian for b). In addition to the E=0 (red dot) bound state there is an E=π bound state (blue star).

cial value of quasi-energy satisfying $E{=}-E$. Thus, like zero-energy states of static systems, a single state with quasi-energy π is topologically protected [17, 18]. The coexistence of $E{=}0$ and $E{=}\pi$ states suggested by the period-2 oscillations observed in Fig. 7.4b, is verified through the explicit calculation of the quasi-energy spectrum presented in Fig. 7.4f. In the Methods section, we give the characterisation of this structure in terms of topological invariants of periodically driven systems and prove their topological robustness.

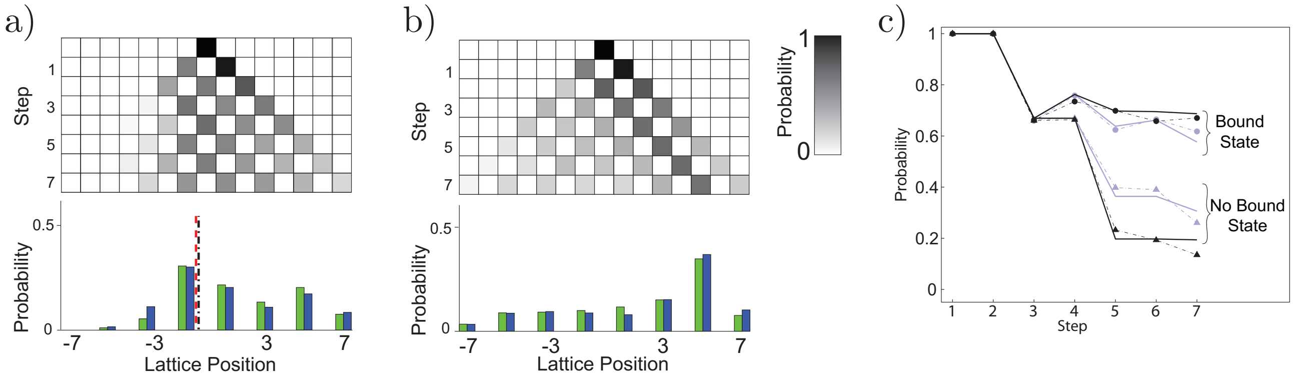

Figure 7.5: Paired bound states in the presence of decoherence. a), b) Probability distributions for split-step quantum walks with additional decoherence, q=0.2, for the initial polarisation state $|H\rangle$. The probabilities of finding the photon at a particular site are indicated by the shading in the upper panel and the bar graphs below each dataset compare the measured (blue) and predicted (green) probabilities after the seventh step. Experimental errors due to photon counting statistics are not visible on this scale. For these walks θ_2=0 and $R(\theta_1)$ is spatially inhomogeneous. a) A pair of bound states is observed between two distinct topological phases despite the added decoherence. The phase boundary is indicated on the bar plot by both the dash-dotted black and dashed red lines. b) Absence of bound states in the presence of decoherence. c) Sum of probabilities at lattice positions around the boundary (-1, 0 and $+1$) for integer steps of the split-step quantum walks with and without bound states. The solid lines show theoretical predictions and the dashed lines are the experimental results, error bars are smaller than the marker size. The difference between bound and unbound states can be seen for both datasets, with no added decoherence (black), and with added decoherence (blue).

7.2.4 Bound states under decoherence

One feature of our optical quantum walk setup is the ability to tune the level of decoherence [24]. Each pair of beam displacers forms an interferometer, which can be intentionally misaligned to add temporal and spatial walk-off [24]. This process, coupled with measurement of the photon, corresponds well to pure dephasing [24]. If the system at step N is described by the density matrix ρ_N it will evolve according to:

$$\rho_{N+1} = (1-q)U\rho_N U^\dagger + q\sum_i K_i U\rho_N U^\dagger K_i^\dagger \tag{7.1}$$

where q is the amount of dephasing and K_i are the associated Kraus operators. For q=0, Eq. 7.1 describes a pure quantum walk, while q=1 represents a system without any quantum coherence, that is, the evolution is described by a classical random walk. Although q=0 indicates that we do not introduce deliberate dephasing, some may arise from experimental imperfections.

Although the topological bound states observed in the paper are no longer eigenstates of the quantum walk under dephasing, signatures of bound states are still observable for a small number of steps. This result demonstrates that it is possible to study topological phenomena, for short times, in other systems that might be more prone to decoherence.

In Fig. 7.5, we show split-step quantum walks with θ_1 and θ_2 parameters equivalent to those presented in Fig. 7.4b,d. However, here we have introduced additional decoherence at a level of q=0.2 according to Eq. 7.1. Figure 7.5a shows the same period-2 oscillation as before demonstrating that a pair of bound states can be seen with this small amount of decoherence. The absence of a bound state is confirmed when we chose W_{-}=W_{+}=0, and the results are shown in Fig. 7.5b.

In the presence of dephasing, the bound state observed in Fig. 7.4b gradually decays as the number of steps increases. However, for slow dephasing, this decay is slow and, for few steps, the probability distribution is still peaked near the boundary compared to the cases with no bound states (Fig. 7.5a,c summarises the effect of decoherence on the probability distribution around the boundary region).

7.3 Discussion

The bound states observed in Fig. 7.3d,e are direct analogues of the zero-energy states in the Su-Schrieffer-Heeger (SSH) model of polyacetylene [27] and the Jackiw-Rebbi model of a one-dimensional spinless Fermi field coupled to a Bose field [10]. Specifically, the SSH model describes conduction in conjugated organic polymers, of which polyacetylene is the simplest example. By studying this polymer from a topological perspective, they identified the formation of a ‘topological soliton’ [27] that is responsible for the charge-transfer doping mechanism in this molecule. Despite these theoretical predictions, its topological nature has never directly been confirmed. With our system, we have simulated the same class of topological phases as the SSH model and demonstrated their robustness to system perturbations for the first time.

The experiment can be extended to other symmetry classes and higher dimensions. In particular, the beam displacer architecture could also implement a two-dimensional walk [28], which would allow observation of topologically protected edge states. Furthermore, one could simulate many topological classes of static systems that have been theoretically predicted but have not yet been realised because of the lack of natural materials with suitable symmetries [25]. In addition, novel topological phenomena, unique to periodically driven systems, are expected in other symmetry classes and dimensions. The versatility of photonic quantum walks makes them ideal tools for exploring these captivating phenomena [17].

7.4 Methods

7.4.1 Rotation operators implemented in the experiment

The implementation of split-step quantum walks with a photon requires the rotations of polarisation, written as $R(\theta)$. In this experiment, we used half-wave plates which implement

$R(\theta){=}e^{-i\sigma_y\theta/2}\sigma_z$, where σ_i are the Pauli matrices such that $\sigma_z\,|H\rangle=|H\rangle$ and $\sigma_z\,|V\rangle=-\,|V\rangle$.

7.4.2 Winding numbers of split-step quantum walk

In our theoretical proposal [25], we considered creating a boundary between regions with different topological numbers by varying the second rotation angle θ_2. We described the topological structure of the split-step quantum walk in terms of the one-step evolution operator, or Floquet operator, $U(\theta_1,\theta_2){=}T_2R(\theta_2)T_1R(\theta_1)$ and associated chiral symmetry operator Γ_{θ_1}, which depends only on θ_1 and satisfies $\Gamma_{\theta_1}^{-1}U(\theta_1,\theta_2)\Gamma_{\theta_1}{=}U^{\dagger}(\theta_1,\theta_2)$. In this experiment, we implemented inhomogeneous split-step quantum walks by varying the first rotation angle, θ_1. To maintain the chiral symmetry in the system, it is necessary to characterise the dynamics in terms of an alternative chiral symmetry operator that depends only the second rotation angle, θ_2. In the following, we explain and define such a chiral symmetry operator. As a consequence of considering such a chiral symmetry operator, the present phase diagrams are slightly different from those in ref. [25].

Because the origin of time for a periodically driven system is arbitrary, we can characterise the topology of the split-step quantum walk with a different initial time, namely in terms of the evolution operator given by,

$$U'(\theta_2,\theta_1){=}T_1R(\theta_1)T_2R(\theta_2). \tag{7.2}$$

This alternative choice corresponds to making a half-period shift of the origin of time. Using the momentum-space expressions,

$$T_1{=}\sum_k e^{ik\sigma_z/2}e^{ik/2}\,|k\rangle\,\langle k| \quad \text{and} \quad T_2{=}\sum_k e^{ik\sigma_z/2}e^{-ik/2}\,|k\rangle\,\langle k|\,, \tag{7.3}$$

we see that $U'(\theta_2,\theta_1)$ is different from $U(\theta_1,\theta_2)$ only through the exchange of θ_1 and θ_2, that is, $U'(\theta_2,\theta_1){=}U(\theta_1,\theta_2)$. Therefore, it is clear that the chiral symmetry operator of $U'(\theta_2,\theta_1)$ is given by Γ_{θ_2}, and that the winding numbers of $U'(\theta_2,\theta_1)$ are the same as those of $U(\theta_1,\theta_2)$. The chiral symmetry of $U'(\theta_2,\theta_1)$ only depends on the second rotation angle θ_2, and thus the symmetry is preserved even when θ_1 is varied in space. Therefore, it is possible to construct inhomogeneous quantum walks with boundaries between topologically distinct phases, while preserving the required chiral symmetry across the entire system.

7.4.3 The split-step quantum walk with $\theta_2 = 0$

We studied the behaviour of the split-step quantum walk $U = T_2R(\theta_2)T_1R(\theta_1)$ with $\theta_2 = 0$,noting that $R(\theta{=}0){=}\sigma_z$. In the experiment, we implemented the quantum walk with Floquet operator $U_{\mathrm{ex}}{=}T_2T_1R(\theta_1)$. In this section, we show that these two quantum walks are related through a unitary transformation, and therefore represent equivalent dynamics with equivalent topological properties.

The split-step quantum walk with $\theta_2 = 0$ is described by the Floquet operator

$$U(\theta_1, 0){=}T_2\sigma_z T_1 e^{-i\sigma_y\theta_1/2}\sigma_z = T_2 T_1 e^{i\sigma_y\theta_1/2}. \tag{7.4}$$

It is simple to check that the unitary transformation $V{=}e^{-ix\pi/2}$ acts on $T{=}T_2T_1$ such that $V^{-1}TV{=}iT\sigma_z$, where x is the coordinate operator. Therefore, $U(\theta_1, 0)$ and $U_{\rm ex}$ are unitarily related through $V^{-1}U(\theta_1, 0)V{=}iTe^{-i\sigma_y\theta_1/2}\sigma_z{=}iU_{\rm ex}$. Apart from a global phase, the experimental implementation is equivalent to the split-step quantum walk with $\theta_2 = 0$.

7.4.4 Topological invariants of 0 and π energy bound states

In this section, we show that the topological classification of periodically driven systems with chiral symmetry is given by $Z \times Z$, and give explicit expressions for the topological invariants in terms of the wavefunctions of the bound states. These invariants provide another way to understand the topological protection of the 0- and π-energy bound states found in the experiment.

We consider the bound states at energy 0 because analogous arguments apply to the bound states at π. Suppose that there are N_0 degenerate bound states with energy 0, which we label $|\phi^0_{\alpha'}\rangle$ with $\alpha'{=}1, \ldots, N_0$. Because the chiral symmetry operator Γ anticommutes with the Hamiltonian, Γ^2 commutes with H. When there is no conserved quantity[29] associated with Γ^2, it is possible to choose the phase of Γ such that $\Gamma^2 = 1$. Because $\Gamma|\phi^0_{\alpha'}\rangle$ is an eigenstate of H with energy 0, we can choose the basis of zero-energy states such that they are eigenstates of Γ. We denote the zero-energy states in this basis as $|\psi^0_\alpha\rangle$ and their eigenvalues under Γ as Q^0_α. As $\Gamma^2 = 1$, Q^0_α is either $+1$ or -1.

We now show that the sum of eigenvalues, the integer $Q^0 \equiv \sum_\alpha Q^0_\alpha$, represents the topological invariant associated with zero-energy bound states. The invariant Q^π for π-energy bound states is constructed in an analogous fashion, $Q^\pi = \sum_\alpha \langle\psi^\pi_\alpha|\Gamma|\psi^\pi_\alpha\rangle$, where $|\psi^\pi_\alpha\rangle$ are the π-energy bound states. To show that these quantities are indeed topological invariants, we show that perturbations to the Hamiltonian that preserve the chiral symmetry cannot mix the zero- and π-energy bound states with the same eigenvalues of Γ, and therefore cannot change the energies of these states away from 0 or π. Let H' be a perturbation to the system such that $\{\Gamma, H'\} = 0$. Now we evaluate the matrix element of $\{\Gamma, H'\} = 0$ between the 0 (π) energy states. The result is

$$\begin{aligned} 0 &= \langle\psi^0_\alpha|\{\Gamma, H'\}|\psi^0_\beta\rangle \\ &= \begin{cases} 2Q_\alpha\langle\psi^0_\alpha|H'|\psi^0_\beta\rangle & \text{for } Q_\alpha = Q_\beta \\ Q_\alpha\langle\psi^0_\alpha|H'|\psi^0_\beta\rangle - Q_\alpha\langle\psi^0_\alpha|H'|\psi^0_\beta\rangle = 0 & \text{for } Q_\alpha = -Q_\beta. \end{cases} \end{aligned} \tag{7.5}$$

Thus, bound states with the same eigenvalues Q_α cannot mix, while those with different eigenvalues in general do mix and are not protected by chiral symmetry. Because one can break up any finite change of the Hamiltonian into successive changes of small perturbations, one can repeat this argument and show that the values Q^0 and Q^π cannot change unless the bound states at 0 and π energies mix with the bulk states.

In the limiting case of the split-step quantum with $\theta_2{=}0, \theta_{1-}{=}-\pi, \theta_1{=}\pi$, we can analyse the bound states of the shifted evolution operator,

$$U'(\theta_2, \theta_1){=}T_1 R(\theta_1) T_2, \tag{7.6}$$

with chiral operator $\Gamma_{\theta_2}{=}\sigma_x$. The bound-state wavefunctions can be easily computed and one finds a single zero-energy bound state with $Q^0 = 1$ and a single π-energy bound state with $Q^\pi{=}-1$. Because the pair of bound states found in the experiment arises in a situation that is continuously connected with this limiting split-step quantum walk without closing the gaps, the observed pair is characterised by the same values of the topological invariants.

7.5 Additional experimental details

In this section we present supplementary data that was not published in the original manuscript due to journal length restrictions.

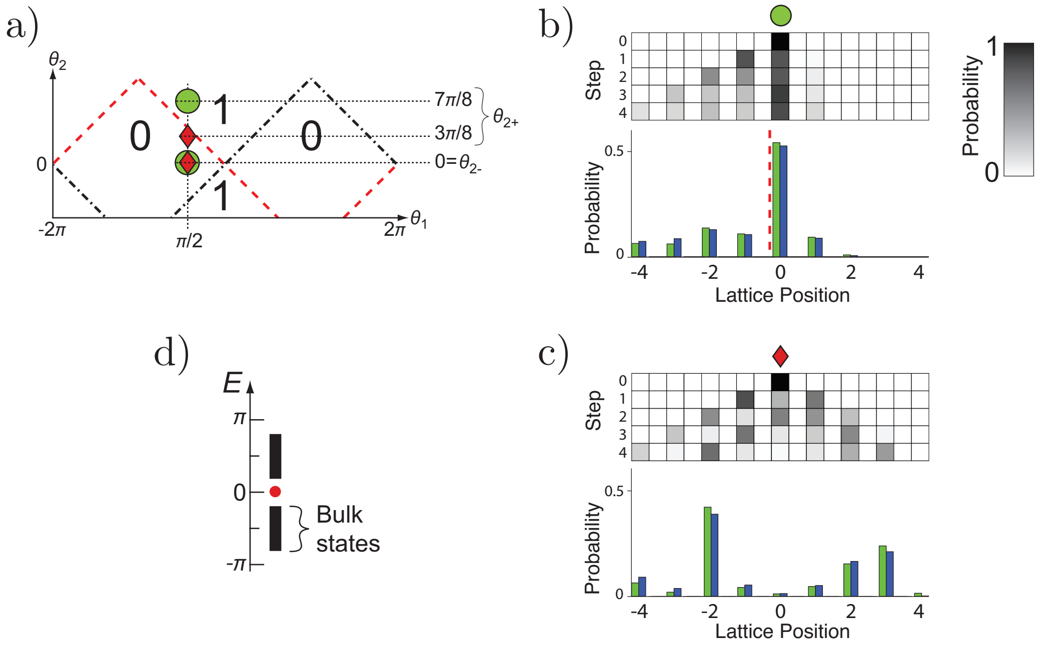

Figure 7.6: Experimental split-step quantum walks with inhomogeneous θ_2. a) Phase diagram, with symbols indicating the parameters (θ_1, θ_{2-}, θ_{2+}), and corresponding winding numbers for the experimental cases b and c. b) and c) Experimental probability distributions of split-step quantum walks for $\theta_1{=}\pi/2$ and a spatially inhomogeneous rotation $R(\theta_2)$. The probabilities of finding the photon at a particular site are indicated by the shading in the upper panel. The bar graphs below each dataset compare the measured (blue) and predicted (green) probabilities after the fourth step. Experimental errors due to photon counting statistics are not visible on this scale. b) Initial polarisation $|H\rangle$. A bound states is present as there is a large probability of detecting the photon near the boundary after four steps. The phase boundary is indicated on the bar plot by both the dashed red line. c) Shows the absence of a bound state near $x{=}0$ for the initial polarisation state $|H\rangle$. d) Calculated quasi-energy spectrum of the effective Hamiltonian for b. The bound state with quasi-energy $E{=}0$ is indicated by the red dot.

7.5.1 Split-step quantum walks for inhomogeneous θ_2

In the main text we discuss split-step quantum walks with an inhomogeneous rotation $R(\theta_1)$ across the walk lattice. Here we present results with an inhomogeneous rotation $R(\theta_2)$ and show that the presence or absence of bound states persists as a result of the topological nature of the quantum walk. The results are shown in Fig. 7.6. These results add weight to the argument that indeed the presence or absence of bound states in split-step quantum walks is a purely topological effect.

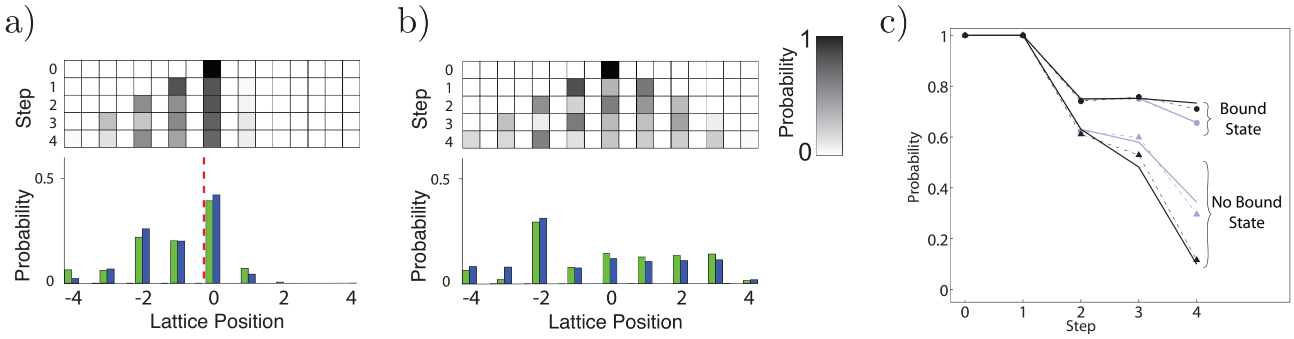

Figure 7.7: Bound states in the presence of decoherence, for walks with $\theta_1 = \pi/2$ and $R(\theta_2)$ is spatially inhomogeneous. a), b) Probability distributions for split-step quantum walks with additional decoherence, q=0.2, for the initial polarisation state $|H\rangle$ and the same parameters as shown in Fig. 7.6b and c. The probabilities of finding the photon at a particular site are indicated by the shading in the upper panel and the bar graphs below each dataset compare the measured (blue) and predicted (green) probabilities after the fourth step. Experimental errors due to photon counting statistics are not visible on this scale. (a) A bound state is observed between two distinct topological phases despite the added decoherence. The phase boundary is indicated on the bar plot by both the dashed red. (b) Absence of a bound state in the presence of decoherence. (c) Sum of probabilities at lattice positions around the boundary (-1, 0 and $+1$) for integer steps of the split-step quantum walks with and without bound states. The solid lines show theoretical predictions and the dashed lines are the experimental results, error bars are smaller than the marker size. The difference between bound and unbound states can be seen for both datasets, with no added decoherence (black), and with added decoherence (blue).

7.5.2 Additional data for bound states under decoherence

In the main text we only presented decoherence data for split-step quantum walks with θ_2=0 and an inhomogeneous $R(\theta_1)$. In Fig. 7.7 we present the split-step quantum walks that are subject to additional decoherence with θ_1=$\pi/2$ and an inhomogenous $R(\theta_2)$. The results show a clear signature of the bound state despite the presence of decoherence. Finally, in Fig. 7.8 we show split-step quantum walks under more decoherence than was implemented in the main text. The results still show a clear difference in the walker population near the phase boundary, between quantum walks with and without bound states. Again, these results demonstrate that the signature of a topological bound state is not restricted to experiments that are minimally affected by decoherence.

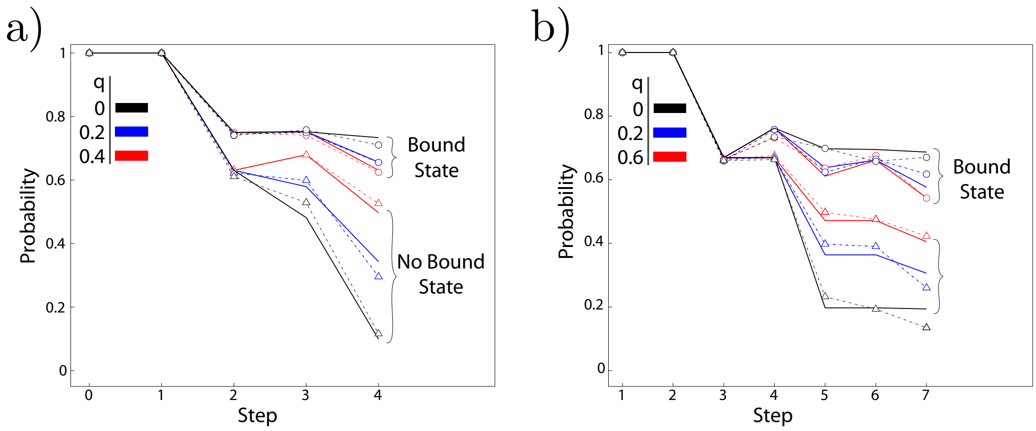

Figure 7.8: Summed probabilities for lattice positions −1, 0 and +1 for integer steps of the split-step quantum walk with additional decoherence indicated on the graphs. The difference between bound and unbound states can be seen despite the introduction of decoherence into the system. The amount of decoherence is given by the q parameter, as defined in Eq. 7.1. a) Split-step quantum walks with θ_1=$\pi/2$ and an inhomogeneous $R(\theta_2)$ (see Fig. 7.6 for data without additional decoherence) and b) split-step quantum walks with θ_2=0 and an inhomogeneous $R(\theta_1)$ (see Fig. 7.4 for data without additional decoherence). In both a) and b) there is a phase boundary at x=0, therefore one expects to observe a bound state neatr this boundary. The solid lines are theoretical predictions and the dashed lines are experimental results. Error bars are smaller than the marker size.

References

[1] Landau, L. D. Zur Theorie der Phasenumwandlungen. *Phys. Z. Sowjetunion* **11**, 26–27 (1937).

[2] Chen, Y. L. *et al.* Experimental realization of a three-dimensional topological insulator, Bi2Te3. *Science* **325**, 178–81 (2009).

[3] Xia, Y. *et al.* Observation of a large-gap topological-insulator class with a single Dirac cone on the surface. *Nature Physics* **5**, 398–402 (2009).

[4] Nayak, C., Simon, S. H., Stern, A., Freedman, M. & Das Sarma, S. Non-Abelian anyons and topological quantum computation. *Rev. Mod. Phys.* **80**, 1083–1159 (2008).

[5] Fu, L. & Kane, C. L. Superconducting proximity effect and Majorana fermions at the surface of a topological insulator. *Phys. Rev. Lett.* **100**, 096407 (2008).

[6] Alicea, J., Oreg, Y., Refael, G., von Oppen, F. & Fisher, M. P. A. Non-Abelian statistics and topological quantum information processing in 1D wire networks. *Nature Physics* **7**, 412–417 (2011).

[7] Wray, L. A. *et al.* Observation of topological order in a superconducting doped topological insulator. *Nature Physics* **6**, 855–859 (2010).

[8] Hasan, M. Z. & Kane, C. L. Colloquium: Topological insulators. *Rev. Mod. Phys.* **82**, 3045–3067 (2010).

[9] Qi, X. L. & Zhang, S. C. Topological insulators and superconductors. *Rev. Mod. Phys.* **83**, 1057–1110 (2011).

[10] Jackiw, R. & Rebbi, C. Solitons with fermion number $\frac{1}{2}$. *Phys. Rev. D* **13**, 3398–3409 (1976).

[11] Wang, Z., Chong, Y., Joannopoulos, J. D. & Soljačić, M. Observation of unidirectional backscattering-immune topological electromagnetic states. *Nature* **461**, 772–775 (2009).

[12] Sørensen, A. S., Demler, E. & Lukin, M. D. Fractional quantum Hall states of atoms in optical lattices. *Phys. Rev. Lett.* **94**, 086803 (2005).

[13] Zhu, S.-L., Fu, H., Wu, C.-J., Zhang, S.-C. & Duan, L.-M. Spin hall effects for cold atoms in a light-induced gauge potential. *Phys. Rev. Lett.* **97**, 240401 (2006).

[14] Jaksch, D. & Zoller, P. Creation of effective magnetic fields in optical lattices: the Hofstadter butterfly for cold neutral atoms. *New Journal of Physics* **5**, 56 (2003).

[15] Osterloh, K., Baig, M., Santos, L., Zoller, P. & Lewenstein, M. Cold atoms in non-Abelian gauge potentials: From the Hofstadter "moth" to lattice gauge theory. *Phys. Rev. Lett.* **95**, 010403 (2005).

[16] Aharonov, Y., Davidovich, L. & Zagury, N. Quantum random walks. *Phys. Rev. A* **48**, 1687 (1993).

[17] Kitagawa, T., Berg, E., Rudner, M. & Demler, E. Topological characterization of periodically driven quantum systems. *Phys. Rev. B* **82**, 235114 (2010).

[18] Jiang, L. *et al.* Majorana fermions in equilibrium and in driven cold-atom quantum wires. *Phys. Rev. Lett.* **106**, 220402 (2011).

[19] Lindner, N. H., Refael, G. & Galitski, V. Floquet topological insulator in semiconductor quantum wells. *Nature Physics* **7**, 490–495 (2011).

[20] Karski, M. *et al.* Quantum walk in position space with single optically trapped atoms. *Science* **325**, 174–177 (2009).

[21] Zähringer, F. *et al.* Realization of a quantum walk with one and two trapped ions. *Phys. Rev. Lett.* **104**, 100503 (2010).

[22] Schmitz, H. *et al.* Quantum walk of a trapped ion in phase space. *Phys. Rev. Lett.* **103**, 090504 (2009).

[23] Schreiber, A. *et al.* Photons walking the line: A quantum walk with adjustable coin operations. *Phys. Rev. Lett.* **104**, 050502 (2010).

[24] Broome, M. A. *et al.* Discrete single-photon quantum walks with tunable decoherence. *Phys. Rev. Lett.* **104**, 153602 (2010).

[25] Kitagawa, T., Rudner, M. S., Berg, E. & Demler, E. Exploring topological phases with quantum walks. *Phys. Rev. A* **82**, 033429 (2010).

[26] Ryu, S. & Hatsugai, Y. Topological origin of zero-energy edge states in particle-hole symmetric systems. *Phys. Rev. Lett.* **89**, 077002 (2002).

[27] Su, W. P., Schrieffer, J. R. & Heeger, A. J. Solitons in polyacetylene. *Phys. Rev. Lett.* **42**, 1698–1701 (1979).

[28] Di Franco, C., Mc Gettrick, M. & Busch, T. Mimicking the probability distribution of a two-dimensional Grover walk with a single-qubit coin. *Phys. Rev. Lett.* **106**, 080502 (2011).

[29] Ryu, S., Schnyder, A. P., Furusaki, A. & Ludwig, A. W. W. Topological insulators and superconductors: tenfold way and dimensional hierarchy. *New Journal of Physics* **12**, 065010 (2010).

CHAPTER 8

Two-photon quantum walks in an elliptical direct-write waveguide array

Published: *New Journal of Physics* **13**, (2011)

J. O. Owens[1], M. A. Broome[1], D. N. Biggerstaff[1], M. E. Goggin[1,2], A. Fedrizzi[1],
T. Linjordet[3], M. Ams[4], G. D. Marshall[4], J. Twamley[3], M. J. Withford[4] and A. G. White[1]

[1]ARC Centre for Engineered Quantum Systems, ARC Centre for Quantum Computer and Communication Technology, School of Mathematics and Physics, University of Queensland, 4072 Brisbane, QLD, Australia
[2]Department of Physics, Truman State University, Kirksville, Missouri 63501, USA
[3]ARC Centre for Engineered Quantum Systems, Department of Physics and Astronomy, Macquarie University, North Ryde NSW 2109, Australia
[4]ARC Centre for Ultrahigh bandwidth Devices for Optical Systems, Centre for Quantum Science and Technology, MQ Photonics Research Centre, Department of Physics and Astronomy, Macquarie University, North Ryde NSW 2109, Australia

Abstract

Integrated optics provides an ideal testbed for the emulation of quantum systems via continuous-time quantum walks. Here we study the evolution of two-photon states in an elliptic array of waveguides. We characterise the photonic chip via coherent-light tomography and use the results to predict distinct differences between temporally indistinguishable and distinguishable two-photon inputs which we then compare with experimental observations. Our work highlights the feasibility for emulation of coherent quantum phenomena in three-dimensional waveguide structures.

8.1 Introduction

COMPUTER modeling of complex systems has contributed greatly to modern science due to sophisticated approximation methods and steadily increasing computational power. However, classical simulation methods are ultimately impractical for modeling even moderately-sized quantum systems due to an exponentially-increasing parameter space. As first proposed by Feynman[1], a possible solution is for the model itself to operate via quantum instead of classical dynamics, either through *simulation*, in which a digital model on a quantum computer yields physical quantities as in e.g. [2, 3], or through *emulation*, in which a quantum system is modeled by a better-controllable system with a sufficiently similar Hamiltonian [4].

Quantum walks [5, 6]—an extension of the classical random walk into the quantum world—provide an ideal framework for emulation due to their rich dynamics [7, 8, 9]. There are two limiting cases, discrete and continuous. In discrete-time quantum walks, one or more (interacting) quantum particles (the so-called quantum coin) evolve on a graph, with their evolution governed by their internal quantum (coin) states. The discrete-time quantum walk on a line is the best studied example of such a walk and it has been demonstrated in a number of physical systems [10, 11, 12, 13, 14].

In continuous-time quantum walks, in contrast, there are no coin operations and the evolution is defined entirely in position space [15]. These walks require a well-controlled, continuous coupling between vertices, or lattice sites. Integrated optics is perfectly suited for this task and lithographically written, evanescently coupled surface waveguides were the first system used to demonstrate a quantum walk on a line with coherent light [16]. Unfortunately, surface waveguides can only realise simple, one-dimensional graphs with limited interconnectivity.

Physically more interesting three-dimensional structures can be engineered in laser written optical waveguide arrays in dielectric materials such as fused silica [17, 18], a platform that has been shown to have suitable fidelity for photonic quantum information processing [19]. The two-dimensional graphs that can be realised with this technique allow the study of new quantum walk phenomena, such as wave communication [20], cooperative quantum games [21] and the creation of topological phases in two dimensions [22]. Examples of direct-write waveguide array structures relevant for these problems include rings, hexagonal lattices, X-shapes and triangular shapes [23, 24, 25]. To date, however, these have only been explored with classical light inputs, and specifically in the context of 2D quantum walks in [25]. True quantum effects, and genuine efficiency improvements in emulating quantum systems, will only emerge for non-classical input states as pointed out (for discrete-time walks) in [26]. The first such walk in the continuous regime was recently demonstrated in a linear waveguide array with two-photon inputs in [27].

Here, we study multi-walker continuous-time 2D quantum walks in an optical chip containing an elliptical arrangement of coupled direct-write waveguides. We characterise the optical chip via coherent light tomography, effectively realising single particle walks, and use the results to predict correlations for non-classical two-photon walks which we compare with experimental observations. Our work is an important step towards the emulation of quantum systems in three-dimensional integrated photonic architectures.

8.2 Device description

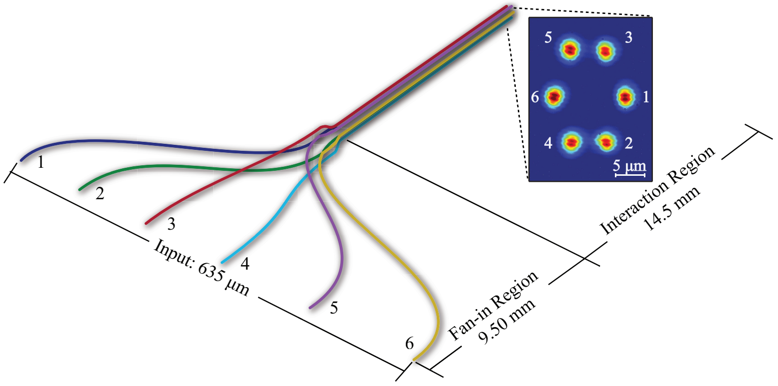

Figure 8.1: Schematic of the integrated waveguide circuit (drawing not-to-scale) and associated output. At the input the waveguides are equally spaced by $127 \mu m$. They then converge via a two-stage fan-in to their eventual elliptical configuration. The inset is a CCD image of the output: the waveguides are arranged with equal angular spacing around an ellipse with semi-major and semi-minor radii of 10.2 and 7.0 μm respectively.

The circuit for the quantum walk, shown in Fig. 8.1, consists of six waveguides written into a chip of high-purity fused silica using an ultrafast direct-write technique, described in detail in [19]. In this technique, femtosecond Ti:Sapphire laser pulses tightly focused inside the sample yield localized refractive index modifications. The sample is translated in all dimensions to create true three dimensional curved waveguides, a process that cannot be replicated by conventional lithographic techniques. Our chip was written with a 1 kHz repetition rate, 800 nm, 120 fs laser, passed through a 520 μm slit and focused with a 40x0.6 NA microscope objective. The maximum refractive index difference between the waveguides and the substrate is approximatelty $\Delta n \sim 0.0062$.

At the input, the six waveguides are arranged in a line with equal spacing of 127 μm, allowing each waveguide to be addressed individually and simultaneously. The waveguides converge via a two-stage fan-in to their final configuration as shown in Fig. 8.1. In the primary fan-in stage, which occupies the first $\sim$ 8.5 mm of the chip, the waveguides follow S-bend curves from a linear input arrangement to an elliptical configuration twice as large in radius as their final configuration. In the second fan-in stage, during the next 1 mm, further S-bends shrink this ellipse to have a semi-major axis of 10.2 μm and semi-minor axis of 7.0 μm. Studying an elliptical array provides additional insights into the coupling between waveguides as this shape breaks the degeneracy of the inter-waveguide distance. The expected inter-waveguide coupling constants are given in the appendix; notably some of the next-nearest-neighbour and even next-next-nearest-neighbour couplings are non-negligible over the interaction length in the chip. All the S-bends are of the ‘raised-sine’ form which has been shown to minimise bend loss [28], while the two-stage fan-in configuration was designed to minimise coupling (in particular, *asymmetrical* coupling) between waveguides before they attain their final interaction configuration.

The light evolution in this array is governed by the evanescent inter-waveguide coupling which drops off exponentially as a function of the waveguide distance. As an approximation, it can be theoretically described by a coupled-oscillator Hamiltonian, see Appendix.

8.3 Optical chip characterisation

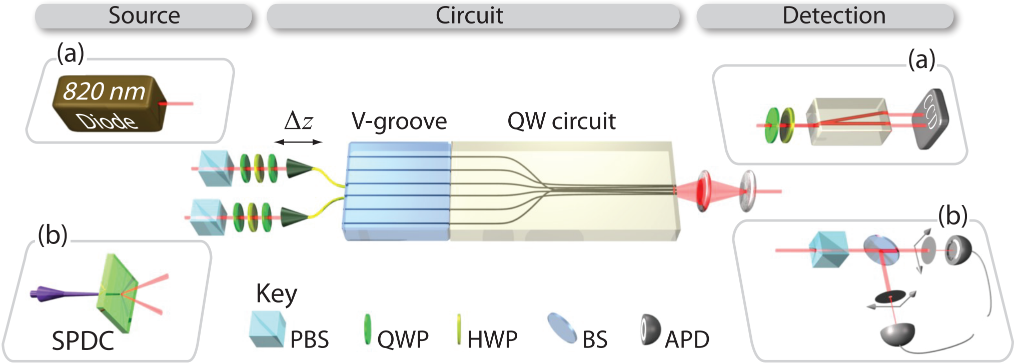

Figure 8.2: Experimental setup. The chip can be addressed with 6 individual single mode fibres. The input light polarisation is set by a combination of half- and quarter-wave plates (HWP, QWP) and polarising beamsplitters (PBS). The chip output is magnified and then collimated with two spherical lenses. a) The chip was characterised with an 820 nm laser diode, imaged onto a CCD camera via a polarising prism. b) Quantum walks were performed with two-photon inputs created via spontaneous parametric downconversion (SPDC). The relative delay Δz between the two input photons was adjusted using a translation stage. We used a 50/50 beamsplitter (BS) and two ~ 500 μm apertures to select a combination of output ports and measure the two-photon correlations in coincidence using single-photon avalanche diodes.

The experimental setup is shown in Fig. 8.2. Light was coupled into the chip via a V-groove array, which houses six single-mode optical fibres on a line, matching the input spacing of the circuit waveguides. We first illuminated individual waveguides in the chip using coherent light from an 820 nm laser diode, see Fig. 8.2a. The output intensity profiles were processed in Matlab and converted into probability distributions. When compared to the numerical simulation obtained with the software suite, used to design the chip, the predicted and observed distributions at the circuit output differed significantly, see Fig. 8.3. This behaviour prompted us to empirically determine the full optical response of the circuit using, polarisation-sensitive, coherent light tomography.

For this tomography the input polarisation was set using a bare reference fibre on top of the chip. Into each waveguide we input the following set of polarisation states:

$$\{|H\rangle, |V\rangle, |D\rangle, |A\rangle, |L\rangle, |R\rangle\}, \tag{8.1}$$

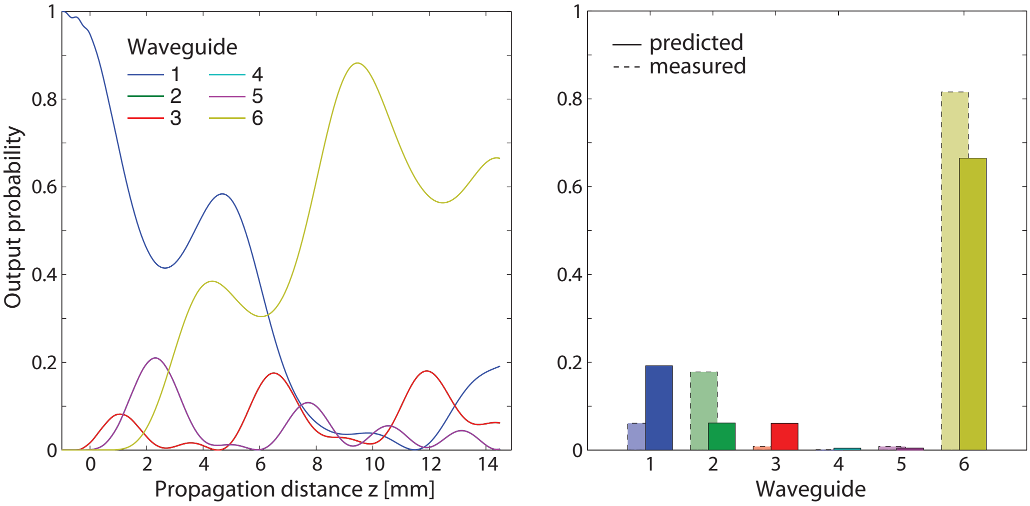

Figure 8.3: Comparison of numerical simulations and observed probability distributions for the optical chip in figure 8.1. a) The propagation dynamics predicted using optical waveguide simulation software (see Appendix) with light input into waveguide 1, as a function of z. The simulation includes modelling of inter-waveguide coupling during the 1 mm second fan-in stage at $z \leq 0$. The curves for waveguides 2 and 3, and 4 and 5 overlap due to symmetry. b) The predicted distribution at the output of the circuit, and the corresponding observed probabilities. The asymmetry in the measured distribution indicates that the optical response of the chip is not scalar, instead suggesting some vectorial behaviour. This was confirmed by further tomographic analysis.

where $|H\rangle$ and $|V\rangle$ represent horizontal and vertical polarisation and $|D/A\rangle = (|H\rangle \pm |V\rangle)/\sqrt{2}$, $|L/R\rangle = (|H\rangle \pm i\,|V\rangle)/\sqrt{2}$. For each output we measured the same six polarisation components, obtaining a total of 216 CCD images.

Using output intensity distributions taken from these images, we subsequently reconstructed an array of 36 Mueller matrices $\mathcal{M}$ [29]. This array completely characterises the optical response of the circuit, quantifying the effects of three distinct processes: notably polarisation-dependent inter-waveguide coupling, birefringence, and polarisation-dependent loss [29].

The results indicate strong birefringence in each of the six waveguides. Most notably, when the state $|H\rangle$ is input into waveguide 5, 29% of the overall output state across the six channels is rotated to $|V\rangle$. For the input channels 1, 2 and 4, the overall polarisation rotation was small, with more than 91% of $|H\rangle$ being retained at the output. Furthermore, there was significant polarisation-dependent coupling between the waveguides for all input channels. For instance, for input $|H\rangle$ into waveguide 1, 80% of the total output intensity was observed in channel 6, however when the input state was $|V\rangle$, only 11% of the total output intensity was contained in this channel. An exemplary selection of Mueller matrices, illustrated on Poincaré spheres and quantifying these effects is shown in Fig 8.4. The full matrix array $\mathcal{M}$ can be found in the Appendix.

In addition, the whole chip exhibited significant polarisation dependent loss; integrating over all output channels, we observed an excess 38% loss of $|V\rangle$ compared to $|H\rangle$ for waveguide

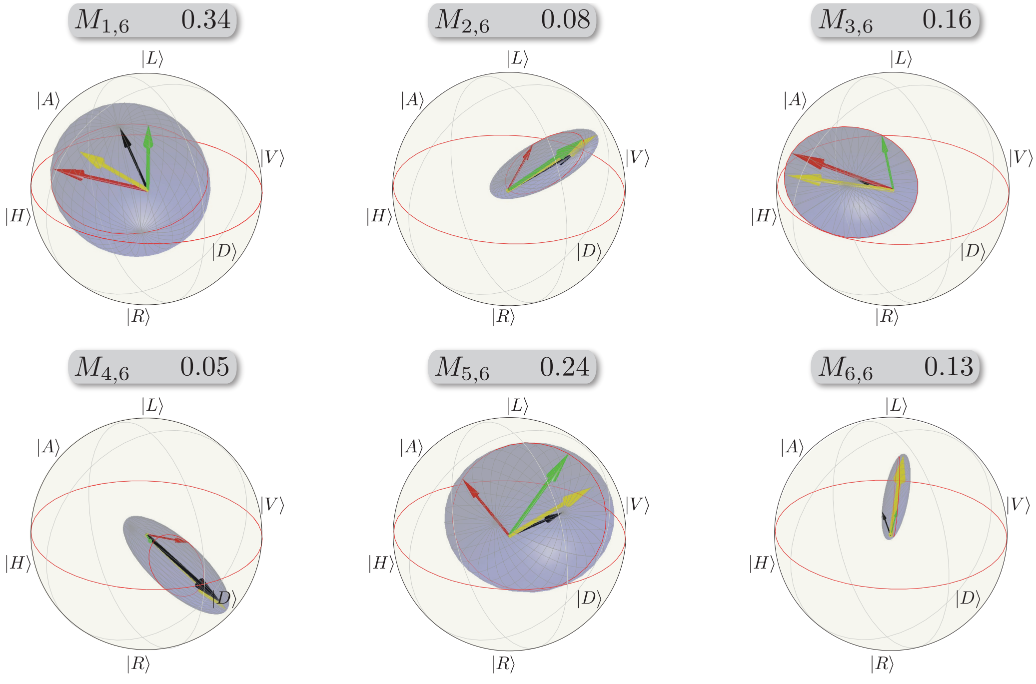

Figure 8.4: Poincaré sphere representation of the corresponding Mueller matrices, $M_{out,in}$ (see Appendix) describing the transformation from input waveguide 6 to outputs $1-6$. Input states shown on the outer Poincaré spheres are mapped to different locations on the blue ellipsoids, simultaneously showing polarisation-dependent coupling and birefringent effects in the respective channel. The relative orientation of the ellipsoids is indicated by the set of orthogonal states $|H\rangle$ (red arrow), $|D\rangle$ (green arrow) and $|L\rangle$ (black arrow), and the point of contact between sphere and ellipsoid is indicated by the yellow arrow. Note that the arrow lengths are proportional to output power, *not* degree of polarisation. The numbers above each sphere give the normalised average power coupled into the respective channel.

6. This may be due to a combination of absorption into the bulk of the circuit, or polarisation dependence of the input coupling efficiency from the V-groove array to the chip, or both.

8.4 Two-photon quantum walks

The coherent-light tomography encompasses all possible single-photon walks in this chip, since a single photon shares the coherence properties of a coherent light beam. However, these walks can be efficiently simulated classically and it is not until we input multi-photon states that we observe quantum effects [26].

A schematic of the setup for the two-photon walk experiment is shown in Fig. 8.2b. Pairs of single photons are created via spontaneous parametric down-conversion: a mode-locked 76 MHz laser centred at 820 nm is frequency doubled to 410 nm and focused into a 2 mm long β-barium borate (BBO) crystal, phase-matched for type-I downconversion. After passing through interference filters at 820 ± 2.5 nm, the degenerate photon pairs are coupled into single-mode fibres equipped with manual polarisation controllers. Photons are coupled into the chip via the V-groove fibre array.

We created photon pairs at a rate of 180 kHz, of which we detected a total of 6.5 kHz at the circuit output. The single-photon loss is thus $\sim 73\%$, factoring out the 50/50 beamsplitter, which reduces the number of coincidences by 50%. The main loss contributions stemmed from the poor input coupling efficiency between the V-groove array and the chip ($\sim$31%). The imperfect coupling is mostly due to a slight mismatch between the spacing of the fibres in the V-groove array and the locations of the input ports of the circuit. Intrinsic waveguide loss was negligible in comparison. The observed loss could be significantly reduced by using a more sophisticated imaging system.

We carried out two-photon quantum walks in two separate scenarios: with temporally distinguishable and indistinguishable photons. When the photons entering the chip are temporally distinguishable, i.e. with a time delay larger than their respective coherence times, they perform independent quantum walks with local evolution. When they enter the chip simultaneously, $\Delta z = 0$, they experience non-classical two-photon interference [30], yielding quantum dynamics, including the generation of two-photon entanglement. The theoretic qualitative difference between these two cases is described in the Appendix. Figure 8.5 shows an exemplary calibration scan of coincidence counts as a function of temporal delay. The signature of indistinguishable quantum walkers manifests as a dip in the rate of coincident detection events, C, at zero delay, with an interference visibility of $\mathcal{V} = (C_{\mathrm{max}} - C_{\mathrm{min}})/C_{\mathrm{max}}$ of $38 \pm 2\%$.

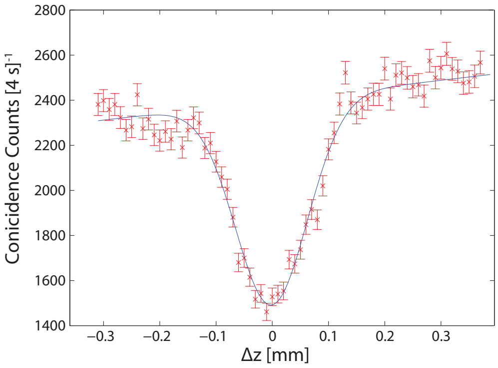

Figure 8.5: Example of observed two-photon interference between output waveguides 2 and 6 as a function of relative path difference between photon pairs input into neighbouring waveguides 1 and 2. The visibility of the dip is $\mathcal{V}_{2,6} = 38 \pm 2\%$, calculated from a Gaussian fit (blue line).

The results for two-photon quantum walks for distinguishable and indistinguishable photons input into the *nearest*-neighbour channels 1 and 2 are shown in Fig. 8.6a, as the normalised coincidence probability distributions, Γ^d and Γ^i respectively. Distinct differences are observed between the two cases, as suggested by the strong two-photon interference signature in Fig. 8.5.

The measured distributions are compared with predictions, Fig. 8.6b, which are based on determining the components of the waveguide array unitary U, for a particular input polarisation, see Appendix for details. The generalised overlap fidelities S, defined in the Appendix, between our measurements and predictions are S^d=$93.4 \pm 0.3\%$ for the distinguishable walkers, and S^i=$91.6 \pm 0.4\%$ for the indistinguishable walkers.

Figure 8.7a shows correlation matrices for inputs 2 and 4 as an example of two-photon walks

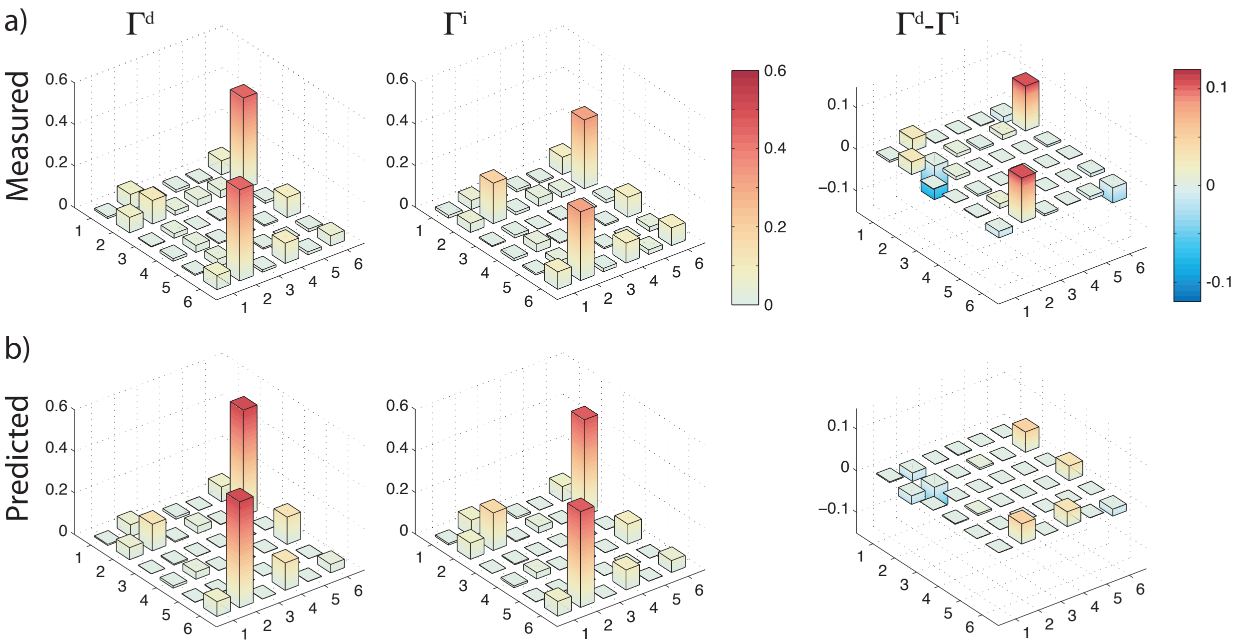

Figure 8.6: Correlation matrices for nearest-neighbour input channels 1 and 2. We recorded the photon-coincidence counts at each of the 36 pairs of output channels in a 20 second time-window. a) The measured and b) predicted correlation matrices for (left) temporally distinguishable photon pairs Γ^d, (center) temporally indistinguishable simultaneous walkers Γ^i, and (right) the difference $\Gamma^d - \Gamma^i$. The coincidence probability at the outputs 2 and 6 between the two plots reflects the two-photon interference dip shown in Fig. 8.5. The measured uncertainties are not plotted, as they are too small to be seen on the plots.

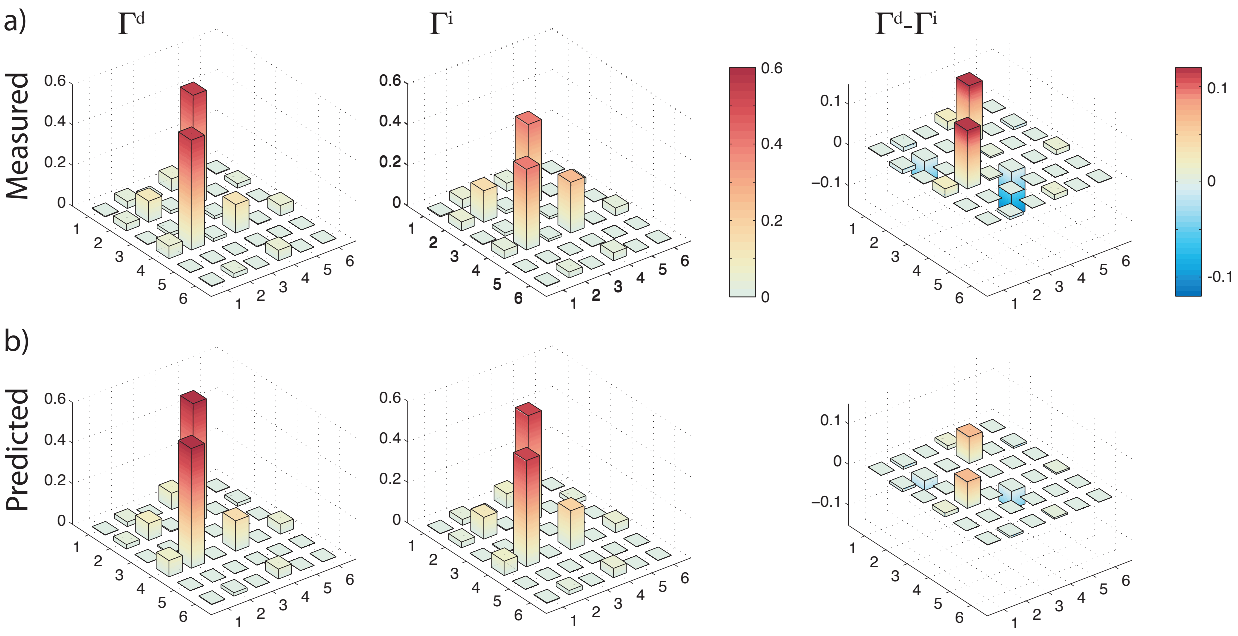

Figure 8.7: Correlation matrices for next-nearest neighbour input channels 2 and 4. The plots follow the same convention as those in Fig. 8.6, for both a) the measured and b) predicted correlation matrices. Uncertainties are again too small to be seen on the graphs.

with *next*-nearest neighbour input ports. We again observe non-classical interference signatures, with visibilities up to $\mathcal{V}_{2,4}$=28 ± 3%. The fidelities between the measured two-photon matrices and their corresponding predictions, Fig. 8.7b), are $S^d = 97.9 \pm 1\%$, and $S^i = 96.2 \pm 0.8\%$.

8.5 Discussion

In conclusion, we have performed the first quantum walk in a three-dimensional waveguide structure with genuine non-classical inputs. This is a significant step towards emulating Hamiltonians which can be approximated by evanescently coupled waveguides. However, we have also identified a number of obstacles which must be addressed before such an approach can be fully realised.

First, despite the apparent good agreement between our predictions and the observed two-photon probability distributions, the two-photon visibilities—which quantify the measured non-classical effects—matched the predictions poorly. This is because the Mueller-matrix array derived from the coherent beam intensities only yields the squared absolute values of the elements of the system's unitary U; it does not determine the (generally complex) phase relations of the waveguide array. These phase factors could in principle be obtained by phase-sensitive coherent light tomography, as proposed in [25, 31]. An alternative technique [32] requires a single N-photon input state (in this case $N = 6$) and photon-number resolved detection at each output. However, generating Fock states is hard and both techniques suffer from the large number of measurements required to fully characterise the six-port system. This is a perennial problem in quantum science: the exponential power granted by multi-photon walks on big lattices makes it hard to experimentally characterise system dynamics. A potential solution might be to use compressive sensing techniques, which have recently been exploited for exponentially efficient quantum process tomography [33].

Second, while we observed significant two-photon interference visibilities, the resulting probability distributions did not exhibit a conclusively quantum signature, as quantified by the witness defined in [16]. This was most likely due to the significant polarisation-dependent coupling and loss in the circuit, leading to non-unitary evolution which failed to preserve the coherence of the input quantum state. With a better understanding of the origins and mechanisms of these effects, they could be exploited to engineer devices such as polarisation-dependent couplers. It should be noted that these effects are certainly not inherent to the direct-write technique, as for example demonstrated by [34].

Future research should also focus on realising decoherence in continuous-time walks. Many physical, biological or chemical systems are strongly coupled to their environment and decoherence has been suggested to be the driving factor behind phenomena such as environmentally-assisted quantum transport [9]. While decoherence has been studied in discrete-time experiments [14], techniques for controllably introducing it to inherently robust waveguide lattices have yet to be demonstrated.

The emulation of classically intractable physics requires the scaling up to larger, more elaborate waveguide structures, which is certainly feasible, as demonstrated by [23, 24, 25]. However, it will be tricky to address the individual modes in these systems as the fan-in we demonstrate in our paper has its limitations. The theory will also have to catch up; unlike for quantum computation, there are no known fault-tolerance or error-correction techniques for quantum emulation in quantum walks.

Appendix

In the Heisenberg picture, a light field input into a waveguide in this chip is subject to the coupled-oscillator Hamiltonian [16]

$$H = \sum_{i=1}^{6} \beta_i a_i^\dagger a_i + \sum_{i,j=1}^{6} C_{i,j} a_i^\dagger a_j, \tag{8.2}$$

where β_i is the propagation constant in waveguide i and $C_{i,j}$ is the coupling constant between waveguides i and j. The system then evolves in time according the unitary operator $U(t) = e^{-iHt/\hbar}$ and the creation operators $a_i^\dagger$ are subject to the Heisenberg equation of motion

$$\frac{\partial a_i^\dagger}{\partial z} = \frac{n}{c}\frac{\partial a_i^\dagger}{\partial t} = i\left[H, a_i^\dagger\right] = i\beta a_i^\dagger + i\sum_{j=1}^{6} C_{i,j} a_j^\dagger, \tag{8.3}$$

which has the solution

$$a_i^\dagger(z) = \sum_j (e^{izC})_{i,j} a_j^\dagger(0) = \sum_j U_{i,j}(z) a_j^\dagger(0), \tag{8.4}$$

where $C = \{C_{i,j}\}$ is the 6×6 matrix of coupling constants with diagonal entries $C_{i,i} = \beta$, and z is the propagation distance along the waveguide array. Note that this evolution is equivalent to the continuous-time quantum walk formalism [15].

The interaction length z of the waveguides is chosen to match the desired run time t for the emulation of the Hamiltonian. The overall response of the circuit as a 12-port beam-splitting device is then contained in the unitary matrix $U = e^{izC}$, and we can define a set of six output creation operators $b_i^\dagger$, with $b_i^\dagger = a_i^\dagger(z) = \sum_j U_{i,j} a_j^\dagger$ for the input operators $a_j = a_j(0)$.

The coupling $C_{i,j}$ between two waveguides falls off exponentially with waveguide separation $r_{i,j}$ [23], so to design an array of the type discussed in this paper, the number of waveguides, their geometry, and their separations $r_{i,j}$ are chosen to reflect the properties of the Hamiltonian under investigation. This determines the parameters β_i and $C_{i,j}$. An interaction length z is chosen according to the desired emulation time t.

To translate the theoretical design into a real experimental system, the geometry of the circuit is analysed in a numerical electromagnetic design suite, in our case *RSoft* [35]. This program uses finite-difference algorithms to find solutions to Maxwell's equations in dielectrics and can be used to optimise a set of physical parameters (core diameter and refractive index contrast) which will approximate the desired evolution. This provides the link between the Hamiltonian evolution of the quantum system under study, and the physical properties of the experimental system. For our chip, simulation predicts two leading nearest-neighbour coupling strengths of $C_{24} = 0.963\ \text{mm}^{-1}$ and $C_{12} = 0.312\ \text{mm}^{-1}$, reflecting the elliptical geometry. The next-nearest neighbour and further coupling values are $C_{14} = 0.050\ \text{mm}^{-1}$, $C_{16} = 0.044\ \text{mm}^{-1}$, $C_{23} = 0.009\ \text{mm}^{-1}$, $C_{25} = 0.005\ \text{mm}^{-1}$. The latter two are negligible: our model predicts that, in the absence of the other waveguides, less than 2% of light input into one waveguide of either of these pairs would couple to the other waveguide over the interaction length of the chip. However, the next-nearest neighbour coupling C_{14} and even the next-next-nearest neighbour coupling C_{16} are notably *non*-negligible, respectively leading to modeled values of 40% and 33% coupling between these waveguide pairs, in the absence of all other waveguides, over the interaction length of the chip.

We now describe the two-photon evolution in the optical system. Two temporally indistinguishable input photons $|\Psi\rangle = a_i^\dagger a_j^\dagger |0\rangle$, for $i \neq j$, give the joint detection probability $\Gamma^i_{k,l}$ of finding the state $b_k^\dagger b_l^\dagger |0\rangle$ in output modes k and l [16]:

$$\Gamma^i_{k,l} = \langle b_l^\dagger b_k^\dagger b_k b_l \rangle_\Psi = \frac{1}{1+\delta_{k,l}} |U_{i,k}U_{j,l} + U_{j,k}U_{i,l}|^2. \tag{8.5}$$

The matrix $\Gamma^i = \{\Gamma^i_{k,l}\}$ then describes the two-photon probability distributions in all combinations of output modes. In contrast, two distinguishable photons will evolve independently and obey the statistics of Bernoulli trials. The corresponding output probability distribution $\Gamma^d_{k,l}$ takes the form,

$$\Gamma^d_{k,l} = \frac{1}{1+\delta_{k,l}} \left(|U_{i,k}U_{j,l}|^2 + |U_{i,l}U_{j,k}|^2 \right). \tag{8.6}$$

In the case of photons and electro-magnetic fields, $\Gamma^d_{k,l}$ represents an intensity correlation matrix $\Gamma^d_{k,l} = \langle I_k I_l \rangle$. The components $\Gamma^i_{k,l}$ and $\Gamma^d_{k,l}$ will differ by the factor $2\,\mathrm{Re}\left[(U_{i,k}U_{j,l})^*(U_{i,l}U_{j,k})\right]$, which encompasses the quantum nature of indistinguishable walkers.

To quantify the overlap fidelity between two probability distributions, we use [27],

$$S = (\sum_{k,l} \sqrt{\Gamma_{k,l}\Gamma^p_{k,l}})^2 / \sum_{k,l} \Gamma_{k,l} \sum_{k,l} \Gamma^p_{k,l}. \tag{8.7}$$

Mueller matrix

The Mueller-matrix array $\mathcal{M}$ describes the transfer properties of the circuit in terms of the Stokes parameters $\mathcal{S}$, which describe the polarisation state of an electromagnetic field [29]. The component $M_{i,j}$ is the 4×4 Mueller matrix describing the coupling from input waveguide j to output waveguide i. From the corresponding output Stokes parameter $\mathcal{S}_{i,j}$ for the input state $|H\rangle_j$, the real-valued parameter $|U_{i,j}|^2$ was calculated as the output transmission component in the $|H\rangle_i$ subspace.

Table 8.1 shows the calculated Mueller-matrix array $\mathcal{M}$ of the quantum walk circuit. The matrix not only allows us to determine the evolution matrix U in the $|H\rangle$ subspace, but also quantifies the polarisation-dependent coupling and birefringence observed in the circuit, as seen in Fig. 8.4.

$$
\{\mathcal{M}\} = \begin{bmatrix} M_{1,1} & \cdots & M_{1,6} \\ \vdots & \ddots & \vdots \\ M_{6,1} & \cdots & M_{6,6} \end{bmatrix}
$$

$$
= 10^{-2} \times
$$

$$
\left[\begin{array}{cccc@{\quad}cccc@{\quad}cccc@{\quad}cccc@{\quad}cccc@{\quad}cccc}
24.51 & -18.83 & -4.89 & -2.32 & 8.39 & 1.52 & 2.15 & 0.92 & 19.34 & -1.06 & 3.41 & -4.45 & 3.03 & -1.47 & 4.15 & 2.16 & 8.89 & 2.42 & -2.92 & -1.04 & 33.34 & 9.02 & 1.30 & -1.14 \\
-20.16 & 26.22 & 2.81 & -2.77 & 1.66 & 6.64 & 3.11 & 5.72 & 0.27 & 5.64 & -16.31 & -15.85 & 3.07 & -1.64 & 4.31 & 1.80 & 3.27 & 0.32 & -8.98 & 0.25 & 10.62 & 36.67 & -3.52 & -13.98 \\
2.42 & -3.57 & 8.18 & -19.65 & -0.35 & 3.54 & -7.40 & 0.01 & 3.63 & -18.81 & 4.39 & -11.81 & 1.49 & -0.49 & 2.46 & 1.69 & -1.63 & -8.39 & 0.23 & -3.15 & -0.45 & -12.27 & 10.14 & -33.96 \\
-7.69 & 5.84 & 21.04 & 9.23 & 0.89 & 5.15 & 2.64 & -6.68 & 5.19 & 11.15 & 16.31 & -14.00 & -0.70 & 0.86 & -0.42 & -0.72 & 2.83 & 3.86 & -1.24 & -8.62 & 6.28 & 8.66 & 34.62 & 9.51 \\[6pt]
16.20 & 4.05 & 3.97 & 2.57 & 43.89 & 21.91 & -11.33 & 3.46 & 2.69 & 2.63 & 1.37 & -0.38 & 23.82 & -11.27 & 2.26 & 1.56 & 7.13 & -5.66 & 3.46 & -2.27 & 7.89 & 0.03 & 7.76 & 4.62 \\
1.88 & 15.38 & -5.17 & -4.88 & 26.78 & 42.58 & -19.28 & 9.28 & -1.81 & -1.79 & -1.57 & -0.91 & -13.09 & 24.40 & -12.65 & -0.47 & -6.69 & 7.22 & -4.32 & 1.69 & -4.97 & -0.03 & -4.85 & -6.14 \\
3.64 & 4.86 & -2.57 & 16.12 & 4.13 & -13.57 & -38.63 & 1.57 & -1.40 & -1.46 & 1.15 & -0.54 & -5.41 & 12.05 & 17.15 & -6.03 & 1.57 & -1.14 & -0.03 & -6.36 & 3.84 & -3.29 & 4.81 & 1.30 \\
-5.42 & -7.03 & -16.81 & -2.59 & 3.99 & 9.54 & -3.60 & -40.51 & 2.44 & 2.47 & 1.25 & -1.82 & 0.02 & 4.93 & 3.60 & 21.42 & -1.27 & 2.74 & 4.66 & -0.22 & 5.71 & 2.44 & 6.35 & 2.06 \\[6pt]
7.77 & -6.72 & -1.85 & -5.82 & 0.37 & -0.32 & 0.10 & -0.11 & 43.51 & 1.17 & -13.56 & 19.12 & 5.48 & -4.18 & 2.03 & -4.22 & 27.90 & 3.29 & 11.18 & -14.72 & 16.01 & 8.96 & -4.68 & -3.37 \\
-0.55 & 1.04 & -3.43 & 0.26 & -0.07 & 0.05 & -0.14 & -0.24 & 5.88 & 40.78 & 13.23 & 19.07 & -4.83 & 4.86 & -3.51 & 3.38 & -1.40 & -19.32 & -6.63 & -3.16 & 11.26 & 13.02 & -9.70 & -8.71 \\
-6.18 & 5.17 & 1.57 & 6.45 & 0.26 & -0.29 & 0.14 & -0.25 & 5.52 & 21.04 & -38.14 & -18.28 & 2.91 & -2.95 & -2.07 & -3.76 & 10.11 & -5.61 & 21.89 & -2.05 & -4.27 & -11.34 & -0.86 & -11.26 \\
5.58 & -5.97 & -1.68 & -2.97 & -0.24 & 0.28 & 0.12 & -0.00 & -24.37 & 7.09 & 31.72 & -44.65 & -0.16 & 1.61 & 2.32 & -3.66 & 21.39 & 6.04 & 6.75 & -27.47 & 2.42 & 6.42 & 12.54 & -6.51 \\[6pt]
9.13 & -9.07 & 1.64 & 0.46 & 35.91 & -17.89 & 6.16 & 0.90 & 0.66 & -0.46 & 0.22 & 0.26 & 52.33 & 27.32 & -14.62 & 11.70 & 1.05 & -0.75 & 0.21 & 0.11 & 4.50 & -0.58 & -2.19 & 5.25 \\
-9.79 & 9.85 & -2.04 & -0.60 & -20.32 & 37.74 & -3.79 & -7.64 & -0.33 & 0.33 & -0.71 & -0.21 & 35.12 & 48.38 & -10.62 & 27.49 & -0.72 & 0.88 & -0.62 & -0.33 & -1.46 & -1.52 & 2.65 & -2.40 \\
-1.75 & 1.73 & -0.06 & 0.37 & -1.21 & 9.61 & 9.90 & 30.06 & 0.36 & -0.62 & -0.04 & -0.38 & 6.50 & -19.53 & -33.03 & 24.30 & -0.02 & -0.00 & 0.40 & -1.08 & 3.91 & -0.23 & -0.60 & 4.86 \\
2.23 & -2.25 & 0.35 & 0.38 & -5.57 & 2.85 & -32.32 & 8.80 & -0.27 & 0.29 & 0.21 & -0.60 & 11.26 & 16.57 & -30.93 & -30.44 & -0.51 & 0.80 & 0.68 & 0.30 & -1.99 & 2.33 & 2.64 & -2.59 \\[6pt]
0.81 & 0.17 & 1.37 & 1.28 & 0.02 & -0.00 & -0.00 & -0.00 & 27.88 & -1.34 & 12.54 & -12.09 & 2.38 & -2.36 & -1.46 & -0.14 & 45.71 & -0.87 & -2.85 & 18.66 & 23.42 & -3.77 & 6.29 & -0.21 \\
-0.55 & 0.15 & -1.22 & -1.06 & -0.01 & 0.00 & 0.01 & 0.00 & -1.19 & -10.62 & 13.42 & 19.06 & 2.05 & -2.07 & -0.05 & -0.55 & 11.35 & 37.49 & 0.79 & 29.00 & -5.40 & 12.39 & -13.28 & -20.14 \\
-0.58 & -0.43 & -1.09 & -1.11 & -0.02 & 0.00 & -0.00 & -0.00 & 6.81 & 21.63 & 15.27 & 0.45 & -1.33 & 1.32 & 1.62 & 0.62 & -1.24 & 9.25 & -45.50 & -11.73 & 4.17 & -22.51 & 1.89 & -12.93 \\
0.09 & 0.11 & 0.40 & -0.27 & -0.01 & 0.00 & -0.00 & 0.00 & 21.23 & -8.06 & 20.64 & -24.46 & -1.40 & 1.39 & 0.95 & -1.49 & -19.88 & 25.77 & 18.00 & -42.56 & 6.30 & 7.07 & 21.99 & -9.18 \\[6pt]
41.59 & 30.40 & -0.25 & 3.82 & 11.42 & -5.21 & 2.92 & -5.18 & 5.93 & -0.95 & -3.98 & -2.46 & 12.96 & -8.03 & 7.64 & -11.06 & 9.32 & 1.58 & -9.08 & -0.74 & 14.85 & -13.66 & -8.48 & -5.15 \\
31.67 & 42.04 & -11.93 & -4.82 & -6.88 & 11.51 & -2.00 & 4.74 & -0.29 & 5.78 & -1.68 & 0.67 & -10.87 & 8.56 & -5.01 & 10.10 & 1.39 & 4.01 & -1.05 & 6.22 & -9.80 & 8.68 & 5.70 & 6.84 \\
15.52 & 18.13 & 18.27 & 29.85 & 0.92 & 1.55 & -7.65 & -8.68 & 3.44 & -0.41 & -4.24 & -5.92 & 9.70 & -4.73 & 7.89 & -9.01 & -7.07 & -3.77 & 9.20 & 3.09 & -14.07 & 13.53 & 8.84 & 3.71 \\
-1.09 & -7.70 & -31.63 & 21.38 & 2.74 & 1.48 & 9.46 & -7.52 & -1.65 & 1.94 & 5.68 & -1.64 & 2.65 & -3.25 & 3.25 & 0.66 & 4.06 & -3.80 & -6.50 & 1.95 & 2.32 & -3.04 & 2.93 & -1.34
\end{array}\right]
$$

Table 8.1: Array $\mathcal{M}$ of 36 Mueller matrices, obtained from polarisation-sensitive, coherent-light tomography. This array fully describes the classical optical response of the waveguide array.

References

[1] Feynman, R. Simulating physics with computers. *International Journal of Theoretical Physics* **21**, 467–488 (1982).

[2] Lanyon, B. P. *et al.* Towards quantum chemistry on a quantum computer. *Nature Chemistry* **2**, 106–111 (2010).

[3] Du, J. *et al.* NMR implementation of a molecular hydrogen quantum simulation with adiabatic state preparation. *Phys. Rev. Lett.* **104**, 030502 (2010).

[4] Lloyd, S. Universal quantum simulators. *Science* **273**, 1073–1078 (1996).

[5] Aharonov, Y., Davidovich, L. & Zagury, N. Quantum random walks. *Phys. Rev. A* **48**, 1687 (1993).

[6] Kempe, J. Quantum random walks: an introductory overview. *Contemporary Physics* **44**, 307–327 (2003).

[7] Mülken, O. & Blumen, A. Continuous-time quantum walks: Models for coherent transport on complex networks. *Physics Reports* **502**, 37–87 (2011).

[8] Plenio, M. B. & Huelga, S. F. Dephasing-assisted transport: quantum networks and biomolecules. *New Journal of Physics* **10**, 113019 (2008).

[9] Mohseni, M., Rebentrost, P., Lloyd, S. & Aspuru-Guzik, A. Environment-assisted quantum walks in photosynthetic energy transfer. *J. Chem. Phys.* **129**, 174106 (2008).

[10] Karski, M. *et al.* Quantum walk in position space with single optically trapped atoms. *Science* **325**, 174–177 (2009).

[11] Zähringer, F. *et al.* Realization of a quantum walk with one and two trapped ions. *Phys. Rev. Lett.* **104**, 100503 (2010).

[12] Schmitz, H. *et al.* Quantum walk of a trapped ion in phase space. *Phys. Rev. Lett.* **103**, 090504 (2009).

[13] Schreiber, A. *et al.* Photons walking the line: A quantum walk with adjustable coin operations. *Phys. Rev. Lett.* **104**, 50502 (2010).

[14] Broome, M. A. *et al.* Discrete single-photon quantum walks with tunable decoherence. *Phys. Rev. Lett.* **104**, 153602 (2010).

[15] Farhi, E. & Gutmann, S. Quantum computation and decision trees. *Phys. Rev. A* **58**, 915–928 (1998).

[16] Bromberg, Y., Lahini, Y., Morandotti, R. & Silberberg, Y. Quantum and classical correlations in waveguide lattices. *Phys. Rev. Lett.* **102**, 253904 (2009).

[17] Davis, K. M., Miura, K., Sugimoto, N. & Hirao, K. Writing waveguides in glass with a femtosecond laser. *Optics Letters* **21**, 1729–1731 (1996).

[18] Nolte, S., Will, M., Burghoff, J. & a. Tuennermann. Femtosecond waveguide writing: a new avenue to three-dimensional integrated optics. *Applied Physics A* **77**, 109–111 (2003).

[19] Marshall, G. D. *et al.* Laser written waveguide photonic quantum circuits. *Opt. Express* **17**, 12546–12554 (2009).

[20] Hein, B. & Tanner, G. Wave communication across regular lattices. *Phys. Rev. Lett.* **103**, 260501 (2009).

[21] Bulger, D., Freckleton, J. & Twamley, J. Position-dependent and cooperative quantum Parrondo walks. *New Journal of Physics* **10**, 093014 (2008).

[22] Kitagawa, T., Rudner, M., Berg, E. & Demler, E. Exploring topological phases with quantum walks. *Phys. Rev. A* **82**, 33429 (2010).

[23] Szameit, A., Dreisow, F., Pertsch, T., Nolte, S. & Tünnermann, A. Control of directional evanescent coupling in fs laser written waveguides. *Opt. Express* **15**, 1579–1587 (2007).

[24] Szameit, A. *et al.* Hexagonal waveguide arrays written with fs-laser pulses. *Applied Physics B: Lasers and Optics* **82**, 507–512 (2006).

[25] Keil, R. *et al.* Photon correlations in two-dimensional waveguide arrays and their classical estimate. *Phys. Rev. A* **81**, 23834 (2010).

[26] Rohde, P. P., Schreiber, A., Stefanak, M., Jex, I. & Silberhorn, C. Multi-walker discrete time quantum walks on arbitrary graphs, their properties and their photonic implementation. *New Journal of Physics* **13**, 013001 (2011).

[27] Peruzzo, A. *et al.* Quantum Walks of Correlated Photons. *Science* **329**, 1500 (2010).

[28] Minford, W. J., Korotky, S. K. & Alferness, R. C. Low-loss ti:linbo$_3$ waveguide bends at $\lambda = 1.3$ μm. *IEEE Journal of Quantum Electronics* **18**, 1802–1806 (1982).

[29] Hecht, E. & Zajac, A. *Optics* (Addison-Wesley, 1974).

[30] Hong, C. K., Ou, Z. Y. & Mandel, L. Measurement of subpicosecond time intervals between two photons by interference. *Phys. Rev. Lett.* **59**, 2044–2046 (1987).

[31] Keil, R. *et al.* Classical characterization of biphoton correlation in waveguide lattices. *Phys. Rev. A* **83**, 013808 (2011).

[32] Pryde, G. J. & White, A. G. Creation of maximally entangled photon-number states using optical fiber multiports. *Phys. Rev. A* **68**, 052315 (2003).

[33] Shabani, A. *et al.* Efficient measurement of quantum dynamics via compressive sensing. *Phys. Rev. Lett.* **106**, 100401 (2011).

[34] Sansoni, L. *et al.* Polarization entangled state measurement on a chip. *Phys. Rev. Lett.* **105**, 200503 (2010).

[35] *http://www.rsoftdesign.com/* .

Conclusion and Outlook

In this thesis we present a variety of experiments linked by the use of quantum states of light to encode and control quantum information, as well as for simulating and exploring fundamental physics. In summary, we have demonstrated a technique for improving multi-photon generation and proven its effectiveness in the betterment of photonic quantum information processing. We have experimentally demonstrated a conclusive CHSH inequality for temporal quantum correlations, opening up the prospect for these correlations to become a resource in future quantum information tasks. Finally, we have studied photonic quantum walks in both the discrete- and continuous-time regime. Most importantly, we use our discrete-time quantum walk architecture as a platform for studying the exotic behaviour of topological phases, thereby demonstrating its versatility for simulating interesting physical phenomenon. We will now discuss the main results in finer detail and highlight future research opportunities in these areas.

The production of large multi-photon states is a difficult, but necessary problem to overcome for the progression of linear-optical quantum computation. Such a technology should create multiple photons at a high brightness to combat dark-count rates of single-photon detectors; produce each photon in a well defined spatio-temporal mode so they can be transported via optical fiber; and ensure photons are generated at the *same* time with equivalent spectral properties for indistinguishable interactions in a photonic quantum computer. At the time of writing this thesis there is no photon source which fulfils all of these criteria and with a competitive advantage over the current state-of-the art: spontaneous parametric downconversion (SPDC).

Although some research groups have used SPDC for experiments with photon numbers up to 8 [1], there is a fundamental flaw with this technology. Higher-order photon emissions lead to an ever increasing noise contribution for a desired photon number state. To combat this problem in Chapter 3 we demonstrated a simple method to increase the photon number purity of SPDC without decreasing source brightness using only linear optics elements and passive optical alignment. Our temporally multiplexed SPDC source has a reduced relative number of higher-order photon emissions, leading to an increased photon number purity. The knock-on effect is an increased visibility in measured non-classical interference as well as the fidelity of photonic quantum logic gates.

This technique on its own however, is limited by laser repetition rates and detector speeds. Another problem for higher photon-number experiments is the inherent dark count rates of single-photon detectors. The probability of producing n pairs of photons from SPDC goes as (pulse power)^n, therefore if each laser pulse is too low in power the detector dark-count rates can start to dominate, therefore reducing the signal-to-noise ratio of the source.

Using high efficiency ($> 98\%$), number resolving detectors based on superconducting transition edge sensors [2, 3] will alleviate the problem of higher-order events, but does not solve it due to other optical losses. Other techniques to increase photon-number purity include spatial-multiplexing with fast optical switching [4, 5]. With these methods one can improve photon number purity. In my opinion a vital question is: given a combination of the best currently available source and detector technologies can we reach photon-number purities within fault tolerant thresholds for photonic quantum computation?

In Chapter 4 we experimentally investigated quantum correlations in the temporal domain. Our work verifies the result that *all* quantum states are entangled in time, pure or mixed. This statement may first appear surprising to the reader, but upon closer inspection can be understood as a direct consequence of the effect that projective measurements have on quantum systems. A projective measurement at time t_i forces the quantum system into a particular state such that the probability distribution for a measurement made at time t_{i+1} is necessarily affected by the previous measurement choice.

This result is good news for applications employing the use of temporal entanglement: since the correlations are state independent, one need only calibrate the measurement devices precisely in order to measure strong temporal correlations and not worry about the fidelity of the quantum state itself. Temporal quantum correlations could provide a new resource for quantum information tasks, in fact, quantum communication protocols have already been proposed [6].

From a more fundamental perspective our work adds to the plethora of experiments that demonstrate a clear violation of a classical worldview based on the notions of macroscopic realism and non-invasive measurability [7]. However, as the system under investigation in our case is microscopic, the question of how these concepts extend into the truly macroscopic regime is still open. This problem was originally posed by Leggett and Garg [7], and has since been the subject of experimental investigation in [8, 9, 10], but again, only in the microscopic regime where one expects to find a violation of macroscopic realism and non-invasiveness. In our case an open question is: can the restriction of non-invasiveness be relaxed whilst still maintaining a violation of temporal Bell-type inequalities with a quantum system?

The main results in Part II of this thesis were the physical implementations of single- and multi-photon quantum walks in discrete- and continuous-time regimes respectively. Our experiments, though limited in the number of steps or lattice positions of the walker, open up a wide variety of future research directions.

In Chapter 6 we presented the first demonstration of a single-photon quantum walk in space. The main advantages of our system are the ability to tune the amount of decoherence as well as having access to every lattice position at every time step of the walk. In particular, in the context of quantum computing, it has been shown that a small amount of decoherence in the quantum walk is desirable for some quantum computing algorithms [11], and for quantum search algorithms, addressability of individual lattice sites is a prerequisite for any physical implementation [12].

At the end of this chapter we discussed the potential to implement multi-photon quantum walks with the calcite beam-displacer setup. Multi-photon quantum walks offer the opportunity to study unique entanglement dynamics [13], as well as the simulation of single-walker dynamics in higher dimensions [14]. In particular, search algorithms based quantum-walks on an n-dimensional hypercubes have speedups close to the best known quantum algorithms [15, 16].

As a tool for quantum computation, Rohde *et al.* have recently shown that the multi-photon quantum walk architecture complemented by measurement and feed-forward is formally equivalent to the Knill, Laflamme and Milburn scheme [17] for scalable and universal linear-optics quantum-computing [14]. The same authors show that quantum walks with multiple walkers without measurement feed-forward are also formally equivalent to the so-called BosonSampling problem posed by Aaronson and Arkhipov [18].

Given a known linear-optical network, that is, the unitary evolution that describes the network, and multiple indistinguishable photon inputs, determining the frequencies of coincident photon events at the output (dubbed BosonSampling) is strongly believed to be intractable using a classical computer, as the complexity of the optical network and photon numbers increase [18]. The reason being that the number of potential paths a collection of bosons can take through such a network scales exponentially with the network size. Although not universal for quantum computing, a physical demonstration of BosonSampling is of fundamental importance to the theory of computational complexity [18]. If it were the case that a real physical system could not sample the boson distribution more efficiently than a classical computer could predict it, the implications for computational complexity would be profound [18]. A full physical proof that BosonSampling is efficient, if performed in a physical architecture, would require one to sample from a number of different quantum walk evolutions. As we can address individual lattice sites in our system, changing the evolution is a matter of altering wave plate angles at different locations on the walk lattice. However, such an experiment comes with its own technicalities, least not the generation of large indistinguishable multi-photon states (see above)[1].

However, where the versatility of our quantum walk system is its superiority, scalability is its inferiority. Our method based on calcite beam displacers is limited by the unavoidable optical phase shifts introduced in each optical mode by manufacturing imperfections, as well as the physical dimensions of the beam-displacers themselves. We have demonstrated a maximum of 8 steps so far [19], compared to discrete-time quantum walks based on classical interferometry in optical fibre-loops which have demonstrated up to 28 steps on a 1D lattice [20] and 12 steps, or equivalently 169 positions, on a 2D lattice [21]. However, given the exponential drop-off in signal strength in these alternative schemes, it is difficult to see how they could find a solution for implementing multiple walkers. Other implementations of multi-photon discrete-time quantum walks have been demonstrated in laser written waveguides [22], which, given the

---

[1] During the final submission of this thesis the author published *"Experimental BosonSampling in a tunable circuit"*, Accepted to *Science*, e-print *arXiv:1212.2234* (2012)

inherent stability of these systems, could be a more appropriate choice to implement large scale multi-photon quantum walks.

In Chapter 7 we used the same beam-displacer network described in Chapter 6 to investigate the topological properties of discrete-time quantum walks. Topological effects have been observed in many physical materials [23, 24] and theoretically predicted to exist in many more systems ranging from condensed matter to high-energy physics [25, 26, 27]. The universality of topological behaviour make it interesting to study from a fundamental physics perspective as well as for technological applications in the development of exotic states of matter [28]. However, the topological properties of real materials are difficult to manipulate and directly observing topologically protected bound-states is technically challenging. In our work we demonstrate an unprecedented control over the topological properties of a quantum system. We are able to both manipulate topological parameters, or invariants, of quantum walks at will, and directly image the wave function of bound states between topologically distinct regions. In doing so, we conclusively demonstrate the topological protection of bound-states identical to those in the long predicted but never observed, Su-Schrieffer-Heeger model of polyacetylene [29], as well as discovering an entirely new topological phenomenon: a pair of topologically protected bound states unique to periodically driven systems. Our work adds to the growing number of quantum walk experiments falling under ‘quantum simulation or emulation’ [30, 22], and highlights the versatility of these systems as quantum simulators.

In Chapter 8 we presented our demonstration of a two-photon quantum walk on an eliptical graph. This work is the first quantum walk in a three-dimensional waveguide structure with genuine non-classical photonic inputs. Studying quantum walks in two or more dimensions allows the exploration of interesting graphs [31] that are not possible in the one-dimensional case without the addition of multiple-walkers [14]. In particular, quantum walks on two-dimensional graphs are a powerful tool in searching for marked nodes, giving information not only of their position, but also of the local structure [12]. Furthermore, our work presents the first multi-walker quantum walk with periodic boundary conditions, a system that has been theoretically predicted to exhibit non-trivial time-dependent entanglement dynamics for a low number of walk lattice positions [32].

Our work complements other multi-photon continuous-time quantum walks in waveguide structures [33], but more importantly it contributes a significant step towards realising complex Hamiltonians using evanescently coupled waveguides for use in quantum emulation. With laser-written waveguide technology achieving a varied waveguide coupling is a matter of altering refractive index profiles of individual waveguides as well as their relative positions to one another [34]. By this method (see Section 5.3) others have simulated a variety of interesting physical phenomenon that are otherwise difficult to observe including Zitterberwegung (trembling motion) [35], Klein tunnelling [36] and Anderson localisation [37].

A particularly exciting prospect for the future is the simulation of coherent biological effects using the quantum walk formalism, which has been studied extensively by Mohseni *et al.* [38]. As their study suggests, an emulation of coherent quantum effects in the Fenna-Matthews-Olson

(FMO) protein complex could be achieved by a judicious choice of coupling parameters between lattice positions in a continuous-time quantum walk. It is likely that such an experiment is within reach of current laser-written waveguide capabilities. Most interestingly, they discover that energy transport around the FMO protein is enhanced by decoherence, in a process known as environmentally-assisted quantum transport [39]. However, central to such an investigation is the ability to experimentally tune the amount of decoherence for a continuous-time quantum walk, which is currently an open problem in experiments with laser-written waveguides.

In conclusion, this thesis contributes a significant development to the progression of photonic quantum information and simulation science. As well as improving upon existing quantum optics techniques, it expands the physical toolbox used for coherent control of photonic quantum states. In doing so, this work moves photonics closer to realising useful applications in engineered quantum systems.

References

[1] Yao, X.-C. *et al.* Observation of eight-photon entanglement. *Nature Photonics* **6**, 225–228 (2012).

[2] Lita, A. E., Miller, A. J. & Nam, S. W. Counting near-infrared single-photons with 95% efficiency. *Opt. Express* **16**, 3032–3040 (2008).

[3] Christ, A. & Silberhorn, C. Limits on the deterministic creation of pure single-photon states using parametric down-conversion. *Phys. Rev. A* **85**, 023829 (2012).

[4] Ma, X.-s., Zotter, S., Kofler, J., Jennewein, T. & Zeilinger, A. Experimental generation of single photons via active multiplexing. *Phys. Rev. A* **83**, 043814 (2011).

[5] Migdall, A. L., Branning, D. & Castelletto, S. Tailoring single-photon and multiphoton probabilities of a single-photon on-demand source. *Phys. Rev. A* **66**, 053805 (2002).

[6] Brukner, C., Taylor, S., Cheung, S. & Vedral, V. Quantum entanglement in time. *arXiv:quant-ph/0402127v1* (2004).

[7] Leggett, A. J. & Garg, A. Quantum mechanics versus macroscopic realism: Is the flux there when nobody looks? *Phys. Rev. Lett.* **54**, 857–860 (1985).

[8] Goggin, M. E. *et al.* Violation of the Leggett–Garg inequality with weak measurements of photons. *Proceedings of the National Academy of Sciences* **108**, 1256–1261 (2011).

[9] Xu, J.-S., Li, C.-F., Zou, X.-B. & Guo, G.-C. Experimental violation of the leggett-garg inequality under decoherence. *Scientific Reports* **1** (2011).

[10] Palacios-Laloy, A. *et al.* Experimental violation of a Bell's inequality in time with weak measurement. *Nature Physics* **6**, 442–447 (2010).

[11] Kendon, V. & Tregenna, B. Decoherence can be useful in quantum walks. *Phys. Rev. A* **67**, 042315 (2003).

[12] Berry, S. D. & Wang, J. B. Quantum-walk-based search and centrality. *Phys. Rev. A* **82**, 042333 (2010).

[13] Rohde, P. P., Fedrizzi, A. & Ralph, T. C. Entanglement dynamics and quasi-periodicity in discrete quantum walks. *Journal of Modern Optics* **59**, 710–720 (2012).

[14] Rohde, P. P. *et al.* Increasing the dimensionality of quantum walks using multiple walkers. *arXiv:1205.1850v1* (2012).

[15] Shenvi, N., Kempe, J. & Whaley, K. B. Quantum random-walk search algorithm. *Phys. Rev. A* **67**, 052307 (2003).

[16] Potoček, V., Gábris, A., Kiss, T. & Jex, I. Optimized quantum random-walk search algorithms on the hypercube. *Phys. Rev. A* **79**, 012325 (2009).

[17] Knill, E., Laflamme, R. & Milburn, G. J. A scheme for efficient quantum computation with linear optics. *Nature* **409**, 46–52 (2001).

[18] Aaronson, S. & Arkhipov, A. The computational complexity of linear optics. *Proceedings of the 43rd annual ACM symposium on Theory of computing. ACM* (2011).

[19] Kitagawa, T. *et al.* Observation of topologically protected bound states in photonic quantum walks. *Nature Communications* **3** (2012).

[20] Schreiber, A. *et al.* Decoherence and disorder in quantum walks: From ballistic spread to localization. *Phys. Rev. Lett.* **106**, 180403 (2011).

[21] Schreiber, A. *et al.* A 2D quantum walk simulation of two-particle dynamics. *Science* **336**, 55–58 (2012).

[22] Sansoni, L. *et al.* Two-particle bosonic-fermionic quantum walk via integrated photonics. *Phys. Rev. Lett.* **108**, 010502 (2012).

[23] Chen, Y. L. *et al.* Experimental realization of a three-dimensional topological insulator, Bi2Te3. *Science* **325**, 178–81 (2009).

[24] Xia, Y. *et al.* Observation of a large-gap topological-insulator class with a single Dirac cone on the surface. *Nature Physics* **5**, 398–402 (2009).

[25] Nayak, C., Simon, S. H., Stern, A., Freedman, M. & Das Sarma, S. Non-Abelian anyons and topological quantum computation. *Rev. Mod. Phys.* **80**, 1083–1159 (2008).

[26] Fu, L. & Kane, C. L. Superconducting proximity effect and Majorana fermions at the surface of a topological insulator. *Phys. Rev. Lett.* **100**, 096407 (2008).

[27] Jackiw, R. & Rebbi, C. Solitons with fermion number $\frac{1}{2}$. *Phys. Rev. D* **13**, 3398–3409 (1976).

[28] Zhang, S. Topological states of quantum matter. *Physics* **1**, 6 (2008).

[29] Su, W. P., Schrieffer, J. R. & Heeger, A. J. Solitons in polyacetylene. *Phys. Rev. Lett.* **42**, 1698–1701 (1979).

[30] Regensburger, A. *et al.* Zitterbewegung, Bloch oscillations and Landau-Zener tunneling in a quantum walk. *arXiv:1104.0105v1* (2011).

[31] Aharonov, D., Ambainis, A., Kempe, J. & Vazirani, U. Quantum walks on graphs. In *Proceedings of the thirty-third annual ACM symposium on Theory of computing*, STOC '01, 50–59 (ACM, New York, NY, USA, 2001).

[32] Benedetti, C., Buscemi, F. & Bordone, P. Quantum correlations in continuous-time quantum walks of two indistinguishable particles. *Phys. Rev. A* **85**, 042314 (2012).

[33] Peruzzo, A. *et al.* Quantum walks of correlated photons. *Science* **329**, 1500 (2010).

[34] Nolte, S., Will, M., Burghoff, J. & a. Tuennermann. Femtosecond waveguide writing: a new avenue to three-dimensional integrated optics. *Applied Physics A* **77**, 109–111 (2003).

[35] Dreisow, F. *et al.* Classical simulation of relativistic Zitterbewegung in photonic lattices. *Phys. Rev. Lett.* **105**, 143902 (2010).

[36] Dreisow, F. *et al.* Klein tunneling of light in waveguide superlattices. *Europhysics Letters* **97**, 10008 (2012).

[37] Naether, U. *et al.* Anderson localization in a periodic photonic lattice with a disordered boundary. *Opt. Lett.* **37**, 485–487 (2012).

[38] Mohseni, M., Rebentrost, P., Lloyd, S. & Aspuru-Guzik, A. Environment-assisted quantum walks in photosynthetic energy transfer. *J. Chem. Phys.* **129**, 174106 (2008).

[39] Rebentrost, P., Mohseni, M., Kassal, I., Lloyd, S. & Aspuru-Guzik, A. Environment-assisted quantum transport. *New Journal of Physics* **11**, 033003 (2009).